Interfacial Transport Processes Involved in the Surfactant Facilitated Wetting of Liquids on Solid Surfaces and Non-wetting on Superhydrophobic Surfaces.

by,

Nikhil S Bhole

A Dissertation submitted to the Graduate Faculty in Engineering in
Partial Fulfillment of the Requirements for the Degree of
Doctor of Philosophy,
The City University of New York

2011

This manuscript has been read and accepted for the Graduate Faculty in Engineering in satisfaction of the dissertation requirement for the degree of Doctor of Philosophy.

Date	Prof. Charles Maldarelli (Mentor) Chair of Examining Committee
Date	Prof. Mumtaz K. Kassir Executive Officer
	Prof. Alexander Couzis
	Prof. Morton Denn
	Prof. Jeffrey Morris
	Prof. Taehun Lee
	Dr. Mohsen Yeganeh

Supervisory Committee

THE CITY UNIVERSITY OF NEW YORK

ABSTRACT

Interfacial Transport Processes Involved in the Surfactant Facilitated Wetting of Liquids on Solid Surfaces and Non-wetting on Superhydrophobic Surfaces.

by Nikhil Bhole

Under the supervision of Professor Charles Maldarelli at Levich Institute and Chemical Engineering Department at the City College of New York of Graduate Center CUNY.

The control of the wetting properties of aqueous solutions on surfaces is critical to the implementation of many industrial technologies. Aqueous solutions are often required to rapidly wet hydrophobic solid and liquid (oil) surfaces. Surfactants, dissolved above the critical micelle concentration, are useful in quickly reducing aqueous/solid and aqueous/oil tensions to facilitate spreading. In other applications, aqueous droplets are required to roll over surfaces, and surfaces engineered with textures which trap air between grooves as the drop moves over the surface retain large droplet contact angles and reduced friction, which causes rolling.

The first part of this dissertation studies the transport of surfactant from an aqueous micellar solution to an oil phase, initially without surfactant, which is placed in contact with the water. Surfactant monomer diffuses and adsorbs from the aqueous phase onto the interface, and subsequently desorbs into the oil. The decrease in the surfactant monomer concentration in the vicinity of the surface disturbs the monomer-micelle equilibrium causing the micelles to break down to replenish the sublayer with monomer. The increase results in a more rapid reduction in interfacial tension. However, when the micellar concentration is too low, the micelle diffusion flux required to replenish the monomer underneath the surface cannot be achieved, and a zone is formed (just underneath the oil-water interface) from which micelles

completely disappear. This micelle-free zone, which retreats from the surface, represents a barrier to the enhanced surfactant flux to the surface. A fluorescing dye is trapped in the micelles to provide a fluorescence contrast so that the micelle-free zone can be located. A Confocal Laser Scanning Microscope is used to spatially resolve the micelle-free zone, and measure the movement of the zone from the interface. A diffusion limited transport model is also developed which predicts the location of the micelle-free zone as a function of time, and compares well with the experiments.

Part two of the dissertation focuses on studying the (superhydrophobic) non-wetting behavior demonstrated by aqueous droplets on surfaces consisting of a periodic array of micron-sized posts. Boundary integral hydrodynamic solutions for the two dimensional, inertialess, gravity-driven movement of a droplet over this micro-texture are obtained to understand the flow on the length scale of the topography. Two regimes are identified: In one, the advancing line spreads relatively easily over the top of a post, sticks to the back of the post, develops increasing curvature and finally jumps to the next post. This cycle repeats until the drop becomes tethered to the back of a post and achieves equilibrium. In the second, the advancing line again cycles between wetting, sticking and jumping, but penetrates the grove between the posts before jumping. This behavior, which precedes the full wetting regime, occurs when the contact angle of the post material is reduced or, the pitch between posts becomes large.

Acknowledgements

I owe my deepest gratitude to my mentor, Prof. Charles Maldarelli, for his endless support and guidance throughout my graduate studies. His expertise in the field of interfacial science and chemical engineering has helped me a lot in my research. He has been an excellent mentor. He provided me complete independence to work on the research projects, which encouraged me to take initiatives and develop creative thinking. I learnt from him how to visualize a scientific problem from different perspective, identify key issues and come up with a most optimal solution.

Further, I would like to thank my thesis examining committee members Prof. Alexander Couzis, Prof. Morton Denn, Prof. Jeffrey Morris, Prof. Taehun Lee and Dr. Mohsen Yeganeh for providing constructive comments on this thesis. I appreciate the generous guidance provided by Prof. Alexander Couzis at every stage in my PhD. I would like to thank Prof. Kretzschmar for the Scanning Electron Microscope and Dr. Song, Dr. Pawar and Dr. Niitsoo for their help with the SEM. I also would like to thank Prof. Morris for the fast video camera. Many thanks to Dr. Shojaei-Zadeh for helping me with the micro-fabrication techniques.

I am grateful to all former and current members of the Surface Science Group at the City College of New York: Nikhil K, Makonnen, Jonathan, Shyam, Fenfen, Spyros, Gerson, Shahab, Isabel, Olivia, Thomas, Xiaoxiao, Nima, Ankur and Vilobh – for their guidance and inputs they provided in my research, without which I could not have mastered the required analytical skills and also for maintaining friendly atmosphere in the lab. Special thanks to all my graduate colleagues, who helped in many ways during my graduate studies and made my stay at the City College a wonderful experience.

During my stay in New York, I got an opportunity to make many friends. Without them life as a graduate student would not have been the same. A big thanks to all of

you guys: Nilesh, Ankur, Vilobh, Swapnil, Shripad, Prasad K/Y, Jas, Vikas, Sandeep, Amar, Pandurang, Shyam, Rohit, Nikhil K, John, Rajesh, Chi, Jayant, Abhinav, DJ, Amit, Kunal, Sharli and many more, for making my stay at the CCNY a cheerful and memorable experience.

I dedicate this thesis to my parents, Mr. Suresh Bhole and Mrs. Shobha Bhole. It is the result of their enduring efforts, love, and support that I have been able to undertake this task and do justice to it. They always encouraged me to achieve higher and higher goals. Also I would like to thank my brother Ashish and sister-in-law Swati for being there always in every stage in my life. Finally, special thanks to a very special person in my life, Pranali, for her love, affection and caring support during the lows and highs of my graduate studies.

Contents

List of Tables

List of Figures

Chapter 1

Introduction

The control of the wetting properties of aqueous solutions on surfaces is critical to the implementation of many industrial interfacial technologies. In many applications, aqueous solutions are often required to rapidly *wet* hydrophobic solid surfaces as, for example, in agricultural or textile industries as well as in ink-jet printing. Because of the difference in polarity, aqueous solutions do not usually readily wet hydrophobic surfaces. To facilitate the wetting of the hydrophobic solid surface by an aqueous solution, surfactants are dissolved in the aqueous phase. At the spreading periphery of the aqueous phase (the advancing contact line), surfactants in solution adsorb at the air/liquid and solid liquid interfaces, reducing the air/water and solid/water tensions. This lowers the contact angle of the aqueous phase at the advancing contact line to promote spreading. To achieve rapid spreading, the surfactant must be delivered rapidly to the advancing interface, and this is achieved by dissolving the surfactant at high enough concentrations where aggregates (micelles) form in the bulk solution. The micelles act as reservoirs of surfactant for delivery to the surface. In other industrial contexts, air/water and oil/water tensions are required to be reduced rapidly as in the formation of fine emulsions and highly textured foams. Concentrated micellar surfactant solutions are again useful for quickly reducing the tensions of these

interfaces. In contrast to these applications, the design of solid surfaces which are very water *repellant* - or equivalently are completely dewet by an aqueous phase - presents a challenge which is not only of broad technological appeal, but which, in its study, raises important issues in the understanding of the science of wetting[3]. In many applications, it is required to prevent wetting of solids by aqueous droplets, and aqueous droplets are required to roll over surfaces. Such an extreme water repellency is achieved by engineering surfaces with textures which trap air between grooves as the drop moves over the surface. At the spreading periphery of droplets placed on these surfaces, the droplet retains large contact angles (suprehydrophobicity) and reduced friction, which causes rolling.

In this work we are investigating both of these extreme requirements in wetting. Part One of this report focuses on studying transport of surfactant from aqueous micellar solutions to an interface, with an aim towards understanding how the reservoirs of surfactant present in the aggregates accelerates the adsorption rate on to the surface. Part Two studies the extreme non-wetting, super-water-repellent behavior illustrated by textured surfaces. Our aim in this part is to provide a picture of the microhydrodynamics of the spreading to develop an understanding of how the textures control the superhydrophobicity. In this Introduction, we provide a description of tthe scope of research for each of these parts.

1.1 Surfactant Transport from a Bulk Aqueous Phase to an Oil-Water Interface

Surfactant molecules dissolved in an aqueous phase can cluster into aggregates (micelles) in solution [4, 5, 6]. This assembly is driven by the hydrophobic effect, as the aggregates remove the hydrophobic groups of the surfactant from contact with water while maintaining the contact of the polar groups with water. The equilibrium

aggregate phase behavior of surfactants in solution has been extensively studied, and phase diagrams map the different aggregate shapes which can form (spherical and cylindrical aggegates, hexagonal and bicontinuous phases). In this study, we focus on the simplest structure which forms at low concentrations, the globular micelle (Fig. 2.3(a)) in which, in bulk aqueous solution, the chains cohere into a central core surrounded by the polar groups. The self assembly of aggregates from isolated monomeric surfactant molecules in aqueous solution occurs principally at a critical bulk concentration of surfactant (the critical micelle or aggregate concentration, CMC or C_{CMC}) at which the chemical potential of the surfactant in the aggregate becomes equal to the potential of the molecule in solution. As the bulk concentration of surfactant, C_b, increases above the C_{CMC}, the aggregate concentration increases. At equilibrium, for $C_b > C_{\mathrm{CMC}}$, the monomer concentration in equilibrium with the micelles is approximately constant (and equal to the C_{CMC}), and added surfactant above the C_{CMC} is mostly incorporated into micelles [7]. The equilibrium is a dynamic one, with aggregated surfactant exchanging with singly dispersed monomer. When this equilibrium is perturbed, aggregates either break down or re-assemble in order to return the monomer concentration to the C_{CMC}.

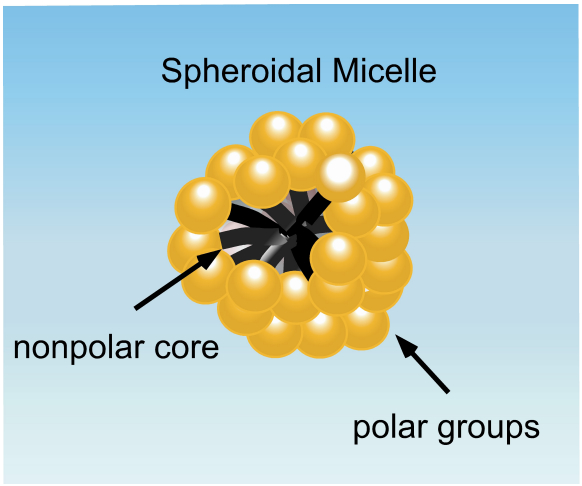

Figure 1.1: The micellization of surfactant in the bulk aqueous media into spheroidal aggregates with the nonpolar chains of the surfactant coheing into a hydrophobic, liquid-like core and the polar groups surrounding the core in contact with water.

As a model to study the adsorption processes which occur in a micellar surfactant solution as surfactant adsorbs from solution onto a hydrophobic solid surface, we examine first the simpler case of the transport processes which occur when a clean (i.e. surfactant-free) hydrophobic oil phase contacts the aqueous solution. Generally, in this case, surfactant monomer adsorbs onto the interface between the oil (or hydrophobic solid) and water, driven by the same hydrophobic effect which underlies the aggregate assembly in the bulk aqueous phase. A monolayer forms, with the tail groups extending into the oil. If soluble in the oil, surfactant can desorb off of the surface and diffuse into the oil phase (see for example [8, 9, 10]). At the interface, the adsorption process proceeds by the kinetic adsorption of surfactant monomer (and possibly aggregates, see for example Bain et al. [11]) onto the interface from the sublayer of the aqueous phase adjoining the interface, followed by diffusion of monomer (and aggregates) to the sublayer to replenish adsorbed species. The diffusion sustains the adsorption until equilibrium is achieved. The bulk depletion of the surfactant monomer disturbs the monomer-aggregate equilibrium, and the aggregates disassemble to restore the monomer concentration. This disassembly accelerates the time scale for the diffusion process and, along with the possible direct adsorption of micelles, shortens the equilibration time.

In this study, we focus on the case in which the diffusion processes in the aqueous phase are slow relative to the kinetic disassembly of the micelles. In the limit of rapid disassembly, micelles act to maintain the monomer concentration at the critical micelle concentration. When the concentration of surfactant is not much larger than the CMC for the case of fast kinetics, a transport regime arises in which a "micelle-free zone" develops underneath the oil-water interface as diffusion of micelles cannot keep up with adsorption of monomer onto the interface. This zone extends from the interface into the aqueous phase up to a boundary which separates the micelle-free region from a zone, containing micelles, which extends further into the aqueous

phase. Micelles diffuse from the micelle zone to the boundary, where they break down causing the the boundary to retreat. At higher bulk micellar concentrations, the micelle-free zone does not develop. This model was first developed (Song et al. [12]) to model the transport of a polyethoxylated surfactant with a low CMC from micellar solutions just above the CMC to a clean air/water interface. Numerical simulations of the dynamic tension reduction using the model were compared with measurements obtained from the pendant bubble apparatus with excellent agreement without adjustable constants. (The required monomer transport parameters for the model (diffusion coefficient, and adsorption and desorption kinetic rate constants for monomer exchange onto the interface) were obtained from submicellar dynamic tension measurements, and the diffusion coefficient of the micelles was obtained from light scattering).

The earlier study of Song et al. [12] did not provide direct evidence of the micelle free-zone, and our aim here is to provide visual evidence of the zone by fluorescently demarcating the region retaining micelles. This is undertaken by dissolving a small hydrophobic dye molecule (Nile Red) in the micellar solution of a nonionic polyethoxylated surfactant $C_{14}E_6$ ($CH_3(CH_2)_{13}(OCH_2CH_2)_6OH$). The dye partitions strongly into the micelle interior, and, upon excitation, only fluoresces when in the hydrophobic environment of the micelle. The fluorescence is quenched when the dye is in water. This provides the fluorescent contrast between the zones, and we use confocal microscopy, imaging at different depths underneath the interface, to quantitatively measure the depth of the micelle-free zone underneath the oil/water interface as surfactant transports to the oil and the micelle-free zone moves away from the interface. The model, and its extension to transport through the oil/water interface, is detailed in the Chapter 2 along with numerical results obtained from solving the transport equations. The fluorescence experiments are described in the Chapter 3, and these experiments are then compared favorably to the numerical simulations,

providing further support for the model.

1.2 Non-wetting Over Superhydrophobic Surfaces

Water repellancy is a subject which has been researched at length for several decades. However, most of this research has focused on the *chemical* modification of the surface to make the surface water repellant. In these studies, molecules or polymers displaying nonpolar (hydrophobic) chemical groups are either phys-adsorbed or covalently grafted to the surface in such a way that the the hydrophobic groups dangle from the air/solid interface. Since the hydrophobic moities are nonpolar, the interaction of water molecules with these groups is not as strong as the dipolar interaction of water to itself, and consequently the water molecules do not spread over the modified surface. Self assembling monolayers (SAMs) of amphiphiles, terminated by hydrophobic functional group, are one of the more important examples of this approach of controlling the surface chemistry to achieve water repellancy. The two SAM systems which have been extensively studied are alkylthiols (X-$(CH_2)_n$SH; X is the terminal functional group) on the gold surface[13] and alkyltrifunctionalsilanes (X-$(CH_2)_n$$SiY_3$, Y = -Cl or -OMe or -OEt) onto hydroxylated surfaces such as glass or the native oxide surface of silicon or glass[14]. For water repellancy applications, to make the surface hydrophobic, the terminal group X is usually a methyl or fluorinated group, e.g. $(CF_3(CF_2)_i-)$.

While an effective approach with a history of success, it has long been recognized that complete dewetting cannot be achieved by changing the surface chemistry alone. A common measure of repellancy is the equilibrium contact angle θ_e subtended by millimeter-sized water droplets placed on the surface; the contact angle is defined as the angle, as measured through the liquid phase, between the substrate and the air/aqueous interface at the three phase (liquid/solid/air) contact line. Complete

wetting corresponds to angles approaching zero, and complete dewetting corresponds to angles approaching 180°. Intermediate angles describe partial wetting conditions, Droplets of water, placed on surfaces chemically modified with silanes terminated in a methyl group, retain contact angles which are large but with an upper limit of no larger than approximately 110°-120°, [15] but complete dewetting, cannot be achieved.

A second issue in the context of chemical modification to achieve complete dewetting is the presence of contact angle hysteresis. A common observation is that droplets placed on a surface move only when the advancing angle at the incipient moving front of the drop exceeds a critical value ($\theta_a > \theta_e$), and the receding angle at the back of the drop becomes less than a critical value ($\theta_r < \theta_e$). The difference ($\Delta\theta = \theta_a - \theta_r$) is the contact angle hysteresis and this limits the mobility of drops placed on the surface since enough stress has to be placed on the drop to exceed the threshold ($\Delta\theta$) before it can move. So even in the presence of large equilibrium angles, drops can be retained by the hysteresis. The origin of hysteresis lies in chemical or topological heterogeneities. Heterogeneities of the scale of microns or larger provide contact angle hysteretic effects on millimeter-sized droplets. When surfaces are chemically treated to be hydrophobic for water repellancy, attention must also be focused on the fact that the resulting treated surface must be chemically homogeneous and topologically smooth so as not to develop a large contact angle hystereis. This can prove to be very challenging since surfaces before treatment do not display such homogeneity.

A breakthrough in the understanding of how to design very water repellant surfaces has come over the past decade with the recognition that surfaces with a microstructured topology consisting of a pattern of elevations and troughs can give rise to very large contact angles ($130^0 - 180^0$). The scale of the features is usually of the order of $10 - 100\mu$m. This important observation was first made through the study of water repellancy in biology [16], where naturally microtextured hydrophobic surfaces

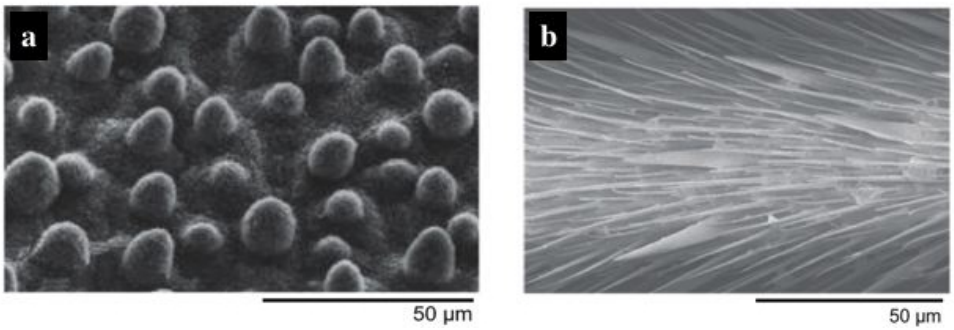

Figure 1.2: SEM images of naturally occuring superhydrophobic surfaces, showing surface roughness on (a) lotus leaf and (b) leg of a water strider. On the leaves of the lotus plant water contact angles greater than 160° have been measured. [1]

were observed to allow water to dewet, serving a biological function. Fig. 1.2 shows SEM images of two such naturally occurring microtextured surfaces, a lotus leaf and the leg of a water strider. In the synthetic, chemical modification approach, the repellency is primarily a consequence of the interactions between the water molecules and the surface grafted groups. In the case of a microtextured surface, the aqueous phase moves over the elevations, riding between the elevations (i.e. over the troughs) on a cushion of air. The surfaces themselves are required to be hydrophobic enough in order that the water does not penetrate into the troughs. The configuration in which water does not penetrate the depressions is termed a "Fakir" arrangement and the surfaces as "superhydrophobic" or "super water repellant". To prevent spreading into the depressions, the contact angles of these surfaces – formed as planar substrates – is required to be of the order of 90° - 100°. These superhydrophobic surfaces also have the added advantage that they exhibit marginal contact angle hysteresis because of the reduced friction of the air/water interface, which allows drops, when placed on these surfaces, to readily roll off. An alternate regime in which the spreading liquid penetrates the troughs of the microstructure (complete wetting) exhibits much lower contact angles, and a roughness induces hysteresis which limits the mobility of droplets placed on these surfaces.

The numerous technological applications envisioned for superhydrophopic surfaces because of their super water repellency have provided the impetus for a number of research investigations. Because of the reduced contact area and minimum contact angle hysteresis, water droplets placed on these surfaces are very mobile and can readily roll onto and off of the surfaces. This property of superhydrophobic surfaces can be taken advantage of in manufacturing waterproof and self-cleaning coatings for satellite dishes, solar energy panels, photovoltaics and textiles [17]. Also several studies have demonstrated that liquids moving over microstructured surfaces in which air remains trapped in the cavities (the Fakir configuration) reduces the drag exerted by the liquid on the surface due to the fact that part of the interface is an air/liquid surface of low friction [18, 19, 20, 21]. This can have potential application in developing coatings for submarines as well as in microfluidic devices. These coating have also proved to be effective at anti-biofouling on the hulls of ships, preventing adherence of unwanted microorganisms such as algae [22].

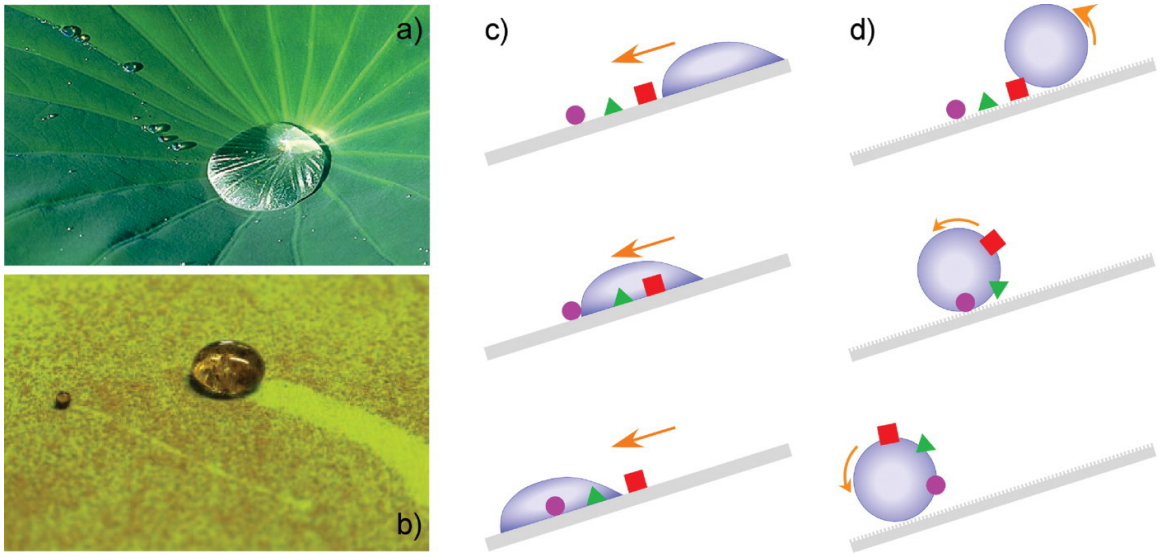

Figure 1.3: (a) Lotus leaf, (b) Self-cleaning ability shown by the textured surface, (c) Particulates on the flat surface are redistributed by the sliding drop, while (d) on a textured surface droplet rolls as opposed to slide and collects the particulates on its way [2].

Most of the research on the subject of superhydrophobic surfaces can be divided into efforts focusing on either the experimental fabrication of the surfaces, or the theoretical understanding of the circumstances at equilibrium under which liquids either sit over the depressions of a textured surface (the Fakir configuration), or penetrate the depressions, wetting completely the substrate. Most of the theoretical efforts in this field are based on thermodynamic grounds, where final configuration of a droplet is predicted from free-energy minimization to achieve a global minimum at equilibrium. However, wetting is a dynamic phenomena, and the aim of this study is to examine how fluid movement, and the associated hydrodynamic stresses, affects the interfacial configuration as drops ride over the microtextured surface. The study is both experimental and theoretical. Theoretically, hydrodynamic equations are solved numerically for a droplet spreading over a topography using a Boundary Integral Method to understand the interaction of the surface microstructures with the droplet. From these simulations we find that during the spreading process, the droplet experiences many local minima and its motion is arrested before the global minimum is achieved. This arrest of the droplet motion cannot be predicted by energy minimization approaches we find in the literature. Numerical formulations of the hydrodynamic model and results are presented in Chapter 4. Experimentally, micro-textured surfaces are fabricated by using soft-lithography technique and droplet fluid motion in the vicinity of the contact line is captured by video microscopy set up, as described in Chapter 5. This contact line motion is then qualitatively compared with the numerical results.

Chapter 2

Theoretical Studies of Surfactant Transport

When aqueous solution of non-ionic surfactants of above CMC concentration is contacted with initially clean oil phase, surfactant monomers partition themselves into the oil phase causing depletion of monomer concentration near the oil/water interface. This in turn causes micelles to break up and drives diffusion of monomers and micelles towards the interface. In this study, we focus on the case in which the diffusion processes in the aqueous phase are slow relative to the kinetic disassembly of the micelles. In this limit of rapid-disassembly of micelles under appropriate conditions two-zones are formed, one containing micelles (away from the oil/water interface) and one completely depleted of micelles (just underneath the oil/water interface). A two-zone micelle transport model is described in Section 2.1, transport equations for solving the model are detailed in Section 2.2, and simulation results are presented in the following Section 2.3.

2.1 Description of the Two-Zone Micelle Transport Model

The general mechanism for the transport of surfactant from an aqueous micellar solution to an initially clean oil/water interface (or any adsorbing surface for that matter) involves, in the aqueous phase, the diffusion of monomer and micelle to the surface, and the kinetic disassembly of the aggregates. The model we develop is based on a separation of time scales for which kinetic disassembly is faster than diffusion, and we first write expressions for these time scales in order to formulate the model and develop criteria for its range of validity. We will develop the model in the context of relatively small aggregates of a few hundred or less monomers - spheres, globules or short rods - which characterize aggregates at concentrations just above the CMC, as these are the conditions of the experiment. Time scales for diffusion of monomer (τ_D^m) and micelles (τ_D^{mic}) in the aqueous phase to the surface are given by ℓ^2/D_w^m and ℓ^2/D_w^{mic}, respectively, where D_w^m and D_w^{mic} are the diffusion coefficients of monomer and micelle in the water, respectively, and ℓ is the length scale over which diffusion is occurring. This length scale corresponds to either the depth of the aqueous phase underneath the surface, or, if this is very large, the adsorption depths h of the monomer and micelle. The adsorption depth is the distance underneath the surface which contains, per unit area, the same amount of surfactant required (in monomer or micelle form) to saturate the surface and, for an oil/water interface the oil phase. For an air/water interface with a maximum packing concentration of Γ_∞, the adsorption depths of the monomers and micelles are respectively, $\Gamma_\infty/C_{\mathrm{CMC}}$ and $\Gamma_\infty/(C_b - C_{\mathrm{CMC}})$ and can be much less than the depth of the aqueous phase. However, for transport into an initially clean oil phase, when the volume of oil is large enough, and the CMC and the bulk concentration of micelles are small enough (as will be the cases in the experiments undertaken here), the adsorption depth is much larger than

the depth of the aqueous phase, and hence the depth of the aqueous phase becomes the determining factor in the diffusion time scale. In formulating these scales, it should be noted that it has been assumed that the length scale of the oil normal to the surface is much smaller than that of the aqueous phase, so that the aqueous phase transport is limiting. This is certainly true in the experiments described here; if larger volumes of oil are used then the diffusion in the oil could become rate limiting and would set the diffusion time scale.

To formulate an expression for the time scale for micelle breakdown, we note that the micellization kinetics is complicated by the fact that experimentally it is known that the aggregates exist as a polydisperse distribution of micelles of different sizes (different numbers of monomers per aggregate), rather than as a single monodisperse species. This polydispersity can be understood in terms of the simplified stepwise model which has been used to describe the kinetics of micellization (for reviews see [23, 24, 25]). In this model, an aggregate population is built up by individual steps of the addition and subtraction of a single monomer to an aggregate. Thus aggregate species S_i containing i monomers per aggregate either adds a monomer to form S_{i+1} or S_{i+1} releases a monomer to form S_i, $S_i + S \underset{k_{-i}}{\overset{k_i}{\rightleftharpoons}} S_{i+1}$, where k_i and k_{-i} are the rate constants for the forward and backward reaction step respectively and are dependent upon i. In micelle assembly the process is cooperative in the sense that k_{-i} decreases with i due to the hydrophobic effect, and anti-cooperative for large enough i due to the repulsion in the headgroups. This competition gives rise to a characteristic distribution of the population as a function of i consisting of large numbers of monomers and oligomers, a region abundant in micelles with a distribution (approximated as Gaussian) centered on a single value σ (usually approximately several tens to a few hundred monomers per aggregate), and a region in between in which the concentration of aggregates is small. Experimental techniques to measure the micelle kinetics disturb equilibrium population distributions by subjecting the solution to either a temperature or pressure

jump or an ultrasonic disturbance, or by dilution by mixing with a solution below the CMC (stopped-flow experiment) [26]. The re-equilibration of aggregate and monomer concentrations is followed by conductivity measurements (for ionic surfactants) or by fluorescence or extinction coefficient measurements of dye molecules partitioning between the micelle and solution phases. The slow time scale τ_{SL} for the micelle disassembly kinetics, which is related to the slow re-equilibration as rare aggregates break-up to reform monomers and bring the monomer concentration back to the CMC and the center of the abundant micelle distribution back to σ [27, 28, 29, 30], is in the range of $10^{-3} - 10$ sec. For the time scale for diffusion to be slower than the time scale for kinetic disassembly, we require the slow kinetic step to be faster than the bulk diffusion time scales or

$$\tau_{SL} << \ell^2/D_w^m \tag{2.1}$$

where ℓ is the extent of the aqueous phase normal to the surface. If the above inequality holds, then micelles also diffuse slower than aggregates disassemble since $D_w^{mic} < D_w^m$ micelle diffusion time scale is even slower since the micelle diffusion coefficient is smaller than that of the monomer. In our study we arrange conditions such that diffusive rates of transport are slower than the rate of micelle breakdown. When convective processes are present, these may be faster than the breakdown kinetics and hence a quasi-equilibrium model such as ours would not be valid.

We focus on a case, where convection is absent and above inequality is satisfied. Thus for large departure from equilibrium, diffusion processes take much longer time than micelle break up and in such a quasi-equilibirum (between monomers and micelles) micelles maintain the monomer concentration at the CMC wherever micelles are present. In this limit, the surfactant transport process in the presence of micelles is divided into two regimes which we illustrate for the case of adsorption to a planar oil/water interface with the oil initially clean of surfactant: In the high micelle concentration regime (Fig. 2.1(a)), monomer depletion in the sublayer caused by the

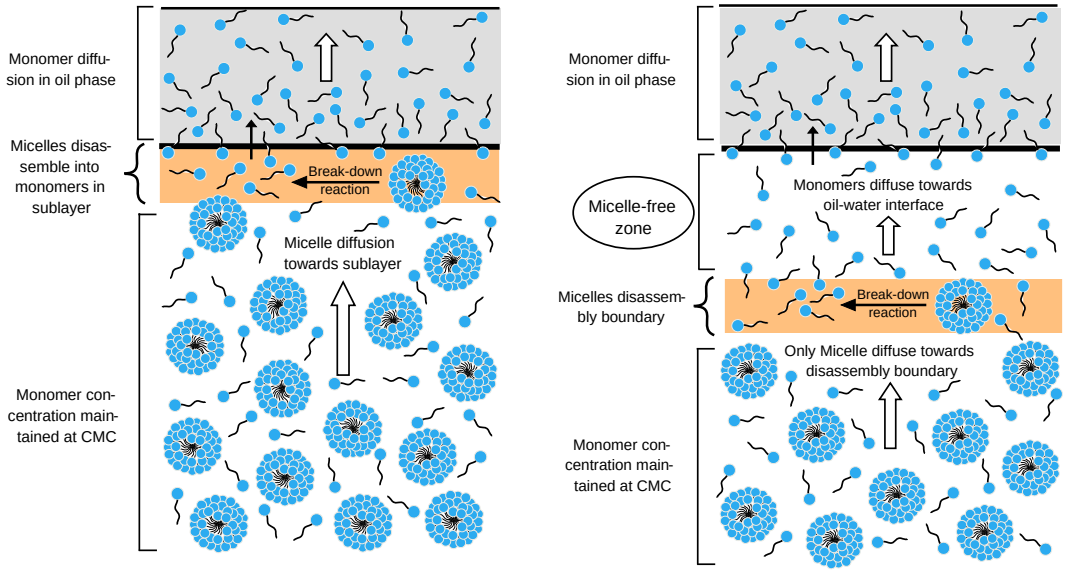

(a) High micelle concentration

(b) Low micelle concentration

Figure 2.1: Pictorial representation of the surfactant transport process from an aqueous micellar solution to an initially clean phase in the quasi-static limit in which micelle disassembly is much faster than diffusion of monomer and micelle.

adsorption at the interface and desorption into the oil is replenished by the micelle break-up in the sublayer as the larger diffusive flux of micelles assures the presence of micelles all the way up to the sublayer. In this regime, only micelles diffuse and the monomer flux is zero, as they are maintained at fixed concentration C_{CMC}. At lower micelle concentrations (Fig. 2.1(b)), the diffusion flux of micelles cannot keep up with the adsorption flux at the interface and micelle break-down takes place away from the interface. This reaction boundary separates two distinct zones, a micelle zone where the monomer concentration is equal to the CMC, and a micelle-free zone where micelles are absent. Thus, in the micelle zone, only micelles diffuse until the micelle disassembly boundary, where the break-down supplies monomers to the micelle-free zone. At the boundary, from the micelle zone side, the micelle concentration is equal to zero, and from the micelle-free zone side the monomer concentration is equal to the C_{CMC}. These monomers, in turn, diffuse to and subsequently adsorb onto the interface. This zone therefore represents a barrier to the surfactant transport process,

preventing micelles from directly reaching the interface. The zone initially forms after an induction time in which the concentration of micelles in the vicinity of the surface decreases due to breakdown (driven by the disequilibrium created by the adsorption of monomer to the surface), and possibly direct micelle adsorption onto the surface. Once the micelle-free zone is formed, it rules out the possibility of direct micelle adsorption as well as solubilization of oil by the micelles as reported by Ariyaprakai et al[31]. As time proceeds, the zone migrates away from the interface, as the adsorption of monomer to the interface continues to deplete the micelle population. With further time, as the interface and oil phase saturate, two kinds of equilibria can be re-established. In one, in which the depth of the aqueous phase extends much further than the micelle adsorption depth, the boundary of the zone can re-approach the fluid interface establishing an equilibrium with a micelle concentration lower than the initial concentration of micelles. Alternatively, if the aqueous phase has been totally depleted of micelles (the micelle adsorption depth larger than the depth of the aqueous phase), an equilibrium is established with the aqueous phase now a submicellar solution. The transition between the two regimes of Fig. 2.1 is demarcated by a critical total bulk concentration of surfactant C_{crit}, for $C_b < C_{crit}$ the second regime follows while for $C_{crit} < C_b$ the first regime obtains. Our focus is on the verification of the two-zone transport picture of Fig. 2.1(b).

2.2 Transport Equations and Numerical Solution

In this section, the two zone transport model, as outlined before, is formulated in one dimension (which will also be the case in the experiments), in which surfactant transports from a micellar solution to an oil phase floating on the top. When the oil layer is first placed on the air/aqueous interface of the micellar solution, the transport begins in one dimension, normal to the oil/water interface. Diffusional transport of

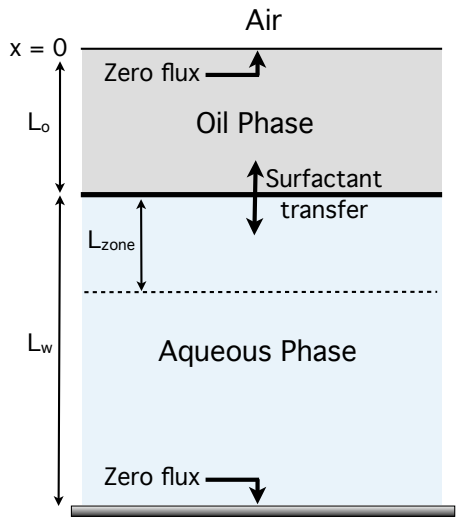

Figure 2.2: Simulation arrangement of oil and water layer for the development of the 1-D transport model.

monomer in the oil and monomer in the micelle-free zone, and micelles in the micelle-zone (Fig. 2.1(b)) are governed by Fick's law

$$\begin{aligned} \frac{\partial C_o}{\partial t} &= D_o \frac{\partial^2 C_o}{\partial x^2} && (0 < x < L_o) \\ \frac{\partial C_w^m}{\partial t} &= \frac{\partial}{\partial x}\left(D_w^m \frac{\partial C_w^m}{\partial x} \right) && (L_o < x < L_o + L_{zone}) \\ \frac{\partial C_w^{mic}}{\partial t} &= \frac{\partial}{\partial x}\left(D_w^{mic} \frac{\partial C_w^{mic}}{\partial x} \right) && (L_o + L_{zone} < x < L_o + L_w) \end{aligned} \tag{2.2}$$

Coordinate x is measured from the oil-air interface into the bulk and L_o, L_{zone} and L_w are the length of the oil phase, the thickness of the micelle-free zone and the thickness of the aqueous phase, respectively (see Fig. 2.2). The parameter t is time, $C_o(x,t)$ and $C_w^m(x,t)$ are the bulk surfactant concentrations of monomer in the oil and the aqueous phase of the micelle-free zone, respectively and D_o and D_w^m are the bulk diffusivity of monomer in the oil and aqueous phases, respectively. Recall that the concentration of monomer in the micelle zone is uniform and equal to the CMC, so a monomer concentration field does not have to be solved for in this region. In the micelle zone, the aggregate population is assumed to be monodisperse, characterized by a single

species (with concentration C_w^{mic} corresponding to the peak in the distribution of concentrations of the abundant micelle aggregate population). This aggregate has diffusion coefficient D_w^{mic} and σ aggregates per micelle.

At the air/oil interface and the aqueous/solid surface, zero flux boundary conditions are imposed,

$$\left[\frac{\partial C_o}{\partial x}\right]_{x=0} = 0 \tag{2.3}$$

$$\left[\frac{\partial C_w^{mic}}{\partial x}\right]_{x=L_o+L_w} = 0 \tag{2.4}$$

$$\left[\frac{\partial C_w^{m}}{\partial x}\right]_{x=L_o+L_w} = 0 \tag{2.5}$$

where Eq. 2.4 is used for the case in which micelles are present in the sublayer adjoining the aqueous/solid interface and Eq. 2.5 is used when the micelle concentration drops to zero in this sublayer. At the oil-water interface, surfactant monomer adsorbs from the aqueous subphase onto the surface, and further desorbs from the surface into the oil phase. The monomer surface density is denoted as $\Gamma(t)$. We will neglect the direct adsorption of micelles onto the surface from the aqueous subphase. This route can be an important component of the transport at high micellar concentrations where micelles remain in the sublayer and have direct access to the surface (cf. Fig. 2.1(a) and [11, 12]). However, in the regime of low micelle concentration studied here (Fig. 2.1(b)), the micelle-free zone develops immediately and only monomer is present in the subphase. This is because of the high partition coefficient of monomer into the oil from the aqueous subphase and the fact that the oil does not initially contain surfactant. The transport of monomer from the aqueous side to the oil/water interface and from the interface to the oil are kinetic steps which can in principle be formulated in terms of two kinetic equations, one for each side. The kinetic steps are usually faster than diffusion [32, 33], and to simplify the formulation here we assume that both the oil and aqueous sublayers are in equilibrium with the surface concentration. This can

be cast as two separate isotherms; here we use Langmuir isotherms as suggested by Liggieri et al [10]. The Langmuir isotherms do not include the effect of intermolecular interactions in the adsorbed layer. While, it could be presumed that intermolecular interactions are relatively weak (relative to monolayers at the air/water interface) because the oil molecules in the subphase tend to insert themselves between the chains and separate the amphiphiles, this fact has not been established. In the context of this study, however, it is important to note that the large partition coefficient of the surfactant in the oil is the predominant effect in determining the rate of transport of monomer from the aqueous to the oil phase, and the movement of the micelle-free zone boundary. The large partition coefficient maintains a value for the sublayer concentration of monomer in the micelle-free zone at the oil/water boundary ($C_w^m(L_o, t)$, see Figure 2.3(b)) which is significantly less than the CMC. The driving force for the movement of the micelle-free zone is the difference between the monomer concentration on the micelle-free zone side of the boundary (which is equal to the CMC) and the monomer concentration on the aqueous side of the oil/water interface (which is much less than the CMC). Including intermolecular interaction effects - with still a large partition coefficient - will not change the fact that the monomer concentration at the interface will still remain much less than the CMC, and as such the progression of the boundary with time will not change appreciably.

$$\Gamma(t) = \Gamma_\infty \cdot \frac{\beta_w C_w^m(L_o, t)}{\beta_w C_w^m(L_o, t) + \alpha_w} \tag{2.6}$$

$$\Gamma(t) = \Gamma_\infty \cdot \frac{\beta_o C_o(L_o, t)}{\beta_o C_o(L_o, t) + \alpha_o} \tag{2.7}$$

where α_o and β_o are the desorption and adsorption constants, respectively, for the oil side and α_w and β_w are these constants for the water side. where, and Γ_∞ is the maximum packing density. The partition coefficient K_p for surfactant monomer is

obtained from the above two equations

$$K_p = \frac{C_o(L_o,t)}{C_w^m(L_o,t)} = \frac{\beta_w \alpha_o}{\beta_o \alpha_w} \tag{2.8}$$

In coding the problem it is easier to use the partition relation (Eq. 2.8) and either the water or aqueous side Langmuir equations of which we choose the water side (Eq. 2.6). Finally the balance of diffusive fluxes across the surface is set equal to the rate of change of the surface concentration.

$$\frac{\partial \Gamma}{\partial t} = \sigma D_w^{mic} \left[\frac{\partial C_w^{mic}}{\partial x}\right]_{x=L_o^+} - D_o \left[\frac{\partial C_o}{\partial x}\right]_{x=L_o^-} \tag{2.9}$$

$$\frac{\partial \Gamma}{\partial t} = D_w^{m} \left[\frac{\partial C_w^{m}}{\partial x}\right]_{x=L_o^+} - D_o \left[\frac{\partial C_o}{\partial x}\right]_{x=L_o^-} \tag{2.10}$$

where Eq. 2.9 is used for the (short) period of time in which micelles are in the sublayer and Eq. 2.10 is used for times after the micelle-free zone has formed.

At the boundary $x = L_o + L_{zone}$ between the micelle-free zone and the micelle zone, the diffusive flux of monomer delivered to the boundary by micelles on the micelle side is equal to the diffusive flux of monomer delivered from the boundary on the the micelle-free zone side.

$$\sigma D_w^{mic} \left[\frac{\partial C_w^{mic}}{\partial x}\right]_{x=L_o+L_{zone}} = D_w^{m} \left[\frac{\partial C_x^{m}}{\partial x}\right]_{x=L_o+L_{zone}} \tag{2.11}$$

In addition, the micelle concentration is equal to zero at the boundary, and the monomer concentration is equal to the CMC.

$$\begin{aligned} C_w^m(x = L_o + L_{zone}, t) &= C_{\text{CMC}} \\ C_w^{mic}(x = L_o + L_{zone}, t) &= 0 \end{aligned} \tag{2.12}$$

At the beginning of the process, surfactant is present only in the aqueous phase,

$$\begin{aligned} C_o(x, t=0) &= 0 \qquad (0 < x < L_o) \\ C_w^m(x, t=0) &= C_{\mathrm{CMC}} \quad (L_o < x < L_o + L_w) \\ C_w^{mic}(x, t=0) &= (C_b - C_{\mathrm{CMC}})/\sigma \quad (L_o < x < L_o + L_w) \\ \Gamma(t=0) &= \Gamma^0 \end{aligned} \tag{2.13}$$

where, as before, C_b is the initial total bulk concentration of surfactant. The initial surface concentration $\Gamma(t = 0) = \Gamma^0$ is given by the equilibrium surface density of an air/water interface at the bulk concentration C_b. For the $C_{14}E_6$ surfactant used in this study, the dynamic and equilibrium adsorption onto the air/water interface has been studied [12]: From measurements of the equilibrium tension as a function of concentration and the modeling of these measurements using adsorption isotherms, the equilibrium adsorption on the surface for concentrations up to the CMC can be calculated. Above the CMC, we assume the equilibrium adsorption changes negligibly, and hence the adsorption at the CMC is used for Γ^0. The above formulation makes clear an important point that the distribution of surfactant monomer in the micellar phase (σC_w^{mic}) is independent of the number of monomers per micelle.

To solve these equations, a front trapping method is used in which a new variable C_w is introduced, which is the total bulk concentration in the aqueous phase and is defined as,

$$C_w = C_w^m + \sigma \cdot C_w^{mic} \tag{2.14}$$

The governing equation for the aqueous phase, valid over the entire aqueous domain, in terms of this total concentration becomes,

$$\frac{\partial C_w}{\partial t} = \frac{\partial}{\partial x}\left(D_w(C_w)\frac{\partial C_w}{\partial x}\right) \qquad (L_o < x < L_o + L_w) \tag{2.15}$$

where $D_w(C_w)$ is a piecewise continuous step function, which is equal to the monomer diffusivity when $C_w < C_{\mathrm{CMC}}$ and equal to the micelle diffusion coefficient for $C_w > C_{\mathrm{CMC}}$. The flux boundary conditions at the aqueous/solid and aqueous/oil interfaces can easily be recast in terms of the total bulk concentration in Equations 2.4, 2.5, 2.9 and 2.10. The initial conditions on the concentrations in Eq. 2.13 can also be reformulated in terms of C_w. The boundary conditions at the micelle-free/micelle zone (Equations 2.11 and 2.12) are satisfied through the numerical scheme (see below).

The system of equations in terms of C_w is solved numerically with a finite volume method of discretization in which the space domain was discretized into N equal sized control "slices" over which the mass balance (Eq. 2.15) is satisfied. The micelle-free zone boundary is identified as the point at which $C_w = C_{\mathrm{CMC}}$, which lies in general within one of the control slices. The mass balance on the surface of this control slice is reformulated to accommodate the fact that within the volume, the micelle concentration is zero at the boundary and the monomer concentration is equal to C_{CMC} (Eq. 2.12). The details of the numerical solution are presented in Appendix A, along with a verification of the code.

In undertaking the simulations for comparison to the experiments with $C_{14}E_6$, the following parameter values are used: The partition coefficient K_p is set equal to 350 as directly measured (see Chapter 3 Appendix A). Because of the assumption of kinetic equilibrium at the oil/water interface, we require only the partition coefficient, maximum packing density (Γ_∞) and the ratio of the desorption to the adsorption rate constants on the water side (α_w/β_w). Here we use a value of 8.35×10^{-6} mol/m^3 for α_w/β_w and 2.4×10^{-6} mol/m^2 for Γ_∞ as given by Song [12], corresponding to a Langmuir fit of the equilibrium adsorption to an air/water interface of this surfactant. While this ratio is not necessarily the same as at the oil/water interface, because the partition coefficient is so large, the monomer concentration of surfactant in the water at the interface is usually small during the transport and the numerical results are not

sensitive to the value of α_w/β_w. $C_{\mathrm{CMC}} = 0.009$ mol/m^3 and the monomer diffusivity in water is set equal to $D_w^m = 4\times10^{-10}$ m^2/s, which is in the range of values reported for similar surfactants (3.9×10^{-10} m^2/s for $C_{10}E_5$ using pulsed field gradient NMR [34] and 3.7×10^{-10} m^2/s for $C_{12}E_8$ using a radiotracer method [35]). For the diffusion coefficient of the aggregates, values measured in the high concentration regime for extended rods of $C_{14}E_6$ are in the range of 0.1 - 0.5×10^{-10} m^2/sec. For the dilute concentration range studied here, larger values are expected since the aggregates are most likely short rods. From the studies of Tiberg et al. [36, 37] for $C_{14}E_6$ at dilute concentrations (1-20$\times C_{\mathrm{CMC}}$), a value for the micelle diffusion coefficient of $(1/4)D_w^m$ was found, which corresponds to a value of 1.0×10^{-10} m^2/s given the monomer diffusion coefficient used. This aggregate diffusion coefficient is very close to the value measured by pulsed field gradient NMR by Brown et al [38, 39, 40] for globular $C_{12}E_6$ aggregates and for the more spherical micelles of $C_{14}E_8$ measured by dynamic light scattering by Richtering et al[41]. Simulation results for reduced values of the micelle diffusion coefficient, with all other transport values remaining unchanged, demonstrate that only when the micelle diffusion coefficient becomes less than 0.1×10^{-10} m^2/s (much smaller than would be expected, given the measurements at high concentrations) is there any noticeable effect on the movement of the zone boundary relative to the result for 1.0×10^{-10} m^2//s . This indicates that the monomer diffusion in the micelle-free zone is the more rate controlling, and any ambiguity in the value of the micelle diffusion coefficient is unimportant. The monomer diffusivity in oil, D_o, is set equal to the diffusion coefficient in water, multiplied by the ratio of the viscosity of water (1 cP) to the viscosity of hexadecane (3 cP)[42] in accordance with the Stokes-Einstein relationship. From the experimental conditions (presented later in the report), $L_o = 300\mu$m, and $L_w = 1.9$ mm and the respective initial bulk concentrations in the aqueous phase are $1.5\times C_{\mathrm{CMC}}$ and $2\times C_{\mathrm{CMC}}$.

2.3 Simulation Results

Fig. 2.3 shows the numerical results obtained from the simulations for $2\times C_{\mathrm{CMC}}$ initial concentration. In Fig. 2.3(a) and Fig. 2.3(b) are plotted, for different times, the micelle and monomer concentrations, where the concentrations are nondimensionalized by C_{CMC}. In calculating the micelle concentration, a value of $\sigma = 100$ monomers per micelle has been assumed; recall the distribution of the concentration of monomers in micelles (or the amount of surfactant in micelle form), as all of the numerical calculations, is independent of σ. The range plotted for the "x" coordinate corresponds to the total thickness of the aqueous phase. The micelle distribution shows the emergence and growth of the micelle-free zone as a function of time as the moving spatial position where the micelle concentration becomes equal to zero. For early times (less than or equal to 451 sec, marked (i), (ii) and (iii) in Fig. 2.3(a)) in which the aqueous/solid interface is far from the boundary between the micelle zone and the micelle-free zone and the micelle region constitutes an "infinite" bulk phase, the micelle concentration is equal to the initial concentration except immediately near the boundary where the concentration drops sharply to zero. This distribution resembles the error function solution for diffusion of a solute from an infinite phase with a uniform bulk concentration to an interface where the solute concentration is maintained at a value equal to zero. As time progresses ((iv) and (v), 1128 and 2256 sec), the boundary between the micelle and micelle-free zones approaches the aqueous/solid wall, the distribution begins to reflect the zero flux condition at the wall as the micelle transport is no longer from an infinite solution, and as such the distribution broadens. Eventually, the concentration at the aqueous/solid wall drops significantly below the bulk value (see the distribution marked (vi) at 4512 sec). For even longer times, the micelle-free zone merges with the wall and there are no micelles in the aqueous phase. The corresponding concentration of monomer in the micelle-free zone shows for the early times (marked (i), (ii), (iii) and (iv)) a linear gradient with the

concentration ranging from a nondimensional value of one at the micelle-free zone – micelle zone boundary to a value of zero at the oil/water interface. The value of zero at the oil/water interface is due to the large partition coefficient of surfactant into the oil, and is in fact maintained for all times of the simulation. The linear profile in the micelle-free zone at the early times is due to the fact that during these early times the thickness of the micelle-free zone L_{zone} is small relative to the aqueous phase L_w. This fact, taken together with the fact that the micelle diffusion coefficient is one-quarter of the monomer diffusion coefficient, requires that the time scale for diffusion of monomer in the micelle-free zone ($\tau_D^m = L_{zone}^2/D_w^m$) is small relative to the overall time scale of diffusion of micelles through the aqueous phase ($\tau_D^{mic} = L_w^2/D_w^{mic}$). Hence the diffusion in the micelle-free zone progresses quasi-statically. For longer times as the micelle-free zone penetrates deeply into the aqueous phase the time scale for diffusion of monomer grows comparable to the diffusion of micelles in the micelle-zone and the monomer diffusion is no longer quasi-static with a linear gradient. Fig. 2.3(c) shows the dimensionless total concentration in both oil and water phases. The discontinuity in the slope of the total concentration gradient in the aqueous phase when $C_w = C_{\mathrm{CMC}}$ (the boundary between the micelle-free zone and the micelle zone) is a result of Eq. 2.11, and the larger slop in the micelle zone follows since the micelle diffusion coefficient is smaller than that of the monomer. (Note if the micelle concentration rather than the total concentration had been plotted, the slope would have been smaller in the micelle zone because the micelles deliver σ monomer per micelle to the interface which offsets the reduced diffusion coefficient of the micelles.) The concentration distribution of surfactant (monomer) in the oil phase as shown in Fig. 2.3(c) shows an increasingly larger value in the oil sublayer next to the oil/water interface, as well as a penetration of surfactant into the oil phase, as oil starts picking up the surfactant monomers from the oil-water interface. The concentration distribution in the oil phase is not quasi-static (and hence the distribution is not flat): Although

the oil depth (L_o) is small, and of the same size as the micelle-free zone when its distribution of surfactant is linear and quasi-static, because the diffusion coefficient of the surfactant in the oil (D_o) is one third of that in the aqueous phase, the time scale for diffusion in the oil is three times longer. Hence quasi-static conditions do not prevail; larger values for the diffusion coefficient of the monomer in the oil would be necessary to achieve a flat profile. In Fig. 2.3(d), the micelle-free zone boundary position is plotted against time for the two bulk concentrations $C_b = 1.5 \times C_{\mathrm{CMC}}$ and $C_b = 2 \times C_{\mathrm{CMC}}$. The micelle-free zone reaches the aqueous/solid interface in a finite time. As expected, when the initial bulk concentration of surfactant in the aqueous phase is increased from $1.5 \times C_{\mathrm{CMC}}$ to $2 \times C_{\mathrm{CMC}}$ the micelle free zone progresses more slowly in time, and the zone requires a longer time to reach the aqueous/solid boundary. For the larger initial concentration of micelles, the diffusive flux to the boundary between the micelles and the micelle-free zone is greater and it takes a longer time for this boundary to travel a certain distance. Equivalently, for the higher initial concentration more surfactant has to be transferred into the oil phase through the micelle-free zone, and this takes a longer time. The movement of the zone displays three time scales: In the beginning (for $2 \times C_{\mathrm{CMC}}$, between 0- 451 sec, see (i)-(iii) in Fig. 2.3(a)) the velocity of the interface between the two zones is large because of the large gradients in the micelle concentration at the early times. This is characteristic of the error function distributions as the micelle-zone is effectively an infinite reservoir and only micelles in the micelle zone near the interface between the zones becomes depleted. In the second stage (for $2 \times C_{\mathrm{CMC}}$, between 451-4512 marked as (iv)-(vi) in Fig. 2.3(a)), the velocity of movement of the interface between the two zones slows down for two reasons. First the flux of monomers at the boundary decreases because the distance over which the concentration gradient in the micelle-free zone is exerted (L_{zone}) increases. Secondly, the micelle zone is no longer an infinite reservoir and the micelle distribution broadens as the zero-flux condition at the aqueous/solid

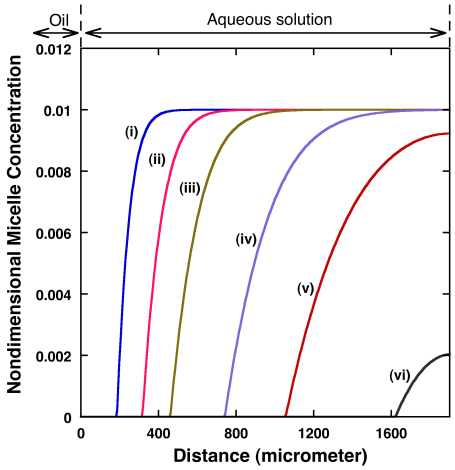

(a) Nondimensional micelle concentration $C_w^{mic}/C_{\mathrm{CMC}}$ distribution with distance (in micrometers) from the oil-water interface.

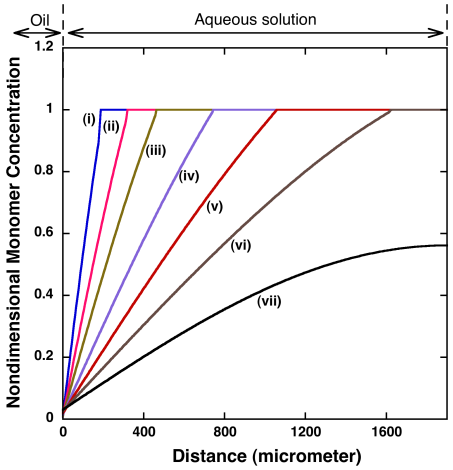

(b) Nondimensional monomer concentration C_w^m/C_{CMC} distribution with distance (in micrometers) from the oil-water interface.

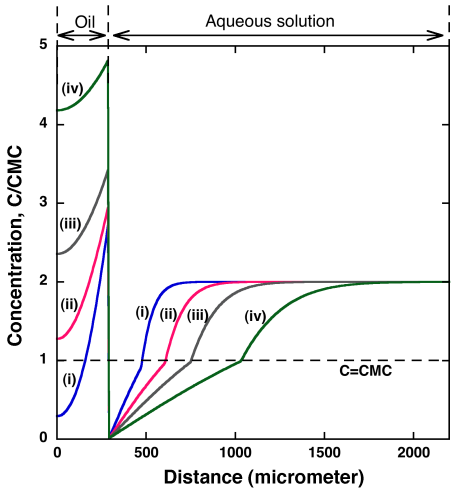

(c) Nondimensional total concentration C_w/C_{CMC} distribution with distance (in micrometers) from the air-oil interface.

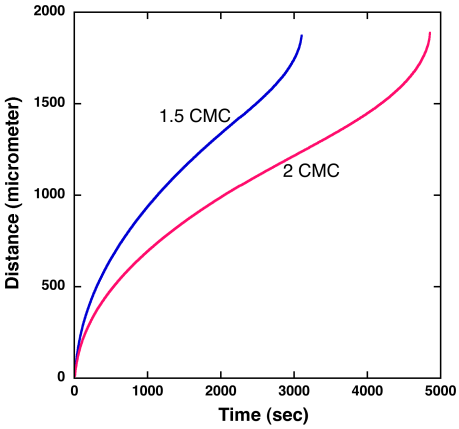

(d) Micelle-free zone boundary position (in micrometers) from the oil-water interface plotted against time (in seconds) for different initial concentrations.

Figure 2.3: Simulation results for $C_{14}E_6$ surfactant at different time intervals (i) 90sec, (ii) 226sec, (iii) 451sec, (iv) 1128sec, (v) 2256 sec, (vi) 4512 sec and (vii) 6769 sec. Initial aqueous phase concentration in Fig. (a), (b) and (c) is 2CMC.

wall begins to exert an effect. Finally in the last stage (greater than 4512 sec for $2 \times C_{\mathrm{CMC}}$), as the micelle-free zone approaches the aqueous/solid wall, the velocity of the interface between the two zones accelerates. In this last stage the concentration of micelles in the micelle-zone is small relative to the initial bulk value. In addition, the flux of surfactant through the zone interface becomes approximately stationary as the driving force on the micelle-free zone side (nondimensionally one in concentration difference) is constant and the distance over which this driving force acts approaches L_w. These two conditions accelerate the movement of the micelle-free zone, as can be understood by writing the mass balance of surfactant on the micelle zone,

$$\frac{d}{dt}\left[\bar{C}_w(t)[L_w - L_{zone}(t)]\right] = -f \tag{2.16}$$

$$\bar{C}_w(t)[L_w - L_{zone}(t)] = f(t_o - t) \tag{2.17}$$

where f is the flux, t_o is the time at which the micelle-free zone reaches the solid surface and

$$\bar{C}_w(t) = \frac{\int_{L_w - L_{zone}(t)}^{L_w} C_w(x,t)dx}{L_w - L_{zone}(t)} \tag{2.18}$$

is the average total concentration of surfactant monomer in the micelle zone. A scaling relationship for the flux through the interface can be written as

$$f \propto D_w^{mic} \frac{\bar{C}_w(t)}{L_w - L_{zone}(t)} \tag{2.19}$$

and hence

$$[L_w - L_{zone}(t)] \propto (t_o - t)^{1/2} \tag{2.20}$$

$$\frac{d}{dt}[L_{zone}(t)] \propto (t_o - t)^{-1/2} \tag{2.21}$$

These arguments show that the velocity diverges as $(t_o - t)^{-1/2}$ as $t \to t_o$ explaining the rapid acceleration in the movement of the zone boundary as the micelle-free zone approaches the wall (Fig. 2.3(d)). Plotting $(L_w - L_{zone})$ as a function of $(t_o - t)^{1/2}$ as $t \to t_o$ a linear relationship is evident confirming the scaling hypothesis (Fig. 2.4).

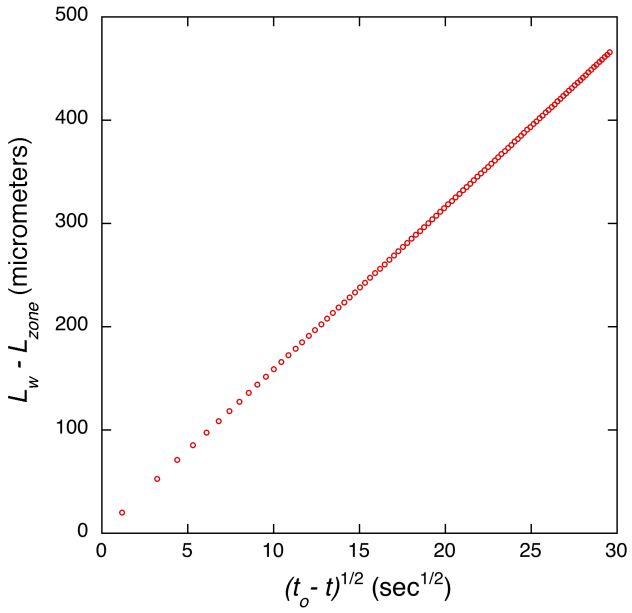

Figure 2.4: Distance of a micelle-free zone boundary position from the aqueous/solid interface $(L_w - L_{zone})$, as obtained from the numerical simulations, plotted against $(t_o - t)^{1/2}$ for the initial aqueous phase concentration of $2 \times C_{\mathrm{CMC}}$. A linear fit confirms the scaling hypothesis and explains the rapid acceleration of the boundary movement as it approaches solid wall.

2.4 Conclusion

A 1-Dimensional two-zone transport model has been developed for the transport of surfactant from an aqueous micellar solution to an initially clean oil phase, in the limit of fast kinetics of micelle disassembly and adsorption at the oil/water interface. At low micelle concentration, the model shows presence of two distinct zones, a micelle zone and a micelle free zone. Conditions are arranged such that micelle free zone grows with time and finally spans the entire aqueous phase. Model transport equations

were solved numerically with a finite volume method to obtain micelle and monomer concentration distribution in both phases, from which a boundary position separating micelle and micelle-free zones can be obtained as a function of time. The boundary first appears near the oil/water interface and with time propagates into the aqueous phase depleting more and more micelles till finally merges with the aqueous/solid wall. Parameters used in the simulations were obtained from experimental studies with $C_{14}E_6$ surfactants and conditions are arranged very close to the experimental set-up as presented in the following chapter, so that a comparison could be made for the boundary position movement obtained from simulations and experiments.

Appendix A. Numerical implementation of Finite Volume Method and Code Validation

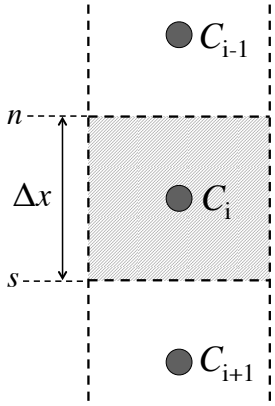

Figure A.1: A typical control volume around i^{th} node of length Δx, enclosed by two boundaries top/north side n and bottom/south side s.

A fully implicit finite volume method is used to solve the system of equations outlined in the Numerical Simulation section. In this method, the entire bulk volume including both the oil and the aqueous phases is divided into N equal-sized control volumes. In each of these control volumes a material balance is satisfied. Fig.A.1 shows a typical i^{th} control volume counting from the oil-air interface, for example in the aqueous phase, where the length of the control volume is Δx and n and s are the north and south side enclosing boundaries. Discretized algebraic equations can be obtained from integration of the governing equation, Eq. 2.15, over the control volume for a small time step of Δt as;

$$\int_n^s \int_t^{t+\Delta t} \frac{\partial C_w}{\partial t} dt \cdot dx = \int_t^{t+\Delta t} \int_n^s \frac{\partial}{\partial x} \left(D_w \frac{\partial C_w}{\partial x} \right) dx \cdot dt \tag{A.1}$$

which yields,

$$\left(C_i - C_i^0\right) \cdot \Delta x = \left[\left(D_w \frac{\partial C_w}{\partial x} \right)_s - \left(D_w \frac{\partial C_w}{\partial x} \right)_n \right] \cdot \Delta t \tag{A.2}$$

where superscript "0" refers to the known quantities from the earlier time step. The diffusive fluxes at the south and north boundaries are approximated as follows,

$$\left(C_i - C_i^0\right) \cdot \Delta x = \left[D_s \frac{C_{i+1} - C_i}{\Delta x} - D_n \frac{C_i - C_{i-1}}{\Delta x} \right] \cdot \Delta t \tag{A.3}$$

In the above equation, D_s and D_n refers to the diffusivity function evaluated at the boundary position, which is a piecewise continuous step function as mentioned before and is dependent on the total concentration C_w at nodes immediately before and after that boundary. For instance for evaluation of D_s, if both $C_i >$ CMC and $C_{i+1} >$ CMC then $D_s = D_w^{mic}$; similarly if both $C_i <$ CMC and $C_{i+1} <$ CMC then $D_s = D_w^m$. However, if $C_i <$ CMC and $C_{i+1} >$ CMC, meaning that the micelle-free zone is present in between the two nodes i and $i+1$, the diffusivity across the boundary between these two nodes is calculated by first matching the micelle flux to the disassembly boundary and monomer flux away from the boundary to formulate an equation for the boundary position. If ϕ is a fractional distance between the nodes i and $i+1$ occupied by the micelle-free zone (which could be approximated by linear interpolation in the total concentration to find the position for which $C_w = C_{\text{CMC}}$), then flux matching condition at the disassembly boundary gives $D_s = (\phi/D_w^m + (1-\phi)/D_w^{mic})^{-1}$. This is the front trapping method, where we solve the governing equation in terms of total concentration but the front of the micelle-free zone is trapped and fluxes on both sides of this front are matched so that the continuity equation is satisfied. Therefore, Eq. A.3 can in general be written as,

$$a_{i-1}C_{i-1} + a_i C_i + a_{i+1}C_{i+1} = b_i \tag{A.4}$$

where a's and b's are constants known from previous iteration. Similar algebraic equation can be written for the oil phase.

At the interfacial node we have three unknowns; namely the surface concentration,

water sublayer concentration and oil sublayer concentration. If our i^{th} control volume as shown in Fig. A.1 is at the interfacial node, then we have the following three equations to be solved simultaneously,

$$\frac{\partial \Gamma}{\partial t} = D_w \left[\frac{\partial C_w}{\partial x}\right]_s - D_o \left[\frac{\partial C_o}{\partial x}\right]_n \tag{A.5}$$

$$\Gamma(t) = \Gamma_\infty \cdot \frac{\beta_w C^m_{w,i}}{\beta_w C^m_{w,i} + \alpha_w} \tag{A.6}$$

$$C_{o,i} = K_p \cdot C_{w,i} \tag{A.7}$$

Discretizing Eq. A.5 and using Eq. A.7 to write oil concentrations at the interfacial node in terms of water sublayer concentration, we get,

$$\frac{\Gamma - \Gamma^0}{\Delta t} = D_w \frac{C_{w,i+1} - C_{w,i}}{\Delta x} - D_o \frac{K_p \cdot C_{w,i} - C_{o,i-1}}{\Delta x} \tag{A.8}$$

The non-linearity in the Langmuir isotherm, Eq. A.6, can be removed by linearizing it,

$$\Gamma = \Gamma^0 + \left.\frac{\partial \Gamma}{\partial C^m_w}\right|^0 \Delta C^m_w$$

$$(\Gamma - \Gamma^0) = \frac{\beta/\alpha \cdot \Gamma_\infty}{\left(\beta/\alpha \cdot C^0_{w,i} + 1\right)^2} \cdot (C_{w,i} - C^0_{w,i}) \tag{A.9}$$

Using Eq. A.8 and Eq. A.9 one can obtain a linear algebraic set of equations of the same form as Eq. A.4. Thus, the generated system of linear equations can be written in the matrix form such as $\underline{\underline{A}} \cdot \underline{c} = \underline{b}$, where $\underline{\underline{A}}$ is a tri-diagonal coefficient matrix of $N \times N$, $\underline{c}$ and $\underline{b}$ are the unknown concentration vector and known constant vector (of $N \times 1$ each) respectively. This $\underline{\underline{A}}$ matrix can be easily inverted with the tri-diagonal solver using FORTRAN to solve for the unknown concentrations at each node from which the micelle-free zone boundary position can be obtained.

For the code validation purpose, consider an aqueous phase of length L with

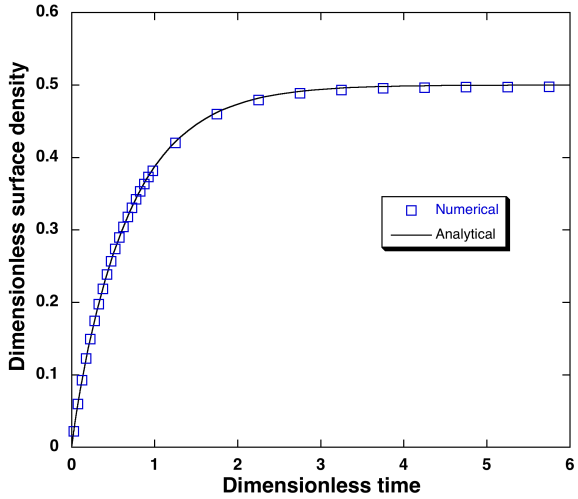

Figure A.2: Comparison between $\tilde{\Gamma}(\tau)$ obtained from analytical solution, Eq. A.13, and that obtained numerically with parameters $K = N_d = N_l = 1$

an impenetrable bottom, with initially a uniformly distribution of surfactant at a concentration below the CMC, exposed to an initially clean air-water interface. In this case there is no oil phase involved, but the clean air-water interface drives the transport process. Adsorption at the air-water interface has been modeled with a linear kinetic scheme. Thus in this simplified case, the governing equations and the boundary conditions are as follows,

$$\frac{\partial C_w}{\partial t} = D_w \frac{\partial^2 C_w}{\partial x^2} \qquad (0 < x < L) \tag{A.10}$$

$$\frac{d\Gamma}{dt} = \beta C_w(x=0)\Gamma_\infty - \alpha\Gamma = D_w \left[\frac{\partial C_w}{\partial x}\right]_{x=0} \tag{A.11}$$

and

$$D_w \left[\frac{\partial C_w}{\partial x}\right]_{x=L} = 0 \tag{A.12}$$

Initial conditions are $\Gamma(t=0) = 0$ and $C_w(x, t=0) = C_{bulk}$. An exact solution for

this problem is obtained by Laplace transform which in dimensionless form is,

$$\tilde{\Gamma}(\tau) = \frac{k}{N_l k + 1} - \sum_{n=1}^{\infty} \frac{2k^2 N_l e^{-\beta_n^2 \tau}}{[(N_l k + 1) - (2N_d - N_l^2 k^2 - N_d N_l k) \cdot \beta_n^2 + N_d^2 \beta_n^4]} \tag{A.13}$$

where $\tilde{\Gamma} = \Gamma/\Gamma_\infty$, $\tau = D_w t/L^2$, $N_d = D_w/(L^2\alpha)$, $N_l = \Gamma_\infty/(C_{bulk}L)$, $k = \beta C_{bulk}/\alpha$ and β_n's are the roots of the equation,

$$\frac{N_l k \beta_n}{(N_d \beta_n^2 - 1)} = \tan \beta_n \tag{A.14}$$

$\tilde{\Gamma}(\tau)$ obtained from this relation compared well with that obtained from the finite volume method code, Fig. A.2. In this simulation, $N = 100$ and $\Delta\tau = 1 \times 10^{-3}$ were used however for N larger than 40 numerical results do not change much. For the actual simulations involving micellar transport, $N = 400$ and non-dimensional time step of $\Delta\tau = 5 \times 10^{-4}$ were used in order to resolve the micelle-free zone boundary movement accurately.

Chapter 3

Experimental Studies of Surfactant Transport

In this chapter, experimental studies of surfactant transport from an aqueous micellar solution to an initially clean oil phase are presented in order to verify the presence of micelle-free zone and the two zone model presented in previous chapter. In undertaking these experiments, region containing micelles is fluorescently demarcated. This is achieved by dissolving a small hydrophobic dye molecule, Nile Red, in the micellar aqueous solution. The dye partitions strongly into the micelle interior, and, upon excitation, only fluoresces when in the hydrophobic environment of the micelle. The fluorescence is quenched when the dye is in water. This provides the fluorescent contrast between the zones, and we use confocal microscopy, imaging at different depths underneath the interface, to quantitatively measure the depth of the micelle-free zone underneath the oil/water interface as surfactant transports to the oil and the micelle-free zone moves away from the interface.

3.1 Materials and Methods

The surfactant used, poly (ethylene glycol) n-alkyl monoether, $CH_3(CH_2)_{13}(OCH_2CH_2)_6OH$ ($C_{14}E_6$) was obtained from Nikko Chemicals, Japan and its aqueous solutions were prepared from deionized water purified by a Milli-Q filter system equipped with an Organex-Q column to remove trace organic contaminants (Millipore, MA, USA). The resistivity of the deionized water was approximately 18 MΩcm. The dye used was Nile Red (Molecular Probes, Inc., Eugene, OR, USA) which was first dissolved in ethanol (Reagent grade, Sigma-Aldrich, St. Louis, MO, USA) before adding to the aqueous surfactant solution. The Nile Red concentration in the surfactant solutions was maintained at 0.2 μg/ml, within its water solubility limit (< 1 μg/mL). The oil used, hexadecane, >99% purity, was obtained from Acros Organics, NJ, USA. All chemicals were used as received without further purification

An inverted confocal laser scanning microscope (CLSM; Leica TCS SP2, employing an acoustic-optical beam splitter (AOBS) and a prism spectrophotometer detector; 63× (dry) objective, NA = 0.7), was used for the epifluorescent detection of the emission from the Nile Red. The surfactant solution with Nile Red was excited with two laser lines, 514 and 543 nm. After spectral decomposition of the light returned from the sample with a prism, the Nile Red luminescence is collected onto a photomultiplier tube (PMT) by using a window of collection between 580-750 nm. Simultaneously, through a separate optical train and PMT tube, the reflected light from the sample is recorded by using a collection window between 519-525 nm, which just excludes the 514 excitation wavelength, but still records reflected light of the 514 nm line because the excitation line is not perfectly sharp and and the tail of the line bleeds through into the collection window. Chamber slides were used to enclose the oil/water interface and position the interface under the objective of the microscope; these slides (Lab-Tek chamber slides, Electron Microscopy Sciences, Hatfield, PA) consisted of two chambers, made of plastic walls attached to a soda lime glass micro-

scope slide, $\sim$160μm thick. The size of each chamber was 20$\times$24 mm in width and length of the base and 10 mm high, and could be enclosed by a plastic lid. During the course of experiments, the plastic lid was placed on the chamber to reduce evaporative effects. The chamber slides, the quartz curvettes and all glassware contacting the surfactant solutions for their preparation (and for measurements of the partition coefficient, see Appendix A) were cleaned by immersing in ethanol, sonicating and then sonicating with water from the Milli-Q system. All experiments were undertaken at room temperature, 20-23°C.

3.2 Experimental Design

To use confocal laser scanning fluorescence microscopy to visualize the micelle and micelle-free zone in the aqueous phase underlying the oil as the surfactant transport proceeds (Fig. 2.1(b)), we arranged conditions so that the micelle-free zone is sufficiently large so as to be clearly discerned. If the surfactant strongly partitions into the oil phase relative to water, then the adsorption into the oil can provide a large capacity for removing the surfactant from the aqueous phase and creating a large micelle-free zone. In the limiting case where the oil volume and partition coefficient are large enough and the amount of surfactant in the aqueous phase is small enough, partitioning into the bulk can drive a micelle free-zone which extends throughout the water volume at equilibrium as the equilibrium concentration of surfactant in the water is lowered to below the CMC when in contact with the oil. These are in fact the conditions we set in the experimental arrangement, as described in the following. As with Song et al. [12], we utilized the polyethoxylated surfactant $C_{14}E_6$ ($CH_3(CH_2)_{13}(OCH_2CH_2)_6OH$). The phase behavior of the $C_{14}E_6$ polyethoxylate has been studied by Einaga et al [43, 44] and also by Kato et al [45, 46] using static and dynamic light scattering and pulsed field gradient (PFG) spin echo. It is important

to note that these studies are at high concentrations of surfactant, >0.001 g/cm^3 or >200 CMC. This range is two orders of magnitude larger than the concentration used in this study. Einaga et al and Kato et al show that, for these high concentrations, as temperature and concentration increase, aggregates grow into long thread or worm like micelles (sphero-cylinders, rods with spherical caps). As the temperature is increased and approaches the lower consulate temperature (cloud point) (the point at which a concentrated solution separates from the isotropic phase) these extended structures can entangle to form a network. ($C_{14}E_6$ has a consulate temperature of approximately 41°C.) At the high concentrations, Einaga et al and Kato et al report measurements of the micelle diffusion coefficients for these worm-like micelles in the range of 0.1 - 0.5$\times 10^{-10}$ m^2/sec. Since the size of the aggregates increases with concentration, we may expect in our study, which is at much lower concentrations, short rods or spheroids, with a diffusion coefficient larger than approximately 0.5$\times 10^{-10}$ m^2/sec. The shapes are more likely short rods, as may be reasoned from the fact that for a shorter chain polyethoxylates, $C_{12}E_6$ and $C_{12}E_8$, Brown et al have shown approximately globular micelles in the very dilute regime of 1-20 CMC using light scattering and PFG-NMR measurements [38, 39, 40]; the longer chains of $C_{14}E_6$ with therefore a larger hydrophobic volume should extend the globules to short rods. In addition, $C_{14}E_8$, with a larger head group, shows, using dynamic light scattering[41] spherical micelles with a radius of 3.7 nm and 119 monomers per micelle for high concentrations (2000-70000$\times C_{\mathrm{CMC}}$) and so for $C_{14}E_6$ with a smaller headgroup it can be similarly concluded that small rods can be expected for the more dilute concentrations. The critical micelle concentration of $C_{14}E_6$ is equal to 0.009 mol/m^3 [12]. In separate experiments (see Appendix A), the equilibrium partition coefficient of $C_{14}E_6$ between a submicellar solution and hexadecane was measured, and a value of 350 (concentration of surfactant in oil to the concentration in the aqueous phase) was obtained. For the bulk concentrations of surfactant which will be used (1.5$\times C_{\mathrm{CMC}}$ and

$2.0 \times C_{\mathrm{CMC}}$), and the oil (300 μl) and aqueous volumes (1.5 ml) used, and for this partition coefficient, the oil extracts at equilibrium enough surfactant so that the aqueous phase is below the CMC. As a result, the length scale for calculating the diffusion time of the monomer is the depth of the water film underneath the oil lens which for the volume of the aqueous phase used and the size of the chamber is 1.9 mm. For an aqueous phase of $\ell = O(1\mathrm{mm})$ and $D_w^m = O(10^{-10}\mathrm{m}^2/\mathrm{s})$[12], the diffusion time scale is $\tau_D^m = O(10^4 sec)$. The micellization disassembly kinetics for this surfactant has not been measured, but for the similar surfactants $C_{12}E_6$ and $C_{12}E_8$ which also form globular micelles, the stop flow technique has been used to measure τ_{SL} and values of 10 and 4 s, respectively, have been obtained [47, 48]. These kinetic timescales are much smaller than the diffusion time scale of the experiment, so the quasi-static assumption can be applied. The hexadecane oil was used as received. While >99% purity, surface active impurities were evident by the fact that the tension of the oil/water interface, as measured by pendant drop tensiometry (see Appendix A), relaxed to a value of 48 dyne/cm, compared to a reported value of 53.3 dyne/cm when the oil was cleaned of impurities by passing through a column[49]. These impurities did not produce an emulsification at the interface when oil and water were contacted to measure a partition coefficient, as described in Appendix A. As the simulations in the previous chapter made clear that the presence of impurities does not significantly affect the movement of the micelle-free zone boundary because the large partition coefficient of the surfactant into the oil forces the concentration of monomer on the aqueous side of the oil/water interface to be much less than the critical micelle concentration. Therefore the driving force for the movement of the boundary, the difference between the monomer concentration at the boundary (which is equal to the CMC) and the monomer concentration on the aqueous side of the oil/water interface (which is much less than the CMC) remains invariant during the retreat of the zone. During this retreat, the oil phase remains far from saturated, which also helps in maintaining the

monomer concentration on the aqueous side of the oil/water interface at a value much less than the CMC. In this regard, as the surfactant diffuses into the oil, aggregation phenomena in the oil (formation of a microemulsion or aggregated monomers in the oil) can take place, which would augment and accelerate the diffusive process into this phase. However, the fact that the monomer concentration on the aqueous side remains well below the CMC basically fixes the diffusive flux of monomer into the oil at its highest rate, and these other processes could not provide any higher rate. In addition, the maximum concentration of surfactant in the oil (assuming all the surfactant initially in the aqueous phase partitions into the oil) is only 0.025 weight percent, far below the one percent that appears necessary for aggregation of polyethoxylates in oils[50] or the formation of a microemulsion[51] which in addition usual requires vortexing and a co-surfactant[51], conditions not present in the experiment.

To fluorescently label the micelle zone, we use the small hydrophobic dye molecule, Nile Red (9-diethylamino-5H-benzo[α]phenoxazine-5-one, Fig. 3.1(a)). Nile Red dissolves readily in nonpolar organic solvents, but is only slightly soluble in water with a reported solubility of less than 1 μg/ml [52, 53, 54]. Because of the polar constituents on the molecule, the excitation and emission spectra of Nile Red are sensitive to the environment, and the peaks in these spectra are red shifted as the solvent becomes more polar. In addition, for the same concentration of dye, the emission intensity is approximately forty-fold less in water than in nonpolar solvents such as n-alkanes, as water quenches the fluorescence [54]. When the dye is added to a micellar solution, it strongly partitions into the hydrophobic domains of the micelles (as shown in Fig. 3.1(b)) where it strongly fluoresces [53]. Upon micelle disassembly, the dye is released into the aqueous medium, and its fluorescence is largely quenched. This property of the Nile Red can be exploited to visualize the micelle and micelle-free zones by detecting its emission in planes parallel to the oil/water interface as a function of distance from this interface, using confocal fluorescence microscopy. The amount of dye which

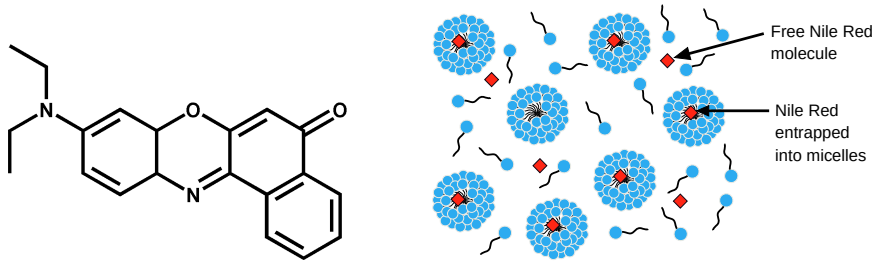

(a) Chemical structure of Nile Red

(b) Incorporation of Nile Red in the aggregates of a micellar surfactant solution

Figure 3.1: The Nile Red molecule and its partitioning into micelles.

is added to the submicellar and micellar solutions is 0.2 μg/ml. With this concentration of dye, for $2\times C_{\mathrm{CMC}}$ micellar solution, 7–8 dye molecules are available per micelle. However, the partitioning of this dye in nonpolar hydrocarbon phases has been reported to be approximately 200:1 [54]. Using this value the equilibrium concentration of dye in the micelles would correspond to approximately one dye molecule per 575 micelles, and the aqueous concentration of dye is 0.19995 μg/ml. (This calculation is done assuming for $C_{14}E_6$, $\sigma = 100$ and radius of the micelle hydrocarbon core is the all-trans extended length of 14 carbon atoms, 1.76nm.) Nonetheless, this low concentration of trapped Nile Red is sufficient to provide the fluorescent contrast between the micelle-free zone and micelle zone as demonstrated in our experiments. It is important to note that as this dye is also soluble in the hexadecane, it will diffuse into the oil phase with time, and while this causes the oil phase to luminesce (see Fig. 3.5), and a dimming of the fluorescence in the micelle-zone, it does not effect the location of the zone as the fluorescence contrast remains distinct.

The experimental arrangement is as shown in Fig. 3.2. A 1.5 ml aliquot of an aqueous micellar solution with Nile Red was placed in one of the chambers of the chamber slide. After sufficient time, a 40 μl aliquot of hexadecane was placed on top of the aqueous phase. The limited volume of oil used insures that the oil forms an approximately circular lens of about 15-17 mm in diameter which floats on the surface of aqueous phase. For this arrangement, the water thickness for the 1.5 ml aliquot

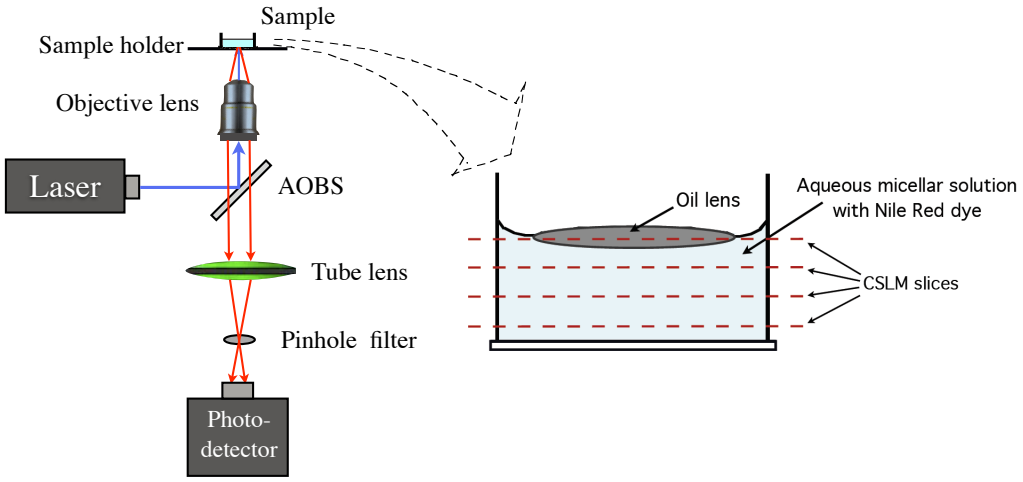

Figure 3.2: Experimental arrangement showing a schematic of the confocal laser scanning microscope, the water subphase, and the oil lens on the top of the aqueous solution.

in the chamber was approximately 1.9 mm and the oil thickness of the 40 μl aliquot of hexadecane was about 300 μm. As the water thickness is very small compared to the oil lens diameter, the transport of surfactant essentially takes place - at least initially - in only the direction normal to the surface. For later times, diffusion in the direction along the interface will become a factor and complicate the transport. While the deposition of an oil layer that spans the entire air/water interface of the chamber would eliminate this problem, these layers tended to spread down the plastic walls of the chamber , and a stable layer of oil on top of the water could not be realized. Treatments of the plastic did not prevent this spreading. It is for this reason that lenses were used. Lenses placed on the surface were found to be stable as the air/water tension with surfactant ($\approx$ 31 dyne/cm) is balanced by the oil/air ($\approx$ 27 dyne/cm and oil/water ($\approx$ 10–15 dyne cm) tensions (the latter also with surfactant) with a finite contact angle. The integrated epifluorescence signal obtained from Nile Red from planes parallel to the oil/water interface was measured by CLSM. The combined thickness of the oil lens and water layer (2.2 mm) is partitioned into approximately 50 slices, corresponding to a slice depth of approximately 50 μm, which therefore

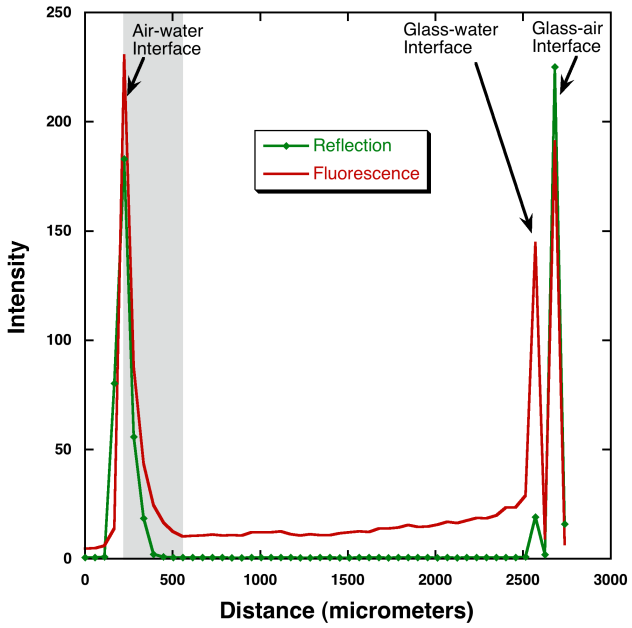

Figure 3.3: Fluorescence signal as a function of distance as obtained at equilibrium from CLSM for a submicellar surfactant solution of $C_{14}E_6$ with a concentration equal to $0.75 \times C_{\mathrm{CMC}}$ and a Nile Red concentration of 0.2 μg/ml. The box shows the region in which out-of-focus reflected and fluorescent light from the air/water interface contributed to the fluorescence signal in the focal planes in the immediate vicinity of the interface.

corresponds to the resolution of the intensity in the direction normal to the interface. The sample was scanned in the planes parallel to the oil/water interface (x-y slices) for slices starting from the air/oil interface and ending at the water/glass surface, and the process repeated. The time to complete one scan from the oil/water to the water/glass interface was approximately 40 sec. After the experiment is complete, the fluorescence intensities at each position along a slice are summed to measure the intensity of each slice, and averaged by the number of voxels in a slice to obtain a value between 0 and 255 (corresponding to the 8 bit analog to digital conversion of the PMT voltage).

3.3 Experimental Results

Reference fluorescence measurements were undertaken to quantify the fluorescence of submicellar solutions in order to determine a threshold value for fluorescence of the dye in the aqueous phase to define the fluorescence of the micelle-free zone. In these experiments the oil lens was not placed on the top of the water layer, and the solution was allowed to come to equilibrium as judged by the fact that the fluorescence did not change with repeated scans. Fig. 3.3 shows (marked as reflection) the integrated intensity at equilibrium of the reflected light from focal planes parallel to the interface as a function of distance for a submicellar solution of $C_{14}E_6$ (C_b=0.75×C_{CMC}) with a concentration of Nile Red equal to 0.2μg/ml. The recorded intensity is dominated by the reflection at the air/water and water/glass and backside glass/air surface (of the chamber glass slide), giving rise to peaks at these interfaces as noted in the figure. These reflections are due to differences in the indices of refraction between the media on either side of the interfaces. In this measurement, the gain of the photomultiplier tube is reduced (relative to the gain used for the fluorescence measurements) because of the large intensity of the reflected signal. Note that the peak corresponding to the interface between the glass bottom of the chamber and the aqueous phase is the smallest because of the close matching of the glass and aqueous phase indices, while the peaks are larger at the air/water and backside glass/air surfaces due to the larger differences in the indices of refraction between air and water and glass and air. These peaks serve to locate the interfaces in the experiments to follow.

The equilibrium Nile Red fluorescence is measured co-currently through a separate optical path to a different PMT with a window of collection (580-750 nm) that does not include the excitation wavelengths, and this is marked in the figure as "fluorescence." The recorded Nile Red fluorescence from each focal plane decays as a function of distance as we move further away from glass-water interface. This attenuation can in principle be due to two factors: As the laser source is below the glass chamber,

light is absorbed by the dye molecules as the laser beam travels through the solution. Thus the available laser intensity decreases in proportion to the extinction coefficient of the dye molecule, which in turn causes a decaying fluorescence signal with distance. However, because the concentration of dye is very low, it can easily be shown from the Beer-Lambert law that this attenuation would be less than one percent. A second reason for the attenuation is the refraction of the excitation laser beam at the bottom of the chamber (the air/glass interface) which defocuses the light and reduces its density. This is the primary reason for the decrease in fluorescence, and while it could be avoided by using an immersion lenses to reduce the refraction, the field of view of the available immersion lenses would not allow for focusing on planes a few millimeters deep into the aqueous phase. Note the strong fluorescence recorded at the air/water, water/glass and backside glass/air surfaces which is co-incident with the reflection peaks. These fluorescence peaks arise from two effects. First, surfactant from solution has adsorbed at the air/water and water/glass interfaces, which drives an adsorption of the Nile Red to the surface to partition into the hydrophobic domains of the adsorbed layers. The Nile Red adsorption gives rise in part to the large fluorescence signals along these interfaces, and is particularly the reason for the fluorescence peak at the water/glass surface being comparable to the fluorescent peak at the air/water surface. At the water/glass surface, the reflection peak is weak relative to the reflection peaks of the air/water and backside glass/air surfaces due to the close matching of the indices of refraction of the glass and water. A second effect, which accounts in particular for the "fluorescent" peak at the backside glass/air surface, is the presence of reflected light from the laser lines in the excitation beam which are included in the collection window. Although the lines selected for excitation (514 and 543 nm) are nominally excluded from the collection window, the acoustic-optical beam splitter does allow some small signal to "bleed" through and although weak can dominate a fluorescence signal at focal planes which are reflective interfaces between

media with large differences in indices of refraction. In the bulk where reflections are minimal this bleed through effect is not noticeable in the recorded fluorescent signal.

The reflection off of the air/water interface from excitation lines which bleed through, and the strong fluorescence of the adsorbed dye at the air/water interface gives rise to an additional effect which is the observed increase in the fluorescence signal in focal planes on the aqueous side of the air/water interface as the interface is approached. These large values are enclosed in the grey box in Fig. 3.3 and arise from the reflected light and high fluorescence from the surface. This shadow region extends approximately 250 μm from the air/water interface into the aqueous phase. In confocal microscopy, light received from a focal plane has contributions from out-of-focus planes in the immediate vicinity of the focal plane. In recording fluorescence emission in the bulk from focal planes, this contribution from the fluorescent light of out-of-focus planes is not significant and a clear resolution is achieved. But in the case of reflected light or fluorescent light from adsorbed layers from an out of focus plane in the immediate vicinity of the focal plane collecting fluorescent light, the large magnitude of these contributions can present a sizable contribution to the light recorded for the focal plane of interest. It is for this reason that a shadow is cast on the water side of the air/water interface. Note because the reflected light is less at the water/glass surface because of the matching of indices of the media, this contribution of out-of-focus light to the fluorescence signal in the immediate vicinity of the interface is not as pronounced and the fluorescence peak is sharper relative to that at the air/water surface.

Plotted in Fig. 3.4 are the reflections and fluorescence signals as a function of distance underneath the air/water interface of micellar solutions with bulk concentrations of $1.5\times C_{\mathrm{CMC}}$ and $2\times C_{\mathrm{CMC}}$ (Fig. 3.4(a) and Fig. 3.4(b) respectively) and a Nile Red concentration equal to that for the submicellar solution of Fig. 3.3. These experiments are undertaken immediately after the submicellar experiments of Fig. 3.3

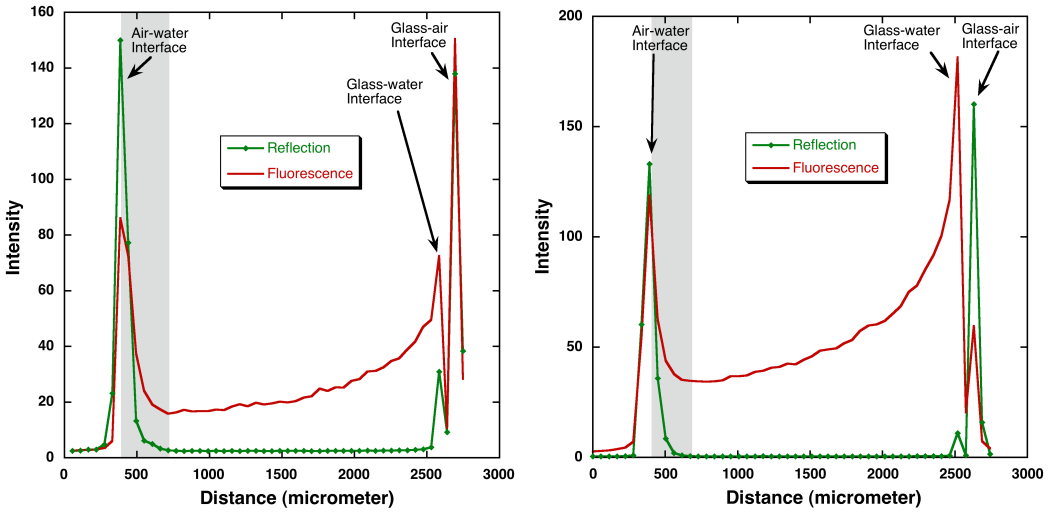

(a) $1.5\times C_{\mathrm{CMC}}$ (b) $2\times C_{\mathrm{CMC}}$

Figure 3.4: Fluorescence signal as a function of distance at equilibrium obtained from CLSM for $C_{14}E_6$ concentration above CMC with Nile Red concentration at 0.2 μg/ml. The box shows the region in which out-of-focus reflected and fluorescent light from the air/water interface contributed to the fluorescence signal in the focal planes in the immediate vicinity of the interface.

at the same laser power settings and PMT gains (as well as all other confocal settings). As expected, the fluorescence is larger from the micellar solutions (compared to the submicellar solution, cf. Fig. 3.3), as the Nile Red molecules partition themselves into the micelles and are surrounded on average by a more hydrophobic environment which does not quench their fluorescence. The exponentially decaying fluorescence signal in the micellar phase is also evident, as are the fluorescent peaks, the coincident reflection peaks and the increase in the fluorescence signal as the air/water interface is approached from the water side (the shadow with a width as shown by the grey box of the same size (250 μm) as the width at the air/water interface of submicellar solutions. The larger recorded fluorescence for the $2\times C_{\mathrm{CMC}}$ solution relative to the $1.5\times C_{\mathrm{CMC}}$ solution for the same concentration of Nile Red can be attributed to the fact that the $2\times C_{\mathrm{CMC}}$ solution with a larger hydrophobic phase will have more dye molecules in a hydrophobic environment and hence a greater fluorescence.

When a fresh lens of hexadecane (containing no surfactant) is placed gently on

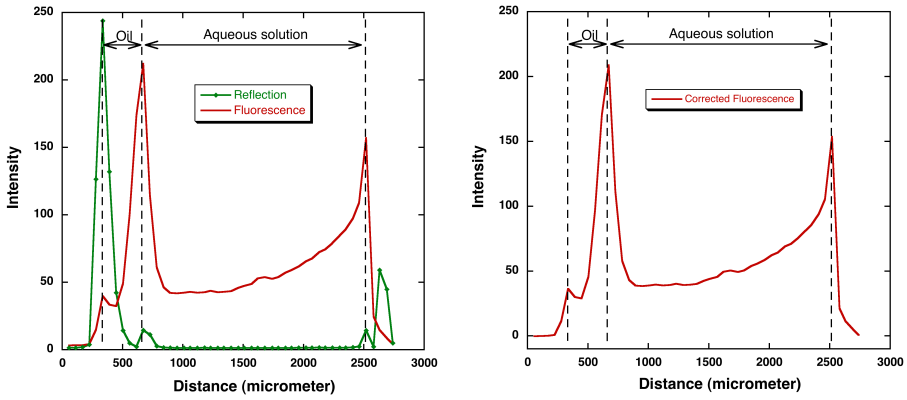

(a) t=18 sec

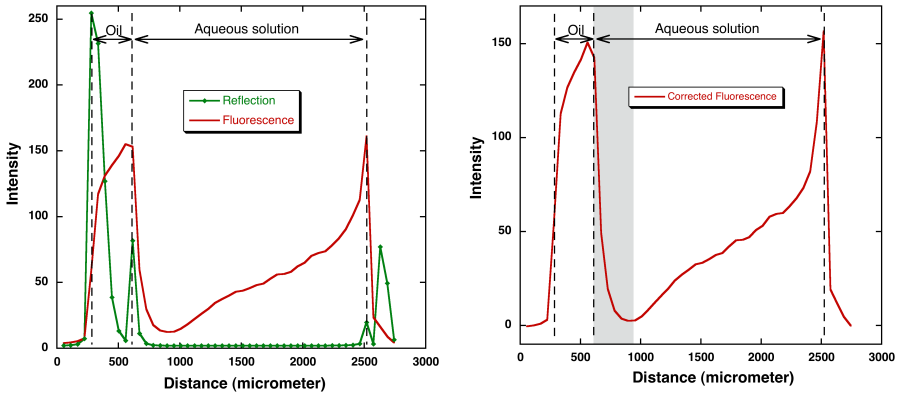

(b) t=320 sec

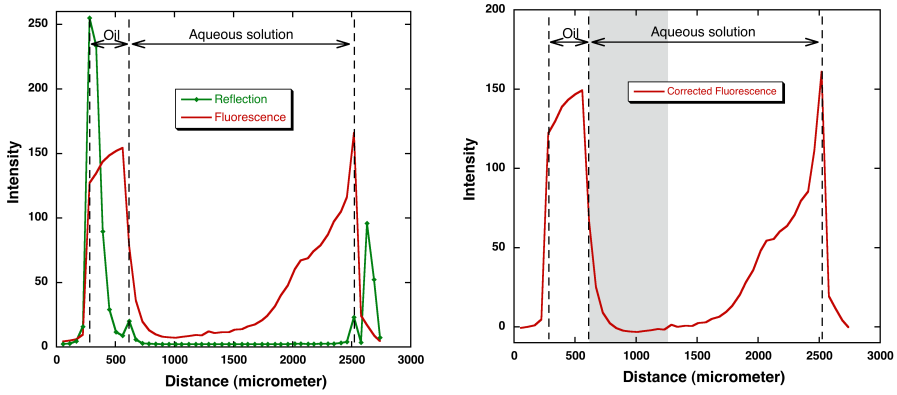

(c) t=1280 sec

Figure 3.5: Visualization of micelle-free zone at different time stages for $2\times C_{\mathrm{CMC}}$ initial concentration. The figures on the left shows raw data obtained from the CLSM, while the figures on the right show the baseline-corrected fluorescence profile obtained after subtracting the reference $0.75\times C_{\mathrm{CMC}}$. Shaded region is the no fluorescence region or micelle-free zone.

the surface of the aqueous phase, equilibrium near the oil-water interface is disturbed as surfactant transports into the oil phase and micelles break down underneath the surface. As a result, a micelle-free zone is developed which is shown in the first set of graphs in Fig. 3.5 at different times through the contrast provided by the fluorescence of the Nile Red initially partitioned into the micelles. This figure reports the results for transport of surfactant from a $2\times C_{\mathrm{CMC}}$ surfactant solution into oil with the dye concentration in the surfactant solution equal to 0.2 μg/ml (as in the reference experiments). First note from this figure that the addition of the oil lens on top of the aqueous phase can be seen in the reflection plots, in which the air/oil interface appears as a strong peak, and the oil/water interface as a much weaker peak, on the same order as the water/glass peak. The oil phase can also be seen in the fluorescence plots. The Nile Red released by the breakdown of the micelles underneath the surface, transfers to the hexadecane phase where it fluoresces strongly due to the hydrophobicity of this phase. This fluorescence in the oil phase is clearly evident in the fluorescence curves of the figure, appearing as a fluorescence signal between the reflection peaks which demarcate the oil phase. Note that the large fluorescent peak at the oil/water interface is due primarily to the adsorption of Nile Red at this surface, as the reflection from this surface is small due to the closer match of the indices of refraction of oil and water (cf. the reduced value of the reflection peak at this interface). As was the case with the air/water interface, the fluorescence intensity increases in the aqueous phase in the immediate vicinity of the oil/aqueous interface due to the contributions of the out-of-focus reflected light and fluorescent light generated at the interface. The shadow region is again approximately 250 μm, as it was for the air/water interface. The intensity of the fluorescence in the oil phase decreases with distance into the oil due to the attenuation of the exciting laser beam and the fact that the concentration of the Nile Red decreases with distance away from the oil/water interface. However, as the air/oil interface is approached from the oil

side, the intensity again increases due principally to the out-of-focus contribution of reflected light since the adsorption of Nile Red at this interface would be small.

In order to correctly identify the micelle-free zone from the plots of the fluorescence as a function of distance in the water phase, the minimal fluorescence of the dye in the aqueous phase (as a function of position) has to be subtracted off in order to set a zero-baseline for demarcating the zone. The reference data obtained previously for the fluorescence as a function of distance from the aqueous/glass interface of the Nile Red from a submicellar solution can be used for this purpose, since the reference fluorescence is collected under the same conditions of confocal setting and aqueous phase thickness as the experiments with the lens of oil over the surface. However, a complication arises due the diffusion of the Nile Red into the oil phase with time. The reference data of Fig. 3.3, obtained without oil above the aqueous phase represents the equilibrium fluorescence for solvated Nile Red in an aqueous solution at a uniform concentration of 0.2 μg/ml. Some dye may have adsorbed onto the air/water and aqueous/glass interface, into the hydrophobic domains of the surfactant layers on these surfaces. In the experiments of Fig. 3.5, the Nile Red concentration in the micelle-free zone can fall below this equilibrium value due to the diffusion of the dye into the oil, and hence subtraction of the reference yields at the least zero and with time negative values for the fluorescence. Thus the micelle-free zone can be identified from the corrected measurement (obtained by the subtraction of the equilibrium reference), by locating the value at which the corrected fluorescence decreases to zero as the oil/water interface is approached from the aqueous side. The second set of graphs in Fig. 3.5 present the corrected fluorescence in the aqueous phase obtained by subtracting the equilibrium of Fig. 3.3, and negative values do become evident at later times near the oil/aqueous interface. In correcting the measurements, the reference data of $0.75\times C_{\mathrm{CMC}}$ was first smoothened by fitting a polynomial before subtracting from the raw data to avoid any irregularities. The reference subtraction

is only done on the aqueous measurements up to the point at which the fluorescence begins to increase due to the out-of-focus contributions of the reflected light and the luminescence of the adsorbed Nile Red. As a result, to track the movement of the boundary between the micelle-free zone and the micelle zone, the boundary must first move out of the shadow of the out-of-focus contributions, in order for a value of zero for the corrected intensity outside of the shadow to be achieved. Thus, in Fig. 3.5(a), the corrected fluorescence profile 18 sec after placing an oil lens on the top of the $2\times C_{\mathrm{CMC}}$ aqueous surfactant solution reveals that the boundary has not emerged from the shadow. But, at 320 sec (Fig. 3.5(b)), we clearly see in the corrected profile the distinction between the fluorescence (micelle zone) and no fluorescence (micelle-free zone) regions as the corrected intensity first becomes equal to zero outside of the shadow region. The boundary is easily located at 330μm from the oil-water interface. At a later time (1280 sec, Fig. 3.5(c)), the boundary has moved more deeply into the aqueous phase and negative corrected fluorescence values are observed just outside of the shadow. The boundary is then located at the point at which the corrected fluorescence changes sign from negative to positive values.

Plotted in Fig. 3.6 is a composite of the spatial profiles of the fluorescence intensity for different times clearly showing the emergence of the micelle-free zone from under the shadow, and its migration into the aqueous phase. Note importantly that the profiles converge as the aqueous/glass interface is approached indicating that in this region the micelle concentration has not dropped significantly, and the dye trapped into the micelles has not been depleted significantly by the extraction into the aqueous phase driven by the diffusion of dye through the micelle-zone and into the oil.

The composite for the spatial profiles of the fluorescence intensity in the oil phase shows that the amount of dye in the oil phase (which is proportional to the area under the profile curves in the oil) increases with time. The transport into the oil phase is marked by a sharp peak near the oil/water interface for early times (up to 230 sec) as

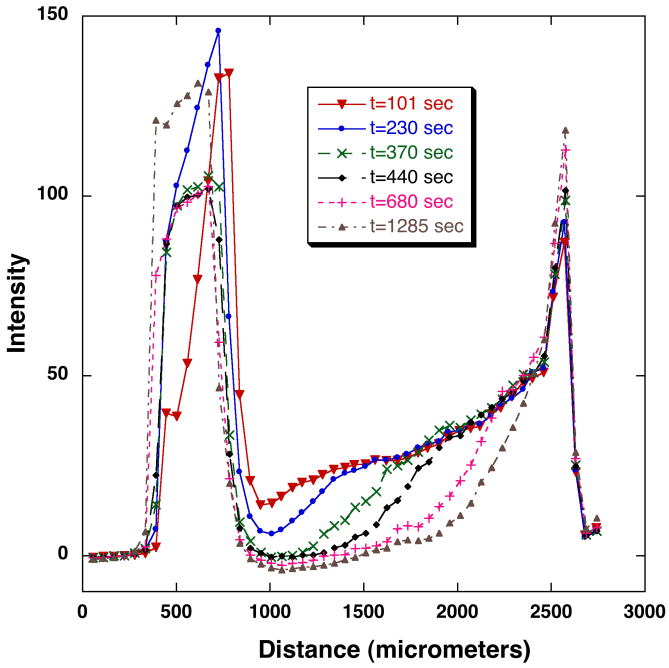

Figure 3.6: Corrected fluorescence intensity plotted against distance obtained from CLSM at different times for an initial bulk concentration of $2\times C_{\mathrm{CMC}}$.

dye first transports into the oil, followed by a reduction in the peak and a flattening out of the profiles for later times as dye diffuses through the oil layer.

From the composite figure a plot can be constructed of the position of the boundary between the micelle and micelle-free zones as a function of time and this is shown in Fig. 3.7(a) for a bulk concentration of $1.5\times C_{\mathrm{CMC}}$ and Fig. 3.7(b) for a bulk concentration of $2\times C_{\mathrm{CMC}}$. Different types of symbols in the graphs represents different sets of experiments conducted at identical conditions and the moving boundary position with time was observed to be consistent and reproducible. Qualitatively it is clear that the boundary initially travels faster but later on slows down as evident from the change in slopes in Fig. 3.7(a) and Fig. 3.7(b). The reasons for the deceleration in the movement of the zone boundary are twofold. First, the oil phase is initially clean and the flux of surfactant through the oil-water interface is very large as oil continuously withdraws surfactant through the oil/water interface. As a result, depletion of surfactant in the aqueous phase takes place at an initially fast rate causing large numbers

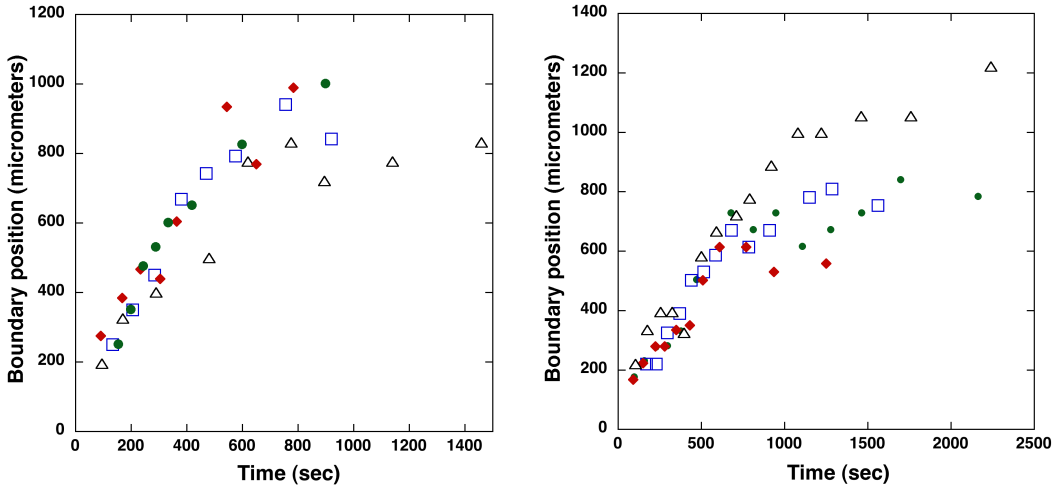

(a) $1.5\times C_{\mathrm{CMC}}$ (b) $2\times C_{\mathrm{CMC}}$

Figure 3.7: Micelle-free zone boundary movement with time as obtained from CLSM experiments for $1.5\times C_{\mathrm{CMC}}$ and $2\times C_{\mathrm{CMC}}$ initial bulk concentration. Each symbol type represents a different experiment.

of micelles to disassemble and the micelle-free zone boundary to move quickly into the aqueous phase. But with time, the oil phase begins to saturate with surfactant, and thus the adsorption flux is reduced, slowing down the depletion of monomer in the micelle-free zone. Secondly, lateral diffusion of micelles into the aqueous region underneath the lens begins to become important for later times, and this replenishes the micelles in the micelle-zone, and reduces the movement of the zone boundary.

3.4 Comparison between Experiments and Theory

The micelle-free zone boundary position as a function of time computed from the solution to the one dimensional model (from Chapter 2) can be compared to the experiments. In undertaking this comparison, note first that the system of the oil lens overlying the water layer has a large area to volume ratio (see Fig. 3.2). The aqueous phase dimensions in the chamber slide are 2.4 cm $\times$ 2 cm $\times$ 0.19 cm, and surfactant molecules from the aqueous phase have a tendency to adsorb onto the plastic side walls, the bottom glass slide as well as onto the air-water interface when the solution

is poured into the chamber. Thus there is always a loss of surfactant molecules from the bulk resulting in a reduced initial bulk phase concentration. To minimize this loss due to adsorption, prior to the deposition of the oil lens, the chamber is rinsed a couple of times with the sample solution so as to saturate the walls and bottom glass slide of the chamber. However, this does not eliminate the loss due to adsorption to the air-water interface when the surfactant solution is poured into the chamber slide. To take into account this loss of surfactant monomers in determining the initial concentration in the aqueous bulk phase, we note that the oil lens is only placed on the air/water surface after a period to allow the monolayer at the air/water interface to come to equilibrium. Thus the surface concentration of the polyethoxylate to be used in correcting for the initial bulk concentration is the equilibrium monolayer concentration Γ^0 at and above the CMC, which has been computed for $C_{14}E_6$ from the fit of the equilibrium tension as a function of concentration using an adsorption isotherm [12]. For the given geometry of the chamber, this correction causes a reduction of $0.13\times C_{\rm CMC}$ concentration from the 1.5 ml of the sample solution. Thus in undertaking the simulations for comparison to the experiments where the nominal initial concentrations are 1.5 and $2\times C_{\rm CMC}$, values of 1.37 and $1.87\times C_{\rm CMC}$ are used.

Fig. 3.8 shows a comparison of the theory using the corrected initial concentrations with the remainder of the parameters as detailed in the simulation chapter with the experiments detailed earlier at the two concentrations. The comparison shows very good agreement between experiments and theory for the first 800 sec of the $1.5\times C_{\rm CMC}$ experiment and 1000 sec for the $2\times C_{\rm CMC}$ experiment (note the zone moves more slowly the higher the initial bulk concentration), and it should be noted that there are no adjustable parameters. From the simulations for the 2CMC it is clear that the agreement extends from the early times where the zone moves quickly and the micelle distribution is sharp and the monomer distribution quasi-static into the middle regime where the zone movement has slowed and the micelle distribution has broadened (Fig.

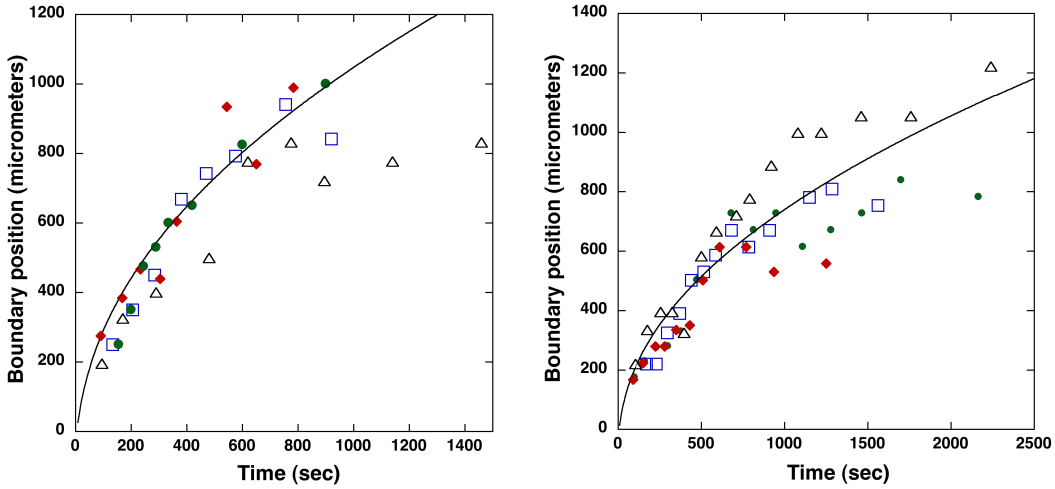

(a) $1.5\times C_{\mathrm{CMC}}$ (b) $2\times C_{\mathrm{CMC}}$

Figure 3.8: Comparison between theory and experiments for the micelle-free zone boundary position vs time. Symbols represent experiments and solid line is theoretical prediction for the corrected concentration.

2.3). For longer times, the movement of the zone becomes noticeably slower than the simulations. We have already speculated that the validity of the one dimensional model used in the simulations begins to break down as diffusion of micelles and monomer parallel to the surface from regions in the aqueous phase not underneath the lens begins to slow the zone movement and accounts for the discrepancy. In addition, as we have also noted, data for longer times (in excess of 2000 sec) is difficult to obtain because the extraction of the dye by the oil removes the dye from the micelles and dims their fluorescence. As a consequence, in particular, the merging of the micelle-free zone with the aqueous/glass solid surface is not imaged.

3.5 Conclusion

The transport of surfactant from a micellar aqueous phase to a clean oil phase has been studied experimentally in the limit where diffusive time scale is arranged to be very large as compared to the micelle dissociation kinetics. In particular, a regime of low micelle concentration is studied where a region depleted of micelles is formed near

the oil/water interface. To verify the existence of these zones, the micelles are labelled with a fluorescent dye (Nile Red) which sequesters into the hydrophobic environment of the aggregates and fluoresces only in this environment and not in the aqueous phase. This fluorescence contrast in the two zones is imaged quantitatively using laser scanning confocal microscopy in which the fluorescence of slices parallel to the oil/water interface are recorded as a function of distance from the interface. Plots of the fluorescence intensity as a function of distance from the interface confirmed the presence of the micelle-free zone, and allowed the boundary between the two zones to be located and its retreat velocity to be measured as a function of time. This position of the boundary between the two zones as a function of time is then compared favorably with the predicted zone boundary movement from the numerical simulations in Chapter 2 without adjustable parameters, providing further support for the two zone transport model.

Appendix A. Determination of Partition Coefficient of $C_{14}E_6$ Between Water and Hexadecane

The nonionic surfactant used, $C_{14}E_6$, is soluble in hexadecane as well as in water, and the partition coefficient drives the diffusion of monomers into the oil phase. The partition coefficient K_p is defined here as the ratio between the concentration of surfactant in the oil phase to the surfactant monomer concentration in the aqueous phase when the two phases are in equilibrium and the aqueous phase is below the CMC.

$$K_p = \frac{C_o}{C_w^m} \tag{A.1}$$

To measure this partition coefficient experimentally, we use a surface tension measurement technique. The pendant bubble technique was used to measure the air/water surface tension of aqueous surfactant solutions equilibrated with oil, for the purposes of measuring the concentration of surfactant in the equilibrated solution. We have used an apparatus similar to the one used by Song [12]. Briefly, a light beam, produced from a tungsten bulb, was collimated by passing through a series of lenses and pinholes. A transparent rectangular quartz cell (2.5(d)×4(w)×4(h) cm; (Rame-Hart, Mountain Lakes, NJ, USA) was filled with the surfactant solutions and placed in the path of the collimated beam with its 4cm×4cm faces perpendicular to the beam. A pendant bubble was formed in the surfactant solution in the cell at the tip of a hollow, inverted, stainless steel needle immersed in the solution. The size of the bubble is approximately 2 mm in diameter and is formed by connecting the inverted needle to a gas tight syringe and moving the plunger of the syringe. The collimated light passing through the cell and across the bubble formed a silhouette image of the pendant shape which was focused by a microscope objective onto a CCD array video camera placed on the side of the quartz cell opposite to the collimating lenses. The images of the bubble were captured electronically. The interfacial loci of the silhouette of the pen-

dant bubble shape were obtained from the captured image by edge detection, and the surface tension was obtained by fitting these loci with solutions of the Young-Laplace equations.

First, known volumes of the aqueous solution of surfactant (with volume V_w and known initial surfactant concentration $C_w^{initial}$) and a pure hexadecane phase (with volume V_o) are equilibrated with each other in a flask, stirring overnight gently enough so as not to form an emulsion but to provide enough convection so that a partition equilibrium is achieved between the two phases. The two layers are then separated and an equilibrium surface tension of the aqueous phase against air is measured with a pendant bubble apparatus by creating an air-bubble in the surfactant solution. Once the surface tension (γ^{eq}) of the equilibrated aqueous phase is measured, the corresponding bulk concentration (C_w^{final}) can be obtained by using a $\gamma^{eq} - C_{bulk}$ curve as a calibration, as reported by Song et al [12]. The measurements reported in [12] are for the surfactant solution prepared from pure water; ideally, we should compare our measured γ^{eq} against a $\gamma^{eq} - C_{bulk}$ curve generated by preparing surfactant solutions with hexadecane equilibrated water. However, our measurements of surface tension for pure water and hexadecane equilibrated water differ by only less than 0.5%. With the known initial and final bulk concentrations in the aqueous phase, one can calculate the partition coefficient as,

$$K_p = \frac{V_w}{V_o}\left(\frac{C_w^{initial}}{C_w^{final}} - 1\right) \tag{A.2}$$

Several measurements of the partition coefficient are undertaken by changing the volumes of the equilibrating phases, and also by changing the initial aqueous phase concentration. The partition coefficient for $C_{14}E_6$-water-hexadecane system is on average 350:1 with a variation of 15% in either direction. Note that, this method of determining the partition coefficient can only work if the final concentration is

below the CMC, as for a bulk concentration above the CMC there is no unique correspondence between γ^{eq} and C_{bulk} as the tension does not change appreciably above the CMC.

Chapter 4

The Microhydrodynamics of wetting on superhydrophobic surfaces

Many naturally existing surfaces have demonstrated extreme water repellency and what has been learnt from the nature that it is a combination of surface microstructures along with low surface energy material causes water to bead up on these surfaces and prevent wetting. In most of these cases, droplet rides over the elevations while trapping air pockets underneath. Although there has been a lot of studies experimentally as well as theoretically for predicting equilibrium or static contact angles, the dynamics of the droplet spreading motion over a textured surfaces is largely unexplored. Aim of this work is to study this dynamics from hydrodynamic point of view and understand, from fluid interactions with topography, what prevents the droplet from spreading further on a textured surface as opposed to that on a flat hydrophobic surface. The chapter is divided as follows, Section 4.1 describes background of superhydrophobicity and the current state of theoretical work. In Section 4.2, we formulate a hydrodynamic model for studying dynamics of the droplet and

its numerical solution approach is detailed in Section 4.3 along with the code validation. Numerical results for a droplet spreading dynamics over a regularly arrayed microstructures in the form of pillars are presented in Section 4.4 and the chapter ends with concluding remarks.

4.1 Theoretical Studies of Superhydrophobicity

The equilibrium contact angle (θ) of a liquid drop at rest on a solid flat homogeneous surface is given by the classical Young's equation:

$$\cos\theta = \frac{\gamma_{SV} - \gamma_{SL}}{\gamma} \tag{4.1}$$

where γ_{SV} is surface energy of the dry solid, γ_{SL} is the surface energy of the wetted solid and γ is the surface tension of the liquid. Although this equation can be viewed as a balance of forces at the contact line, the equation is derived by minimizing the free energy of the drop placed on the solid surface. For a 2-D droplet if we consider the change in the surface energy per unit length for an infinitesimally small displacement δa of the contact line as the droplet spreads on the flat surface, it can be written as,

$$\delta E = \gamma_{SL}.\delta a - \gamma_{SV}.\delta a + \gamma.\delta a.\cos\theta \tag{4.2}$$

First term represents free energy gained due to creating a new solid-liquid interface, second term is for free energy lost by decrease in the solid-vapor interface and last term represents free energy gained due to expansion of the liquid-vapor interface. If we minimize this change in the surface energy we arrive at the Eq. 4.1.

The wetting condition becomes more difficult to describe on a rough solid surface with this equation. Robert Wenzel [55] came up with the first simple model describing the effect of surface roughness on the observed or apparent contact angle θ^*. Consider

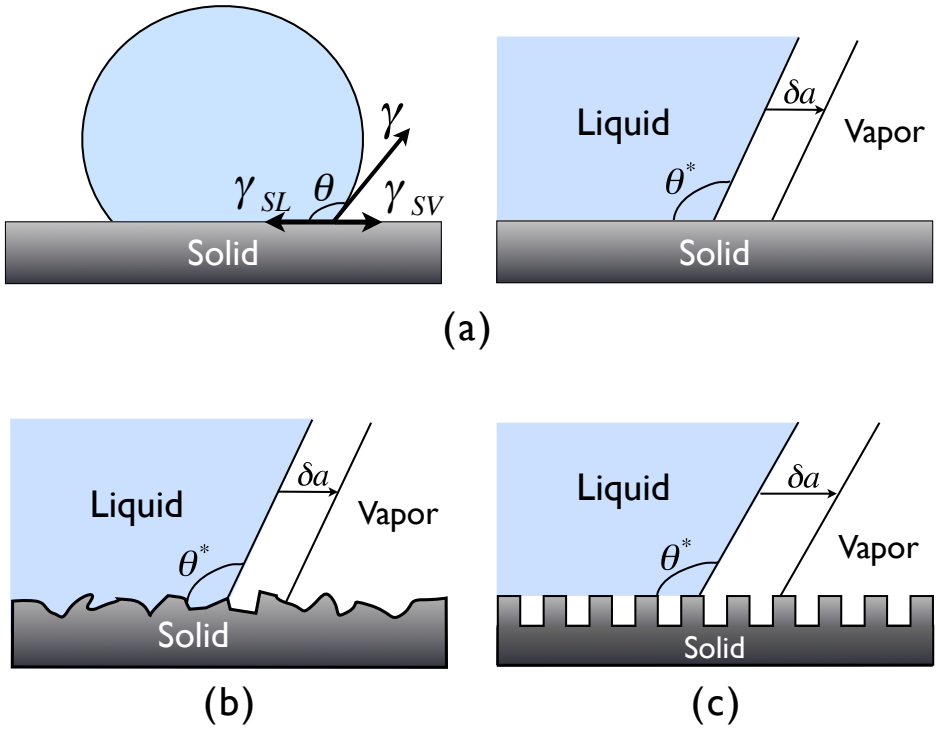

Figure 4.1: Spreading of a droplet with an infinitesimal displacement δa horizontally for; (a) Flat surface, (b) wetted behavior and (c) droplet riding on composite surface of air and solid.

a water droplet on a rough surface spreading with an infinitesimal displacement δa of the contact line parallel to the surface Fig. (4.1b). The change in the surface energy δE per unit length for a displacement δa can then be written in the similar way as,

$$\begin{aligned} \delta E &= r.\gamma_{SL}.\delta a - r.\gamma_{SV}.\delta a + \gamma.\delta a.\cos\theta^* \\ \text{or} \qquad \delta \mathrm{E} &= \gamma^*_{\mathrm{SL}}.\delta \mathrm{a} - \gamma^*_{\mathrm{SV}}.\delta \mathrm{a} + \gamma.\delta \mathrm{a}.\cos\theta^* \end{aligned} \tag{4.3}$$

where r is surface roughness, defined as r = (actual surface area)/(geometric surface area). In other words, droplet can be assumed to be spreading on a flat surface with modified solid-vapor and solid-liquid energies, i.e. $\gamma^*_{SL} = r.\gamma_{SL}$ and $\gamma^*_{SV} = r.\gamma_{SV}$.

Minimizing this energy at equilibrium yields the well-known Wenzels equation,

$$\cos\theta^* = r \cdot \cos\theta = \frac{\gamma^*_{SV} - \gamma^*_{SL}}{\gamma} \tag{4.4}$$

where θ is the contact angle of water as given by Young's equation. As $r \geqslant 1$, Wenzel's equation suggests for Young's angle $\theta < 90^\circ$ wetting gets better (i.e. $\theta^* < \theta$) and for $\theta > 90^\circ$ it gets worse (i.e. $\theta^* > \theta$). This model has an upper limit of validity in r since $|r\cos\theta| < 1$. The Wenzel kind of complete wetting is always associated with a large contact angle hysteresis because of a very low receding angle. As the droplet spreads on the surface, it leaves grooves on the surface filled with liquid and due to pinning of the liquid by itself a very low receding angle can develop.

For a hydrophobic surface ($\theta > 90^\circ$), the surface energy of a dry solid (γ_{SV}) is less than surface energy of a wet solid (γ_{SL}). Hence liquid is less likely to follow the crests and troughs of the rough solid surface, rather it will trap air packets in the groves. Therefore the droplet rests on a composite surface made up of solid and air Fig. (4.1c). Making similar energy arguments for the spreading of a droplet with a small displacement δa over this composite surface, we get

$$\begin{aligned} \delta E &= \phi_s(\gamma_{SL} - \gamma_{SV})\delta a + (1-\phi_s)\gamma\delta a + \gamma.\delta a.\cos\theta^* \\ \text{rearranging,} \quad \delta\mathrm{E} &= [\phi_\mathrm{s}.\gamma_\mathrm{SL} + (1-\phi_\mathrm{s})\gamma].\delta\mathrm{a} - [\phi_\mathrm{s}.\gamma_\mathrm{SV}].\delta\mathrm{a} + \gamma.\delta\mathrm{a}.\cos\theta^* \\ \text{or} \quad \delta\mathrm{E} &= \gamma^*_\mathrm{SL}.\delta\mathrm{a} - \gamma^*_\mathrm{SV}.\delta\mathrm{a} + \gamma.\delta\mathrm{a}.\cos\theta^* \end{aligned} \tag{4.5}$$

Minimizing energy and rearranging we obtain,

$$\cos\theta^* = -1 + \phi_s(\cos\theta + 1) = \frac{\gamma^*_{SV} - \gamma^*_{SL}}{\gamma} \tag{4.6}$$

where ϕ_S is the solid fraction actually in contact with the liquid. This model was first proposed by Cassie and Baxter[56] for porous solids. Again here we can consider that

a droplet is spreading over a composite flat surface of an average or effective surface energy with $\gamma^*_{SL} = [\phi_s.\gamma_{SL} + (1 - \phi_s)\gamma]$ and $\gamma^*_{SV} = [\phi_s.\gamma_{SV}]$. Such a droplet riding on a composite surface of solid and air is known as a "Fakir" droplet. In the limit of $\phi_s = 0$, the apparent contact angle tends to 180°, but this limit is not achievable as in this limit the Fakir state becomes unstable and Wenzel wetting is energetically favored. However for surfaces with a hierarchy of roughness contact angles as large as 170° are achievable[57]. The Fakir regime of wetting is particularly interesting as along with high contact angles it has other desirable properties such as small contact angle hysteresis in spreading, and reduced fluidic drag and slip at the solid surface, owing to the trapped air packets beneath. And thus only Cassie-Baxter regime is termed as "Superhydrophobic".

Although, Wenzel and Cassie-Baxter have provided correlations for understanding the effect of roughness on the wettability more than 60 yeas ago, theories behind superhydrophobicity are still ambiguous. These variational energy arguments are based on the assumption that when the droplet interface moves by an infinitesimal distance δa, it samples several microstructures on the surface so that the droplet (macroscopically) can be considered to be spreading on a flat surface with effective surface properties (modified owing to the presence of the microstructures). In other words, surface features are assumed to be much smaller than the infinitesimally small displacement of the contact line. There is a never ending debate on the validity of Wenzel and Cassie-Baxter relations in the literature [58, 59, 60]. Several researchers have came up with thermodynamic mechanisms for calculating global minimum of the free energy for a droplet on a given surface topography – not considering the effective surface properties. In these procedures, a free energy of a given volume spherical-cap droplet (ignoring gravity) is calculated at different contact angles for corresponding different surface coverage. A global minimum obtained in free energy is then chosen to be the equilibrium contact angle, which was shown in close agreement with the

predicted values from Wenzel and Cassie-Baxter equations [61, 62, 63, 64]. There is also seems to be a lot of interest in studying transitions in between the two wetting regimes (fully wetted regime and Fakir regime) experimentally as well as theoretically [61, 65, 66, 67, 68]. Again free-energy minimization principles are used to describe which wetting state is favorable and phase diagrams are constructed based on the surface roughness or the surface geometric properties.

Although theories based on thermodynamic grounds do bring forward the effect of roughness or geometric properties on the achieved equilibrium contact angle, what they lack is the interaction of the droplet with the topography. In almost every case a droplet is placed onto these surfaces and this droplet when initially contacts the surface has a certain initial shape from where the final equilibrium shape is achieved after going through a dynamic process and most importantly the contact line motion over the topography. While droplet goes through this transient process, it is possible that the droplet come across several available local minima and get trapped into one such minimum. In this case, droplet reaches an equilibrium before the global minimum achieved. Thus, understanding the hydrodynamic behavior of the droplet over surface is critical to provide a complete insight into the problem of topography induced superhydrophobicity.

One common way a droplet is created is by gently placing it on a surface, allowing it to spread and finally come to an equilibrium. Spreading dynamics of a drop can be described by the Navier-Stokes equation, while the contact line motion has to be carefully modeled. Only a few articles have appeared in the literature studying the dynamics. The Lattice-Boltzmann method has been used to model the spreading of droplets on patterned microtextured surfaces for studying the transition between states, modeling the contact angle hysteresis as well as droplet motion over gradient of wettability [68, 69, 70, 71]. In this report we present a continuum approach for modeling spreading dynamics of a droplet over a textured superhydrophobic surface.

In Section 4.2, problem in consideration is formulated. Section 4.3 describes numerical solution to the problem where we demonstrate the use of Biharmonic Boundary Integral Method along with the code validation, followed by numerical results and discussion in section 4.4.

4.2 Model Formulation

4.2.1 Problem Statement

We study the gravity driven spreading motion of a two-dimensional aqueous droplet on a superhydrophobic surface in the inertialess Stokes flow regime. The time evolution of the droplet profile can be obtained by solving the Stokes equations and computing the drop shape quasi-statically. Consider a fluid droplet on a surface with a viscous fluid region (Ω) separated from an inviscid air overlayer by a boundary ($\partial\Omega$). The Stokes equations obeyed by the fluid are,

$$\begin{aligned} \nabla P &= \mu \nabla^2 \mathbf{u} + \rho \mathbf{g} \\ \nabla \cdot \mathbf{u} &= 0 \end{aligned} \tag{4.7}$$

where $\mathbf{u}$(x,y) is the fluid velocity, P(x,y) is the pressure, ρ and μ are the density and the viscosity of the fluid, and $\mathbf{g}$ is the gravitational acceleration. Boundary conditions on the air/fluid interface are normal and tangential stress balances. The inviscid phase is assumed to be passive, hence zero tangential stress is exerted on the droplet surface, and the normal stress exerted by the droplet liquid is balanced by the surface tension (Laplace pressure) and the constant pressure in the inviscid phase.

$$\mathbf{t} \cdot \sigma \cdot \mathbf{n} = 0 \tag{4.8}$$

$$\mathbf{n} \cdot \sigma \cdot \mathbf{n} = -\gamma \, \kappa \tag{4.9}$$

where γ is the surface tension of the liquid and κ is the curvature defined as positive if the center lies within the liquid, $\mathbf{t}$ and $\mathbf{n}$ are counter-clockwise tangential and outward normal unit vectors and σ is the stress tensor

$$\sigma = -P\mathbf{I} + \mu\left(\nabla\mathbf{u} + (\nabla\mathbf{u})^T\right).$$

On the solid wall classical no-slip boundary condition is applied, $\mathbf{u}(x, y) = 0$.

4.2.2 Singularity at the contact point and slip velocity

As the droplet spreads, the contact line has to move or slide along the surface. One common problem associated with the hydrodynamic solution of problems with a contact line movement is the singularity that arises due to the discontinuity in the boundary conditions at the contact point. On the free air/water interface we have a finite velocity but on the solid wall the fluid velocity is zero due to the no-slip condition. This gives rise to an unrealistic infinite force at the contact line [72]. As a consequence, although the solid surface remains at rest, fluid in contact with it has to move violating the no-slip boundary condition. For highly wetting fluids, to eliminate this singularity, a precursor film models have been used widely, where it is assumed that a thin layer of liquid (precursor film) is present ahead of the contact line and the free fluid-fluid interface then merges smoothly with the precursor film at the contact line [73, 74]. For partially wetting fluids, this stress singularity can be avoided by relaxing traditional no-slip boundary condition, i.e. by allowing some finite slip velocity at the contact line or by not-so-realistic approach of setting the contact angle to π (rolling motion instead of sliding) [75]. Slip velocity at the contact line can be imposed in several ways. Navier-type slip model is based on the concept of finite slip-length, b, (distance beyond liquid-solid interface in a direction perpendicular to the wall where velocity approaches zero), where slip velocity at a wall is proportional to

the wall shear stress with proportionality constant as b. Greenspan used Navier-type slip model near the contact line while smoothly reverting to no-slip condition outside the contact line region [76]. More simplified approach is using a numerical slip as demonstrated by Mazouchi et al [77], where slip at the contact point is implemented implicitly by discretizing domain with grid points around the contact point but not including the contact point. The governing equations are then solved with traditional no-slip condition at all grid points along the solid substrate and the position of the new contact line is determined by extending the calculated fluid-fluid interface till the solid surface with independently prescribed contact angle. In this work Mazouchi et al have assumed the prescribed contact angle is constant during the simulations and is equal to the static advancing contact angle, independent of the contact line velocity.

We use a slightly modified slip model than Mazouchi et al, where we compute slip velocity by taking into account dynamic contact angles and contact angle hysteresis. Contact angle hysteresis is a phenomena during which contact line remains fixed at a position (zero slip velocity) for a range of contact angles, $\theta_{rec} \leq \theta \leq \theta_{adv}$, where θ_{rec} and θ_{adv} are the static receding and static advancing contact angles respectively. When there is a relative motion between a contact line and solid surface, the contact angle liquid makes with the solid, θ_{dyn}, is a function of the relative velocity. This contact angle hysteresis and a relationship between dynamic contact angle and slip velocity is shown in Fig. 4.2. Only when the dynamic contact angle θ_{dyn} becomes larger than θ_{adv}, droplet interface slips forward with a velocity $V > 0$ and similar way when $\theta_{dyn} < \theta_{rec}$, the interface recedes, i.e. $V < 0$. There is a body of literature where experimentally measured dynamic contact angles for different slip velocities are fitted to an empirical relation, one such relationship is the Hoffman-Jiang correlation [78]:

$$\frac{\cos\theta_{adv} - \cos\theta_{dyn}}{\cos\theta_{adv} + 1} = \tanh(4.96Ca^{0.702}) \tag{4.10}$$

where Ca is a capillary number, $Ca = \mu V/\gamma$, V is the slip velocity. We use numerical slip model where new contact line position is obtained iteratively till above relation is satisfied for the contact angle and slip velocity.

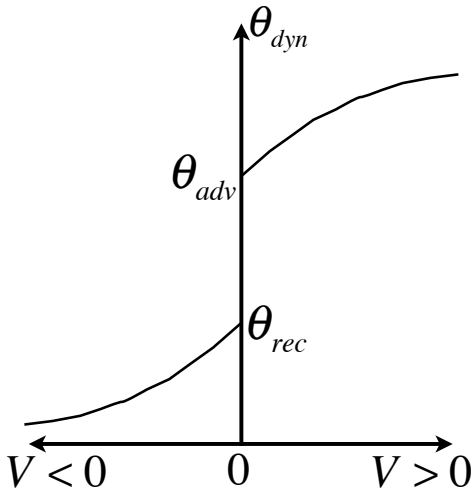

Figure 4.2: Relationship between dynamic contact angle and slip velocity.

4.3 Numerical Solution

4.3.1 Biharmonic Boundary Integral Method

We use the Boundary Integral Method for solving this problem [79][80]. The advantage of using the Boundary Integral Method is that we reduce the dimensionality of the problem by one, by making use of Green's second identity; i.e. transforming the Stokes equations which are valid on the entire fluid domain to integral equations which contain only information from the boundaries. It is convenient to use, as flow variables, the streamfunction Ψ and vorticity ω defined as follows.

$$u_x = \frac{\partial \Psi}{\partial y}, \qquad u_y = -\frac{\partial \Psi}{\partial x}, \tag{4.11}$$

$$\omega = -\nabla \times \mathbf{u} \tag{4.12}$$

Then the Stokes equations in terms of these new flow variables can be written as a biharmonic,

$$\nabla^4 \Psi = 0$$

or in split form,

$$\nabla^2 \Psi = \omega, \qquad \nabla^2 \omega = 0 \tag{4.13}$$

Now applying Green's identity to these biharmonics, the streamfunction and vorticity at any arbitrary point p can be written in terms of information only from the boundary points $q \in \partial\Omega$.

$$\begin{aligned} \eta(p) \cdot \Psi(p) = & \int_{\partial\Omega} \left(\Psi(q) \cdot \frac{\partial G_1}{\partial n} - \frac{\partial \Psi(q)}{\partial n} \cdot G_1 \right) \cdot \partial\widetilde{\Omega}(q) \\ & + \frac{1}{4} \int_{\partial\Omega} \left(\omega(q) \cdot \frac{\partial G_2}{\partial n} - \frac{\partial \omega(q)}{\partial n} \cdot G_2 \right) \cdot \partial\widetilde{\Omega}(q) \end{aligned} \tag{4.14}$$

$$\eta(p) \cdot \omega(p) = \int_{\partial\Omega} \left(\omega(q) \cdot \frac{\partial G_1}{\partial n} - \frac{\partial \omega(q)}{\partial n} \cdot G_1 \right) \cdot \partial\widetilde{\Omega}(q) \tag{4.15}$$

where $\widetilde{\Omega}(q)$ is a differential increment along the boundary at q, $\eta(p)$ and is given by

$$\begin{aligned} \eta(p) &= 0, \quad \text{if } p \notin \Omega + \partial\Omega, \\ &= \varphi, \quad \text{if } p \in \partial\Omega, \\ &= 2\pi, \ \text{if } p \in \Omega. \end{aligned} \tag{4.16}$$

and where, φ is the angle between the two tangents on either side of the point p. G_1 and G_2 are the fundamental solutions of

$$\nabla^2 G_1 = \delta\left(|p-q|\right), \qquad \text{and} \qquad \nabla^4 G_2 = \delta\left(|p-q|\right)$$

which gives,

$$G_1 = \log|p-q|\,, \qquad \text{and} \qquad G_2 = |p-q|^2\,(\log|p-q|-1) \tag{4.17}$$

We have four variables ψ, ω and their normal derivatives involved in the governing equations (4.14) and (4.15). Thus we have to write boundary conditions in terms of these four variables. Rigorous manipulation starting from Eq. (4.8) yields the tangential stress balance as

$$-\omega + 2\frac{\partial^2\Psi}{\partial s^2} + 2\kappa\frac{\partial\Psi}{\partial n} = 0 \tag{4.18}$$

and eliminating the pressure term from equations (4.7) and (4.9) we get the normal stress balance condition as,

$$\frac{\partial\omega}{\partial n} + 2\frac{\partial^2}{\partial s^2}\left(\frac{\partial\Psi}{\partial n}\right) - 2\frac{\partial}{\partial s}\left(\kappa\frac{\partial\Psi}{\partial s}\right) = -\frac{\gamma}{\mu}\frac{\partial\kappa}{\partial s} - \frac{\rho}{\mu}gt_y, \tag{4.19}$$

where s is the arc-length. The no-slip condition at the solid surface can be written as $\Psi = 0$ and $\frac{\partial\Psi}{\partial n} = 0$. These boundary conditions and the two biharmonic boundary integral equations are need to be solved simultaneously to obtain Ψ and ω for the boundary points.

4.3.2 Implementation of Boundary Integral Method

As an analytical solution of this problem is not feasible, a numerical approach has to be adopted. We approximate the drop boundary by a polygon with N linear segments such that flow variables have constant values over each segment. As mentioned earlier, we employ a modified numerical slip model to solve this problem. In this model we do not evaluate flow variables exactly at the contact-line but at the midpoints of each segments as shown in the Fig. (4.3), where q_j's are the vertices of

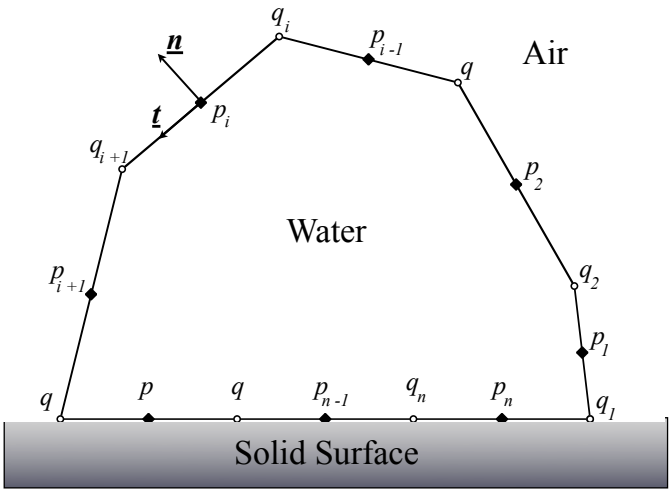

Figure 4.3: Schematic of approximating droplet with a polygon.

the polygon and midpoints p_i's are the collocation points or nodes, where we evaluate the flow variables. Hence, we apply the stress balance conditions on every node at the air/water interface and the no-slip condition is applied to the nodes which are on the solid-surface. By avoiding solving equations at the contact-point we naturally avoid the singularity.

The governing equations in discrete form can be written as,

$$\eta_i \Psi_i = \sum_{j=1}^{N} \left(\Psi_j \int\limits_{\partial\Omega_j} \frac{\partial G_1}{\partial n} \partial\widetilde{\Omega} - \frac{\partial \Psi_j}{\partial n} \int\limits_{\partial\Omega_j} G_1 \partial\widetilde{\Omega} + \frac{1}{4}\omega_j \int\limits_{\partial\Omega_j} \frac{\partial G_2}{\partial n} \partial\widetilde{\Omega} - \frac{1}{4}\frac{\partial \omega_j}{\partial n} \int\limits_{\partial\Omega_j} G_2 \partial\widetilde{\Omega} \right) \tag{4.20}$$

$$\eta_i \omega_i = \sum_{j=1}^{N} \left(\omega_j \int\limits_{\partial\Omega_j} \frac{\partial G_1}{\partial n} \partial\widetilde{\Omega} - \frac{\partial \omega_j}{\partial n} \int\limits_{\partial\Omega_j} G_1 \partial\widetilde{\Omega} \right) \tag{4.21}$$

which can be written in matrix form as

$$\mathbf{A}\Psi + \mathbf{B}\frac{\partial \Psi}{\partial n} + \mathbf{C}\omega + \mathbf{D}\frac{\partial \omega}{\partial n} = 0 \tag{4.22}$$

$$\mathbf{A}\omega + \mathbf{B}\frac{\partial \omega}{\partial n} = 0 \tag{4.23}$$

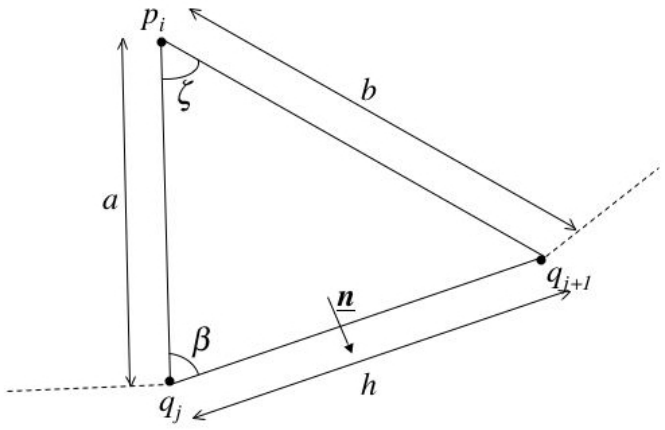

Figure 4.4: Triangle geometry for evaluating integrals in eqns. (4.24)–(4.27).

where,

$$A_{ij} = \int\limits_{q\in\partial\Omega_j} \frac{\partial}{\partial n}\log|p_i-q|\,\partial\widetilde{\Omega}(q) - \eta_i\delta_{ij}, \tag{4.24}$$

$$B_{ij} = -\int\limits_{q\in\partial\Omega_j} \log|p_i-q|\,\partial\widetilde{\Omega}(q), \tag{4.25}$$

$$C_{ij} = \frac{1}{4}\int\limits_{q\in\partial\Omega_j} \frac{\partial}{\partial n}\left[|p_i-q|^2\left(\log|p_i-q|-1\right)\right]\partial\widetilde{\Omega}(q), \tag{4.26}$$

$$D_{ij} = -\frac{1}{4}\int\limits_{q\in\partial\Omega_j} |p_i-q|^2\left(\log|p_i-q|-1\right)\partial\widetilde{\Omega}(q). \tag{4.27}$$

Taking advantage of the polygonal geometry, we evaluate these integrals analytically following Kelmanson's approach[81]. Consider a triangle formed by node p_i and end-points q_j and q_{j+1} of any boundary $\partial\Omega_j$, as shown in the Fig. (4.4) where,

$$\begin{gathered} a = |p_i-q_j|\,, \quad b = |p_i-q_{j+1}|\,, \quad h = |q_j-q_{j+1}|\,, \\ \beta = \angle p_iq_jq_{j+1}, \quad \text{and} \quad \zeta = \angle q_jp_iq_{j+1}. \end{gathered} \tag{4.28}$$

Using these notations, we can evaluate integrals in Eqs. (4.24)–(4.27) exactly as,

$$\int\limits_{q\in\partial\Omega_j} \frac{\partial}{\partial n}\log|p_i-q|\,\partial\widetilde{\Omega}(q)=\zeta, \tag{4.29}$$

$$\int\limits_{q\in\partial\Omega_j} \log|p_i-q|\,\partial\widetilde{\Omega}(q)=a(\log a-\log b)\cos\beta+h\log b-h+a\zeta\sin\beta\equiv I, \text{say}, \tag{4.30}$$

$$\int\limits_{q\in\partial\Omega_j} \frac{\partial}{\partial n}\left[|p_i-q|^2\left(\log|p_i-q|-1\right)\right]\partial\widetilde{\Omega}(q)=a(2I-h)\sin\beta, \tag{4.31}$$

$$\begin{aligned}\int\limits_{q\in\partial\Omega_j} \left[|p_i-q|^2\left(\log|p_i-q|-1\right)\right]\partial\widetilde{\Omega}(q)&=(a\sin\beta)^2\left\{I-\frac{2}{3}h-\frac{1}{3}a\zeta\sin\beta\right\}\\ &+\frac{1}{3}\left\{(h-a\cos\beta)^3\left(\log b-\frac{4}{3}\right)+(a\cos\beta)^3\left(\log a-\frac{4}{3}\right)\right\}.\end{aligned} \tag{4.32}$$

Also we discretize the tangential and normal stress balances, Eqs (4.18) and (4.19), along the arc-length. The calculations of the curvature, and the central difference scheme used for discretization are described in Appendices. Making use of the symmetry of the problem, we solve for only half of the droplet ($x>0$). On the axis of symmetry we provide boundary conditions as $\psi=0$ and $\omega=0$. Then for a given initial shape we solve the following matrix system of $4N$ unknowns and $4N$ equations to obtain the flow variables.

$$\begin{pmatrix}\mathbf{A}&\mathbf{B}&\mathbf{C}&\mathbf{D}\\ \mathbf{0}&\mathbf{0}&\mathbf{A}&\mathbf{B}\\ \mathbf{R}&\mathbf{S}&\mathbf{T}&\mathbf{0}\\ \mathbf{U}&\mathbf{V}&\mathbf{0}&\mathbf{W}\end{pmatrix}\cdot\begin{pmatrix}\Psi\\ \partial\Psi/\partial n\\ \omega\\ \partial\omega/\partial n\end{pmatrix}=\begin{pmatrix}\mathbf{0}\\ \mathbf{0}\\ \mathbf{0}\\ \mathbf{b}\end{pmatrix} \tag{4.33}$$

A, B, C and D are dense matrices and R, U, V are tri-diagonal and S, T and W are diagonal matrices at the free surface. At the solid wall, $R_{ij}=V_{ij}=\delta_{ij}$ and $S_{ij}=T_{ij}=U_{ij}=W_{ij}=0$. The matrix system is then solved with LU decomposition to

obtain the streamfunction and its normal derivative at each boundary node, which is used to compute the velocities. Instantaneous velocities obtained are then used for generation of a new droplet profile by marching in time with the help of the kinematic condition,

$$x(t + \Delta t) = x(t) + u_x \, \Delta t, \qquad \text{and} \qquad y(t + \Delta t) = y(t) + u_y \, \Delta t, \tag{4.34}$$

where, u_x and u_y are the components of velocity $\mathbf{u}$ in x and y direction. To get a position of the new contact line, the calculated new interface is made to intersect the solid surface at a position where dynamic contact angle-velocity correlation (Eq. 4.10) is satisfied.

During the time evolution of the droplet, boundary nodes may get convected along the surface and thus distribution of the nodes is no longer uniform. To avoid crowding/piling of nodes in some region as opposed to other, a cubic spline is fitted after every time iteration to the advanced droplet profile and boundary nodes are again redistributed. Also, often a high curvature region is obtained near the contact line during the spreading process, especially during the droplet spreading over a topography due to very large contact angles. In such cases, the air/fluid interface is smoothed out by fitting a cubic polynomial for the first few nodes from the contact line.

To summarize, a FORTRAN code is developed, which uses only an initial shape of a droplet. From this initial shape, using Boundary Integral Method, it computes matrix elements of Eq. 4.33. Matrix system is solved with LU decomposition to obtain flow variables. Using flow variables boundary nodes are advanced in time to get the new droplet profile. Contact point is moved with a slip velocity, dependent upon the dynamic contact angle. Boundary nodes are re-meshed and the process is repeated to obtain the time evolution.

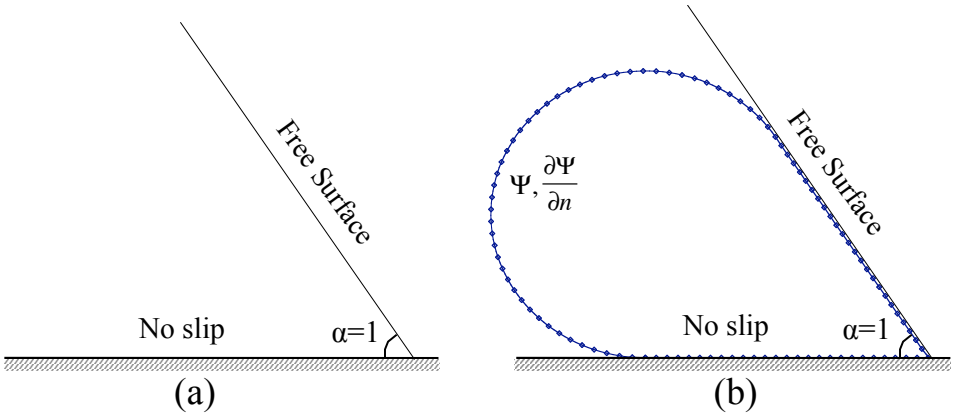

Figure 4.5: (a) Schematic of flow in a corner between a free and a no-slip surface. (b) Numerical grid employed to solve this problem using the Boundary Integral Method

4.3.3 Code Validation

The developed fortran code is validated by comparing calculated instantaneous flow variables with those obtained from an exact analytical solution of a simpler problem. Eq. (4.13), i.e. $\nabla^4\psi = 0$, has a separable solution in polar co-ordinates [82][83],

$$\psi(r,\theta) = r^{\lambda+1} f_\lambda(\theta), \tag{4.35}$$

where, λ is any constant (real or imaginary) and the general form of $f_\lambda(\theta)$ is given by,

$$f_\lambda(\theta) = A_1 \cos\left[(\lambda+1)\theta\right] + A_2 \sin\left[(\lambda+1)\theta\right] + A_3 \cos\left[(\lambda-1)\theta\right] + A_4 \sin\left[(\lambda-1)\theta\right], \tag{4.36}$$

A_1, A_2, A_3, and A_4 are constants to be evaluated from boundary conditions. We consider a problem of flow in a corner, formed by a no-slip surface and a free surface (Fig. 4.5), for which an analytical solution can be obtained[83]. Normal and tangential stresses are applied on the free boundary and a no-slip condition at the solid

surface, which are written as,

$$\begin{aligned} \text{No} - \text{slip} \quad &: \quad f(0) = f'(0) = 0, \\ \text{Tangential Stress Balance} \ &: \quad f''(\alpha) - f(\alpha)(\lambda^2 - 1) = 0, \\ \text{Normal Stress Balancce} \quad &: \quad f'''(\alpha) + (3\lambda^2 + 1)f'(\alpha) = 0. \end{aligned} \tag{4.37}$$

$\lambda(\alpha)$ can be obtained from the normal stress balance condition. We use $\alpha = 1$, for which $\lambda = 0.814$. Now we have three boundary conditions and four unknown constants. Thus, we arbitrarily fix A_1 and evaluate the other constants as,

$$\begin{gathered} A_2 = \frac{A_1}{\lambda + 1} \frac{(\lambda + 1)\cos\left[(\lambda + 1)\alpha\right] - (\lambda - 1)\cos\left[(\lambda - 1)\alpha\right]}{\sin\left[(\lambda - 1)\alpha\right] - \sin\left[(\lambda + 1)\alpha\right]}, \\ A_3 = -A_1, \quad \text{and} \quad A_4 = -\frac{(\lambda + 1)}{(\lambda - 1)} A_2. \end{gathered} \tag{4.38}$$

For solving this problem numerically using the boundary integral method, we have to have a closed calculation domain which is achieved by joining the two surfaces smoothly with a circular arc. As boundary conditions on the curved surface, we use the actual ψ and $\frac{\partial \Psi}{\partial n}$ from the known theoretical solution. The matrix system in Eq. 4.33 is then solved with appropriate boundary conditions to obtain ψ, ω and their normal derivatives. Fig. 4.6 compares the flow variables obtained from the code with analytical values, and a very good agreement between the two is observed. The singularity at the apex (in between 26^{th} and 27^{th} node) has been handled well by the numerical method.

4.4 Numerical Results and Discussion

The first step in understanding the dynamics of the spreading of a droplet over a surface with topology is to study the equilibrium shapes of the drops after they have come to rest. These equilibrium shapes represent the final resting states of

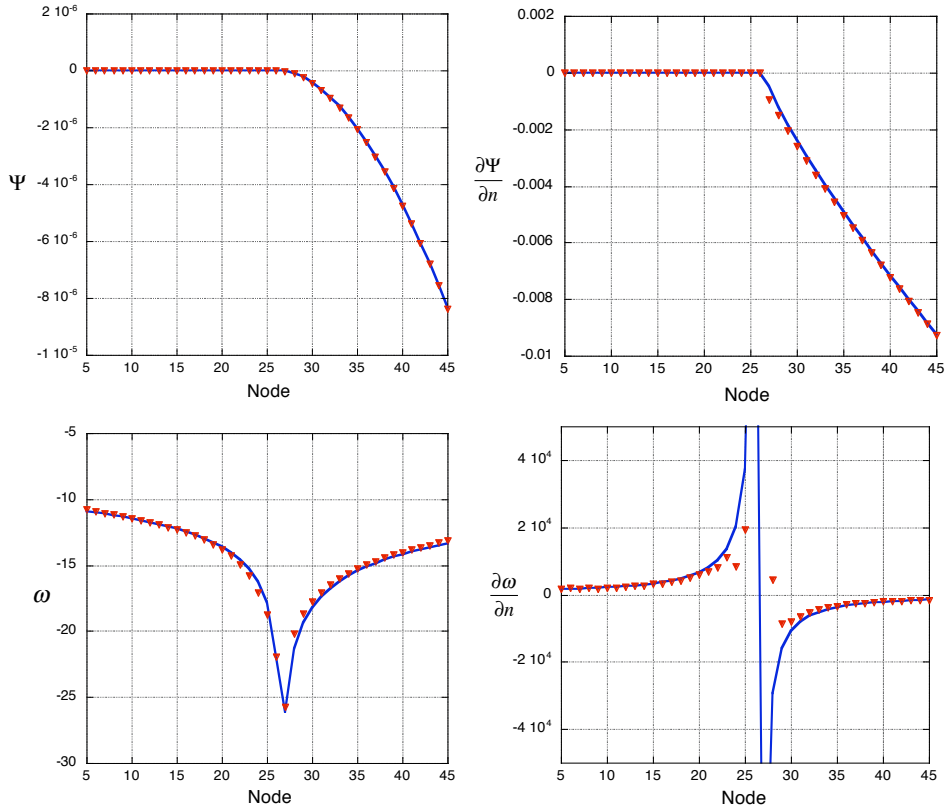

Figure 4.6: Comparison of numerical results (symbols) with analytical solution (solid line) for flow in a corner problem.

the trajectory of drops advancing over a surface. As such, in what will become clear further on, these shapes are important in constructing a correlation between the initial shape and location of a drop placed on a surface with topology, and its final position on that surface. The static equilibrium shapes are discussed in Section 4.4.1. Once we know all the possible equilibrium shapes for a droplet of a given volume, from integration of Young-Laplace equation, we consider the dynamics of the spreading motion over surfaces and we expect that the equilibrium shape obtained at the end of the dynamic process should correspond to one of the equilibrium shape predicted by the above procedure. Numerical results for the spreading dynamics are obtained from the Boundary Integral Method. In all simulations presented in further sections, we use the representative case of a 2 mm in radius (circular) water droplet. The initial shape

of the droplet is assumed to be section of a circle with radius a, and the droplet is symmetric about Y-axis. Time evolution is obtained by solving the Stokes equations by using the Boundary Integral Method. Equations are non-dimensionalized with initial drop radius, a, and the characteristic time and velocity are given by;

$$\tau' = \frac{\mu}{\rho g a}, \qquad V' = \frac{\rho g a^2}{\mu}. \tag{4.39}$$

Thus, by writing the governing equations and boundary conditions in dimensionless form, the only parameter which remains is the Bond number, $Bo = \rho g a^2/\gamma$, which is a ratio of the body forces to the surface tension forces. For a water droplet of radius $a = 2mm$, density $\rho = 1000kg/m^3$ and with gravitational acceleration $g = 9.81m/s^2$, the Bond number is $Bo = 0.545$ and this value is used in the simulations. First, we will describe the numerical results on a planar hydrophobic surface (without topography, Section 4.4.2), to provide base cases to compare with spreading over a surface which has topology. We then describe the spreading dynamics of a droplet over a superhydrophobic surface consisting of regular patterns of rectangular elevations separated by rectangular valleys (Section 4.4.3).

4.4.1 Static equilibrium shapes

Consider a 2-dimensional droplet of liquid with surface tension γ and density ρ resting on a surface in a gravitational field of g. The forces acting on the droplet are the gravitational or body force, and an interfacial or capillary force due to the surface tension of the liquid. On a planar surface, which is perpendicular to gravity, and of infinite extent, the equilibrium shape of the droplet on the surface is uniquely defined if two parameters are specified: volume of the droplet and a contact angle it makes with a surface. These are the familiar "sessile" forms. Thus for a given volume and contact angle, the droplet interface has a unique shape as described by

the Young-Laplace equation,

$$\Delta P = \gamma\kappa = \frac{\gamma}{R} \tag{4.40}$$

where ΔP is the pressure difference across the interface, which is balanced by the surface tension times the curvature κ of the interface, where R is the radius of curvature. This Young-Laplace equation can be integrated to obtain the interfacial shape at the equilibrium. Details of the procedure are provided in the Appendix C.

For a planar surface, for a given volume V, by changing the contact angle we can obtain different equilibrium shapes, which intersect the solid surface at different X positions. From this exercise, we can obtain the extent of spreading on a flat surface, presumed to be infinite in extent, as shown in Fig. 4.7 for two different volumes (V1 and V2, V2>V1), where equilibrium contact angles are plotted against equilibrium X positions for contact angles (as measured through the liquid phase) up to 180°. Figure 4.7 shows that on a flat surface, as expected, a droplet which makes a larger contact angle on a flat surface spreads to a lesser extent as compared to a droplet which makes a smaller contact angle. The reason for this is the larger static contact angle generates very large curvatures and capillary pressures at the air/water interface near the contact line, which can support the weight of the droplet and restrict its spreading extent. Also, as shown in the figure, for the same contact angle a droplet with a larger volume spreads to greater extent as the curvature forces are not sufficient to support the larger weight of the droplet. Fig. 4.7 also presents the equilibrium shapes obtained by integrating the Young-Laplace equation for different equilibrium contact angles, namely 100°, 150° for the volume V1. It is clear from the interfacial loci depicted in the figure that the larger the contact angle the smaller the radius of curvature at the apex of the sessile drop.

In the context of the study of the droplet spreading dynamics on surfaces with topography, the final resting shapes of drops placed on the surface contact the surface on sharp 90° edges or corners where they become pinned. These final states represent

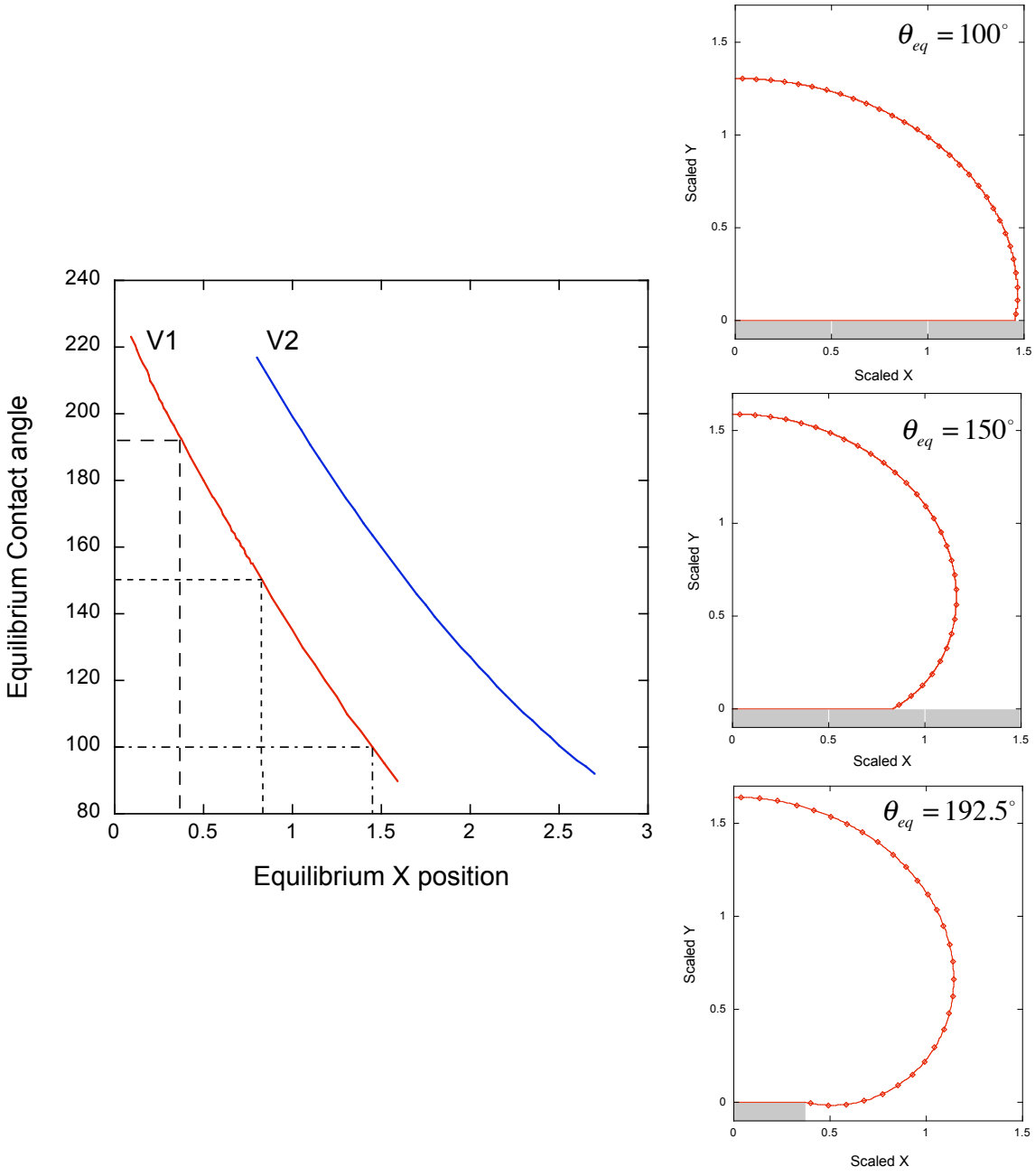

Figure 4.7: Graph on the left shows extent of spreading on a flat surface obtained from integration of the Young-Laplace equation for two different volumes V2>V1, V1=12.46 mm^2 and V2=28.11 mm^2. Plots on the right shows different equilibrium shapes obtained for same volume V1 at different equilibrium contact angles on a flat surface (shaded in grey). These three equilibrium points are also marked on the extent of spreading curve for volume V1. Equilibrium angles larger than 180° are obtained if droplet is pinned indefinitely at a corner point. Droplets are symmetrical about Y axis.

sessile drops on finite planar surfaces in which the droplet hangs freely over the edge of the surface. They can be computed by integrating the Young-Laplace equation through the point at which the tangent to the surface becomes parallel to gravity and the shape becomes multi-valued in the coordinate x. For a fixed volume of droplet V, as the equlibrium X (edge or corner) position of these hanging shapes decreases from the X position of the droplet (with volume V) with a contact angle of 180°, the hanging contact angle increases above 180° as shown in Figure 4.7. The shape for a hanging contact angle equal to 192.5° is shown, and the radius of curvature at the apex is larger than that of the droplet which intersects the surface at 180°.

4.4.2 Spreading dynamics over a planar surface

Here we present numerical results for a droplet spreading on a planar surface, i.e. without topography. As mentioned before, a singularity is associated with the three-phase contact line sliding over the surface. The first case we consider here is when the prescribed contact angle that the liquid makes with the solid is equal to π or 180°. In this case the droplet rolls over the surface (tank-treading motion) as opposed to sliding and thus the contact line singularity is absent. Fig. 4.8(a) shows the time evolution of a droplet. Initially, the shape of a droplet is prescribed to be a perfect circle (of radius $a = 2$mm) just touching the flat solid surface only at a point. For a water droplet of radius $a = 2mm$, density $\rho = 1000kg/m^3$ and with gravitational acceleration $g = 9.81m/s^2$, the Bond number is $Bo = 0.545$ and this value is used in the simulations. The initial shape of the droplet is approximated by a polygon of $N = 280$ sides. The matrix system generated by boundary integral code (1120×1120) is solved in a loop to obtain the time evolution of the droplet. The contact line is advanced by making the air/water interface to intersect the solid surface at the constant contact angle of 180°, which achieved by fitting a parabola through the last three points. As a function of time, under the action of gravity the droplet spreads

on the flat surface with tank-treading motion until the equilibrium is reached, where gravitational forces are balanced by the curvature and surface tension as shown in the Fig.4.8(a). At this equilibrium shape, Young-Laplace equation is satisfied at every

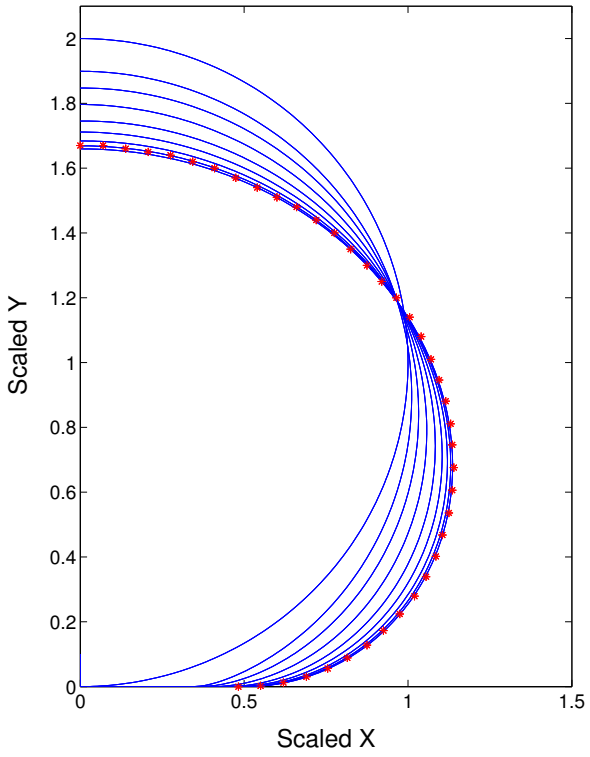

(a) Droplet shape evolution with time, solid lines represents numerical simulations at dimensionless time, τ = 0, 0.05, 0.15, 0.3, 0.5, 0.75, 1.05, 1.4, 1.8, and symbols represents equilibrium shape obtained from integration of Young-Laplace equation. Excellent agreement between the two equilibrium shape is observed.

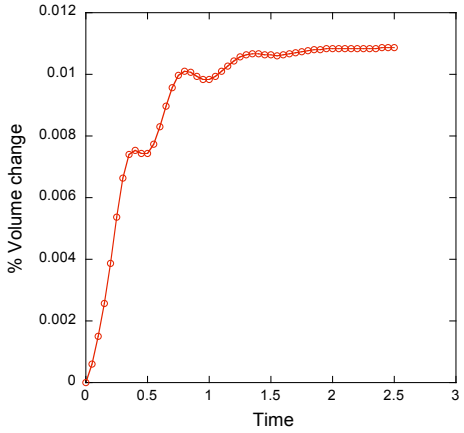

(b) Droplet volume change during the spreading dynamic simulations.

Figure 4.8: Droplet spreading over a flat surface with constant contact angle of 180°. Droplet rolls as opposed to sliding.

point on the boundary, i.e. pressure drop across the interface is equal to the surface tension times the curvature. This predicted Young-Laplace equilibrium shape is also plotted in the Fig.4.8(a), and excellent agreement between the two equilibrium shapes is obtained. This agreement validates our time dependent code. As a check on the incompressibility, the volume change during the spreading process is also plotted in

Fig.4.8(b) and a negligible volume change is observed (about 0.01%).

However, as mentioned before, on a flat surface a water droplet cannot achieve a contact angle larger than 120°. Thus, this tank-treading motion is not possible for such a low contact angles and the droplet rather slides or slips on the flat surface. Fig.4.9 shows spreading dynamics of a droplet with specified static advancing contact angle of 120°. The drop initial shape prescribed to be a section of circle with initial contact angle of 160°. To provide slip at the contact line Hoffman-Jiang correlation (Eq. 4.10) is used, which is solved iteratively during each time-step. Again the final equilibrium shape obtained by the simulations matches very well with the predicted Young-Laplace shape; in particular the final position of the contact line is predicted from Figure 4.7.

4.4.3 Spreading dynamics over topography

Modeling the Hydrodynamic Movement of a Contact Line Over a Surface Topography of Pillars

For studying the spreading dynamics of a droplet over a topography, we need to consider the interaction of the fluid flow with the surface microstructures from a hydrodynamic point of view. The droplet interface interacts with the surface through the contact angle hysteresis, and velocity dependent dynamic contact angles. Fig. 4.10 demonstrates pictorially these interactions with different surfaces. Consider first a flat surface, Fig. 4.10(a). It is well known that in order for the liquid to spread on the flat surface, the liquid-air interface has to exceed a minimum critical contact angle, which is the static advancing contact angle (θ_{adv}) measured through the liquid till the solid surface. This θ_{adv} is an intrinsic property of the liquid-solid system in consideration and is independent of the orientation of the flat surface. That is, if the liquid is spreading downwards on a vertical surface, Fig. 4.10(b), the minimum critical contact angle required for the on-set of the downward spreading motion is

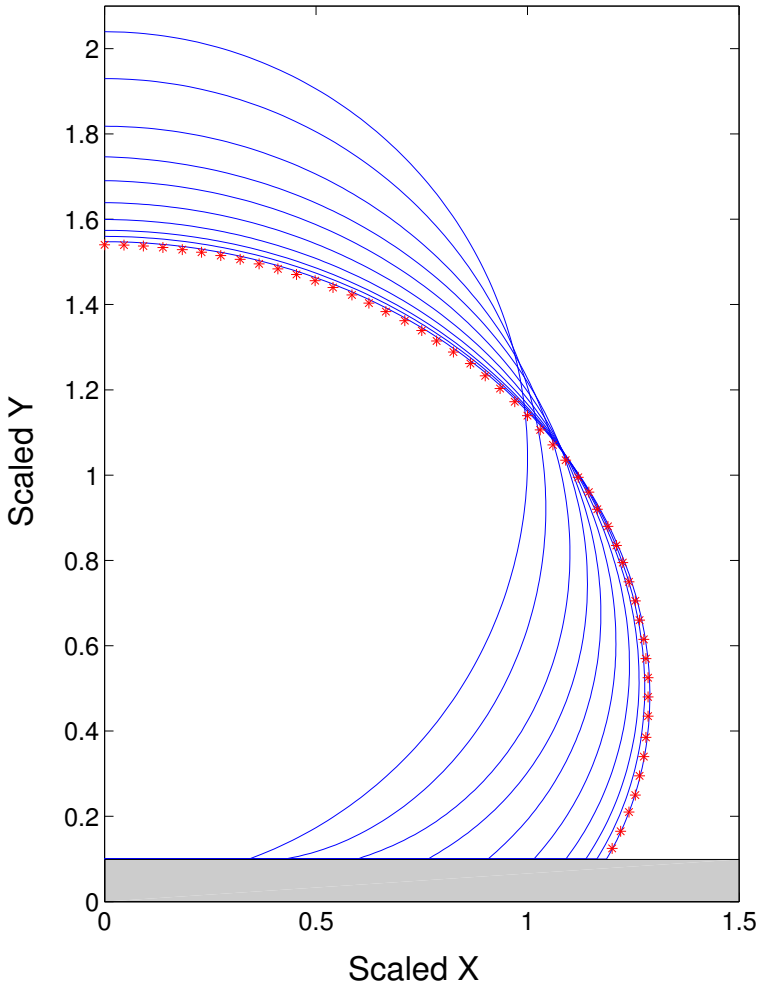

Figure 4.9: Droplet spreading over a flat surface (shaded in gray) with static advancing contact angle of 120°. Numerical results are shown with solid line at dimensionless time τ = 0, 0.21, 0.67, 1.49, 2.8, 4.8, 7.73, 11.87, 1757, and 30. Symbols represents equilibrium shape obtained from integration of Young-Laplace equation. Excellent agreement between the two equilibrium shape is observed.

still θ_{adv} but measured with respect to the vertical wall. To extend this concept of the static advancing contact angle to the surface with a topography in the form of pillars, consider a case in Fig. 4.10(c) where liquid spreads on the top horizontal surface of a pillar with minimum critical advancing angle of $\theta_{crit,H}(= \theta_{adv})$. But when droplet reaches the sharp corner point of this pillar, the contact line can slip

vertically downwards only if it exceeds $\theta_{crit,V}$ ($=\theta_{adv} + 90°$) measured with respect to the horizontal surface. Thus, for all dynamic contact angles in the range $\theta_{crit,H} \leq \theta_{dyn} \leq \theta_{crit,V}$ the contact line does not move, when at the corner, even though interface makes contact angle larger than θ_{adv} with the horizontal plane. In other words, these sharp corner points act as pinning points – they pin the contact line at the corner – and offers multiple static contact angles. The rest of the droplet, however, is free to move, and if the droplet can come to an equilibrium shape with a contact angle within the above mentioned limits then further droplet spreading motion is arrested. On the other hand, if such an equilibrium shape does not exist for a given volume of the drop at a given pinning position, then dynamic contact angle exceeds $\theta_{crit,V}$ and the contact line begins its motion again. In this process, the free interface of the droplet bends so much that it is possible for the interface to touch the neighboring post/pillar and then that touching point becomes the new contact line. The droplet then spreads further on the top horizontal surface of the next pillar.

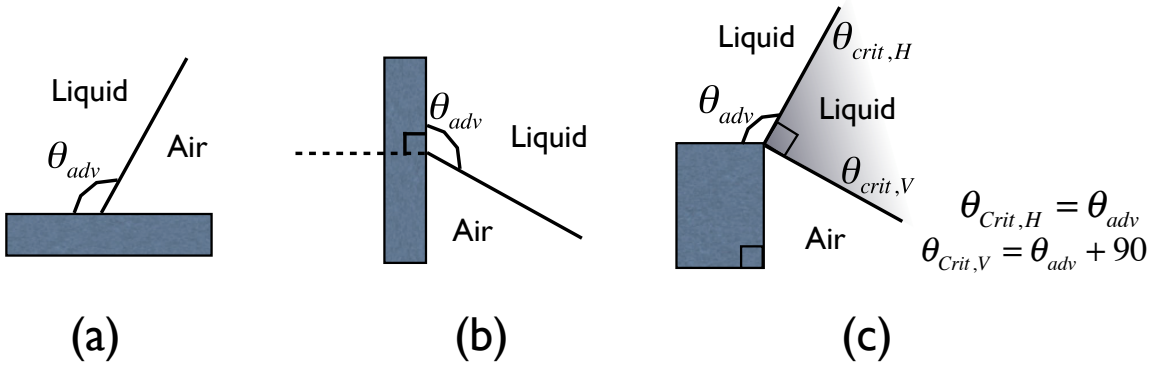

Figure 4.10: Minimum critical contact angles for the on-set of droplet contact line motion: (a) forward on a horizontal surface, (b) downward on a vertical surface, and (c) horizontal till the corner and downward after pinning at the corner for contact angles in the range $\theta_{crit,H} \leq \theta_{dyn} \leq \theta_{crit,V}$

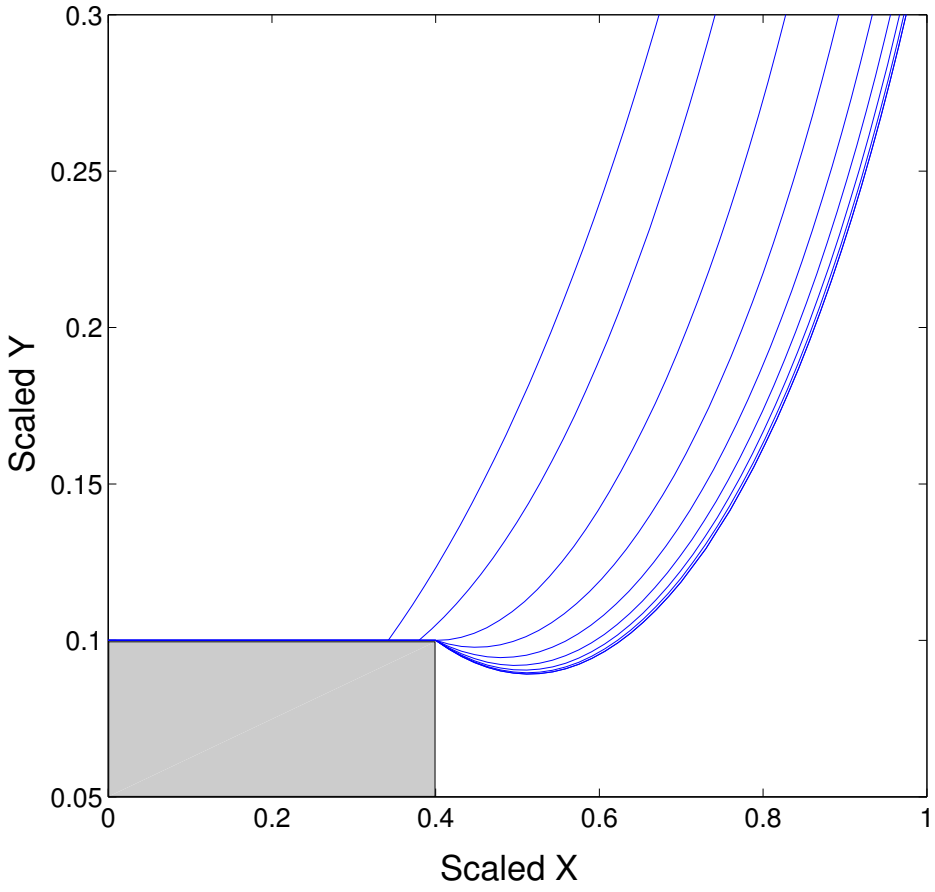

Figure 4.11: Droplet initially spreads over a flat surface (shaded in gray) with static advancing contact angle of 120° and suddenly gets pinned at a corner point located at $X = 0.4$. Numerical results are shown at dimensionless time $\tau = 0$, 0.1, 0.3, 0.6, 1, 1.5, 2.1, 2.8, 10.25 and 28.25. Apparent equilibrium contact angle observed was $\theta^*_{eq} = 189.98°$, which can be located on extent of spreading curve (Fig. 4.7) for volume V1 at pinning position of $X = 0.4$

The Indefinite Pinning of an Advancing Droplet At a Corner

As an illustration of the pinning of the droplet contact line at a corner, we choose the same initial shape for the droplet, a section of a circle with a contact angle of 160 ° and a volume V=V1 (from Figure 4.7) =12.46 mm^2, and an advancing contact angle (120°) as the previous simulation on a flat surface (Figure 4.9). However, an edge is located at a distance of $X = 0.4$ from the centerline of the drop. We

choose this value for the edge location because it is clear from Figure 4.7 that for this volume a hanging drop pinned at $X = 0.4$ can exist at equilibrium with a hanging angle of approximately 190°. Importantly this angle is smaller than the angle ($\theta_{crit,V} = \theta_{adv} + 90 = 210°$) required for the drop to slide down the vertical surface. Hence we anticipate the drop to move first, and subsequently get pinned at the corner until equilibrium. Incorporating the interaction between the topography and the fluid flow over a textured surface as described above, Fig. 4.11 shows the numerical results for a droplet spreading on a flat surface up to the distance of $X = 0.4$ where it encounters the corner or pinning point. As the simulation begins, the droplet initially spreads on the flat surface as the dynamic contact angle is larger than θ_{adv}. At time $\tau = 0.1455$ the contact line reaches the corner point (at $X = 0.4$) and the contact line gets pinned indefinitely at this point. But as the rest of the droplet shape is still not an equilibrium shape, the interfacial nodes continue to move. The interface bends over while remaining pinned at the corner point until finally an equilibrium configuration is reached where all the forces are balanced. The final equilibrium shape is realized at the corner point with the equilibrium contact angle of about 189.98° in agreement with Fig. 4.11. This very large contact angle is possible because it still lies in the range of $\theta_{crit,H} \leq \theta_{eq} \leq \theta_{crit,V}$. The contact line position and the contact angle as a function of time indicate that the contact line slips untill it reaches the corner point, where it sticks until equilibrium. Similarly, the contact angle increases monotonically when the contact line is pinned at the corner and reaches an equilibrium value of 189.98°.

The Spreading Dynamics of Droplets Over Consecutive Pillars

With reference to the previous simulation of movement over an isolated pillar and pinning at the downstream edge, advancement over a microtextured surface of pillars involves the fundamental steps of movement over the horizontal surface of the pillar

to the corner edge to form a hanging drop, followed by attachment of part of the meniscus to the next pillar. For this attachment to occur, the next pillar must be close enough (that is the gap small enough) so that the hanging drop – as it evolves over the edge – contacts the next pillar with its hanging interface before coming to an equilibrium or, if it cannot reach equilibrium, develop a contact angle with respect to the vertical larger than the advancing angle so it moves down the vertical wall of the pillar. (In the latter case, attachment can still occur as the movement down the vertical wall allows the meniscus to come in contact with the next pillar.) Fig. 4.12(a) shows droplet spreading motion over a surface composed of a topography in the form of a width of the pillar = 0.05 and gap = 0.1. Initial shape is similar as before but the prescribed advancing contact angle is 100°. Droplet spreads initially on the flat surface till the corner at $X = 0.4$ and contact line remains pinned while the interface bends over. And before it can come to an equilibrium, contact line touches the neighboring pillar at $X = 0.5$ and begins its spreading motion till it is pinned at the next pinning corner at $X = 0.55$ and finally comes to an equilibrium as all the external forces and the contact angle boundary conditions are satisfied. We see distinct slip-stick-jump motion of the contact line over the topography while trapping an air underneath the droplet. Slipping over the horizontal surface, sticking to the corner point and jumping from one pillar to the next. Fig. 4.12(b) shows this motion when we plot the contact line X position as a function of a time and contact angle also varies accordingly. Thus, just by prescribing an intrinsic angle of only 100° and having a topography on the surface, we see that the final equilibrium angle reached by the droplet is very large (about 174.3°). This large equilibrium angle is possible because the multiple contact angles offered by the sharp pinning point. Final equilibrium position of the contact line and the contact angle can be located on the extent of spreading curve generated before.

Note that in these simulations, after droplet contact line jumps to the next pillar,

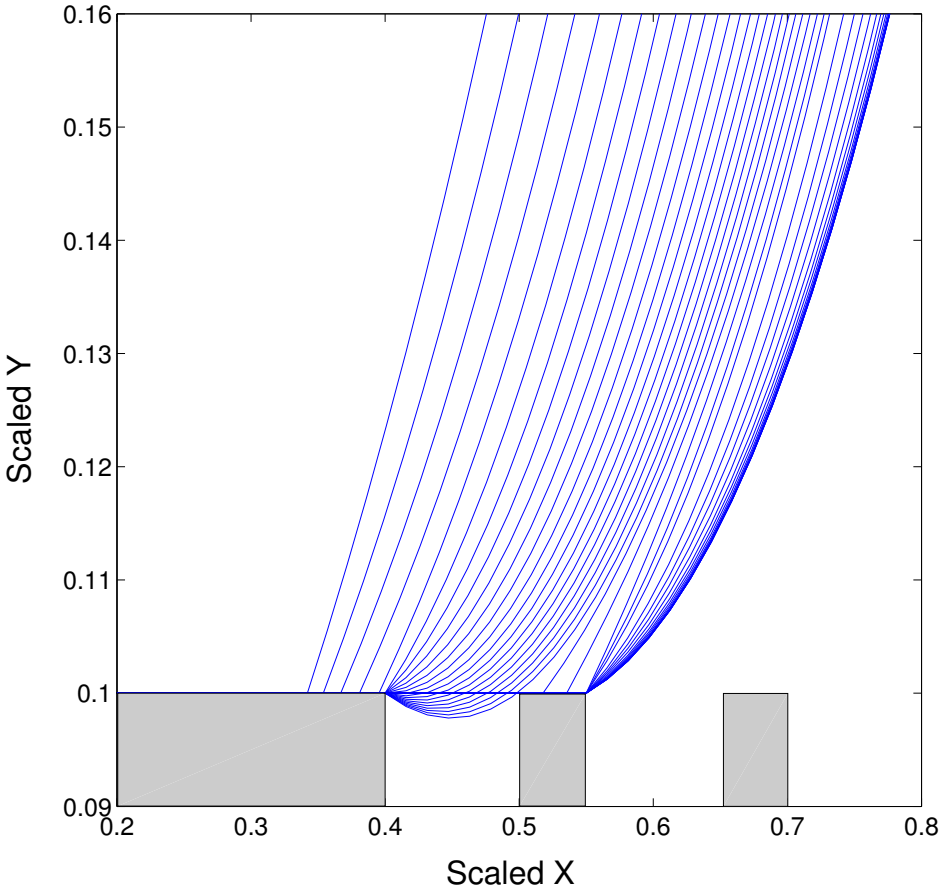

(a) Time evolution of the droplet shape near the contact line region. Droplet achieves a final equilibrium shape at the pinning point located at $X = 0.55$.

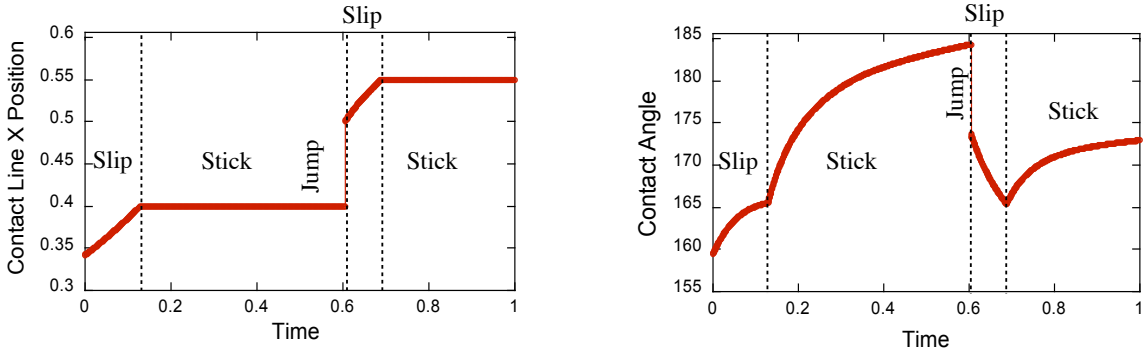

(b) Left hand side plot shows slip-stick-jump motion of the contact line, contact line slips on the horizontal surface, sticks after reaching the corner point and jumps from one pillar to the next. Corresponding dynamic contact angles are plotted on the right.

Figure 4.12: Droplet spreading dynamics over a topography composed of solid width = 0.05 and gap = 0.1 for advancing contact angle of 100°.

liquid-air meniscus in between the two pillar is considered to be flat. That is, although zero tangential stress condition is applied on the free air-water interface riding over trapped air pocket, normal-stress balance is not solved for. Instead, $\psi = 0$ is specified on the flat interface. This simplification is valid, as long as the radius of curvature of the free interface is much larger than the distance between the two pillars, which is usually the case. We have also investigated the spreading dynamics while considering the curvature of the interface, and found that the curvature is indeed small and the final equilibrium shape and overall dynamics of the droplet is not affected. Spreading dynamics of the droplet is dominated by the contact line motion and free interface above the solid but it is unaffected by solid topography or shape of the liquid menisci in the interior of the droplet. Some of the numerical results capturing dynamics of the liquid meniscus can be found in Appendix D at the end of the chapter.

For the topography considered in our simulation, if we compute the average solid area fraction (ϕ_s) available for a droplet to spread on a composite surface made of pillar width = 0.05 and gap = 0.1, we get $\phi_s = 0.333$ and corresponding predicted contact angle by Cassie-Baxter relation (Eq. 4.6) is 136.43°. There is clearly a mismatch between the two equilibrium contact angle on a similar surface topography. But the equilibrium shape we obtained by our simulation is a perfectly valid shape for a given volume and it falls exactly on the straight line predicted by integrating Young-Laplace equation (Fig. 4.7). That is, in the equilibrium shape obtained in our simulation the pressure difference across the interface is exactly equal to the curvature times the surface tension at every single point on the interface. Reason behind this discrepancy is that the relations based on variational energy principles consider the surface is composed of micro-structures so small that surface is assumed to have some average properties, i.e. effective solid-vapor surface energy (γ^*_{SV}) and effective solid-liquid surface tension (γ^*_{SL}), as mentioned before. And droplet is assumed to be spreading over a macroscopically flat, but with an average lower energy surface. This

variational energy approach clearly does not account for interaction of the flow with the topography. This interaction, as described earlier, can result in any equilibrium contact angle if $\theta_{crit,H} \leq \theta^*_{eq} \leq \theta_{crit,V}$ inequality is satisfied. And final equilibrium contact angle achieved depends on the history of the droplet.

In simulation presented in Fig. 4.12(a) droplet never feels the presence of the second pillar situated at $X = 0.65$. However, if we push the droplet down forcefully – on the same textured surface as above – it sees or explores the pillars located at farther distances. For example, in Fig 4.13(a), Fig 4.13(b), Fig 4.13(c) and Fig. 4.13(d) where droplet initial shape itself has a contact line already located on more distant pillars. In such cases droplet still spreads ahead as the contact angle it makes with the horizontal surface is larger than $\theta_{adv} = 100^\circ$ and comes to an equilibrium at the next available pinning point. Thus, depending upon where the final pinning point is located, the apparent equilibrium contact angle varies. Figures show that for pinning points located at $X = 0.7$, $X = 0.85$, $X = 1.0$ and $X = 1.15$, apparent equilibrium contact angles obtained on the exactly same textured surface, for the same volume droplet, are 161.98°, 148.29°, 135.23° and 122.57° respectively. And all these equilibrium shapes fall on the extent of spreading curve, as shown in Fig. 4.14. Fig. 4.14 also plots the Cassie-Baxter equation predicted angle on the curve and we see that contact angles larger or smaller than Cassie-Baxter prediction are possible, provided they are within the range $\theta_{crit,H} \leq \theta^*_{eq} \leq \theta_{crit,V}$ and we have pinning points at respective locations. In other words, for a textured surface, there is no one single apparent equilibrium contact angle (like obtained from global energy minimization or Cassie-Baxter relation) that describes the surface fully.

In above simulations, droplet contact line never starts its downward motion once it is pinned. In order to see this penetrating motion, contact angle has to exceed the critical angle of $\theta_{crit,V}$. To demonstrate this behavior we consider a case where intrinsic advancing contact angle is 90°. Therefore, when contact angle exceeds 180°,

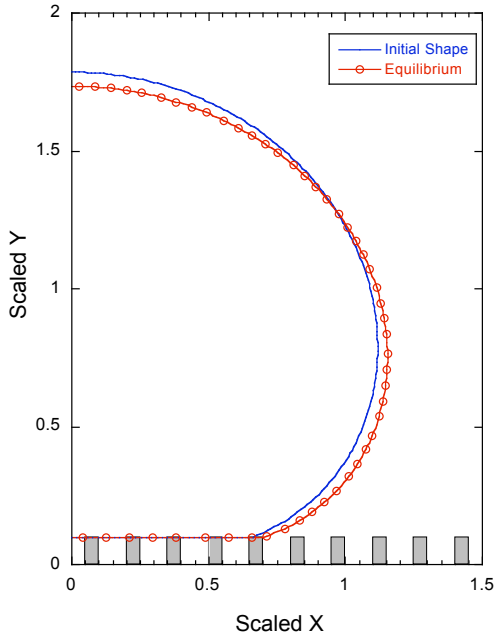

(a) Droplet pins at $X = 0.7$ $\theta^*_{eq} = 161.98°$

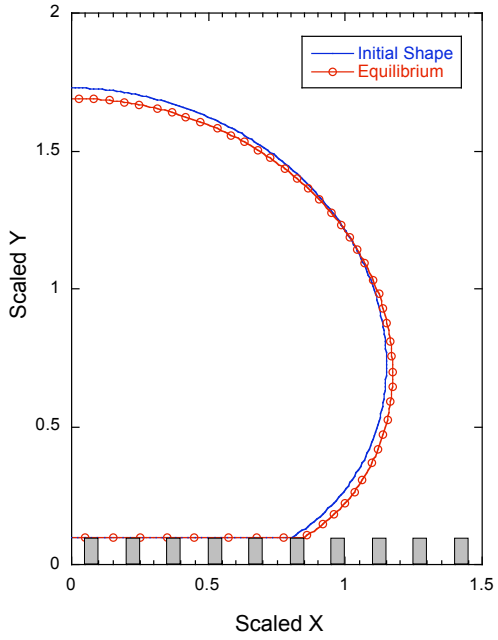

(b) Droplet pins at $X = 0.85$ $\theta^*_{eq} = 148.29°$

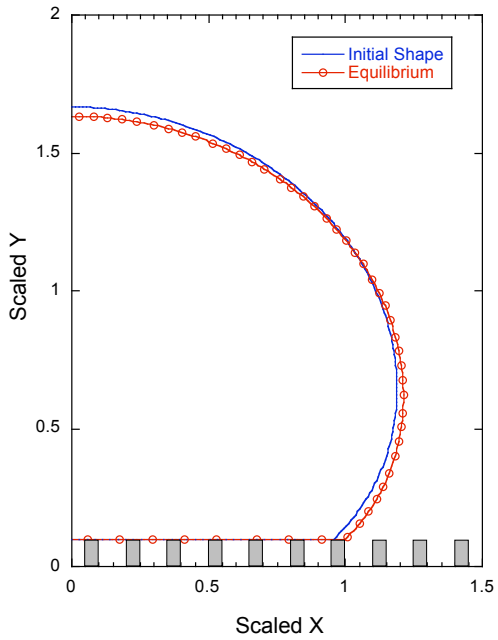

(c) Droplet pins at $X = 1.0$ $\theta^*_{eq} = 135.23°$

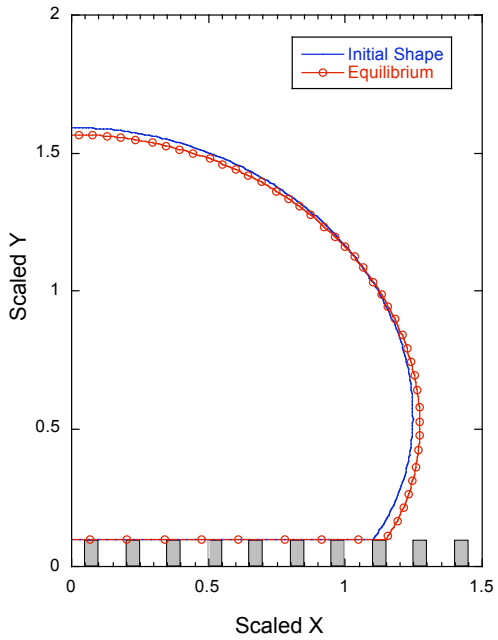

(d) Droplet pins at $X = 1.15$ $\theta^*_{eq} = 122.57°$

Figure 4.13: Droplet spreading on a topography of pillar width = 0.05 and gap = 0.1 with different initial shape, shows different apparent equilibrium contact angels.

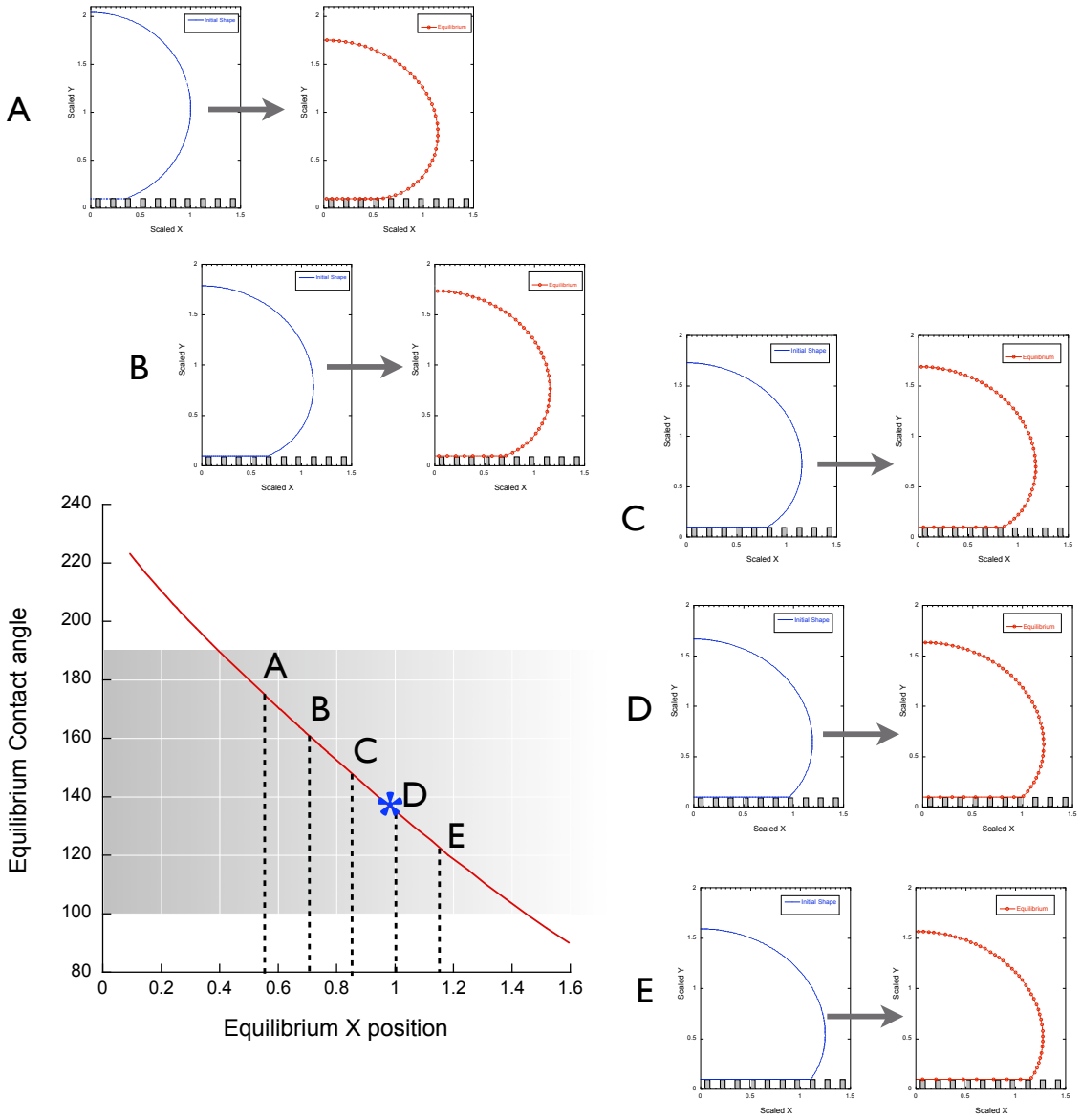

Figure 4.14: Extent of spreading curve for volume V1, on which different equilibrium points are plotted for a given surface texture obtained from the dynamics of the spreading problem with different initial shapes. Shaded area shows the range of contact angles possible ($\theta_{crit,H} \leq \theta^*_{eq} \leq \theta_{crit,V}$) for the prescribed intrinsic surface energy of the liquid-solid system θ_{adv}. $'*'$ is the Cassie-Baxter relation predicted apparent contact angle.

contact line will resume its downward motion and equilibrium angles larger than 180° cannot be realized as in the case of Fig. 4.11. Fig.4.15 and Fig 4.16 shows slip-stick-penetration-jump behavior for two different pillar densities, where contact line after sticking penetrates down the pillar before the interface touches the next surface. Extent of downward penetration is not significant but can be seen in the simulations. And again, final equilibrium position and the contact angle can be located on the extent of spreading curve.

4.5 Conclusion

From our numerical simulations, what we see is the superhydrophobicity is attributed to the nature of the pinning points and the final equilibrium contact angle is dependent upon where the pinning points are located. Closer the distance of the final pinning point to the axis of symmetry, for a given volume, larger is the observed equilibrium contact angle. Once the droplet attains equilibrium at a corner, it doesn't know the presence of the pinning points which are ahead of the contact line. In our simulations, we also observe very large equilibrium contact angles, much larger than those predicted by Cassie-Baxter equation for similar surface features. Major difference between the two is that Cassie-Baxter equation is dependent upon effective surface properties while our hydrodynamic model is based on the interaction of fluid droplet contact line with local topography of the surface. On the textured surface there are number of equilibrium shapes of the droplet are possible at different pinning locations with corresponding contact angles. Final equilibrium shape attained by the droplet is based on the history of the droplet, i.e. how droplet achieved that equilibrium. When droplet spreads on the surface with a very small initial base radius, it first sees pinning points that are close to the symmetry axis and hence final equilibrium contact angle obtained is larger. If for some reason (often in experiments due to inertia

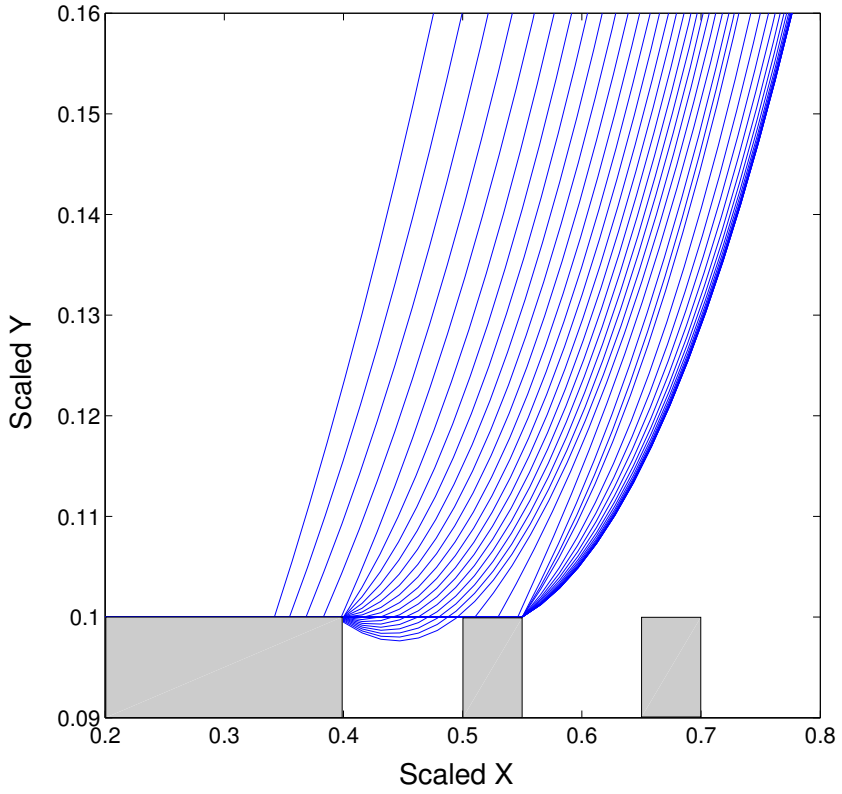

(a) Time evolution of the droplet shape near the contact line region. Droplet achieves a final equilibrium shape at the pinning point located at $X = 0.55$.

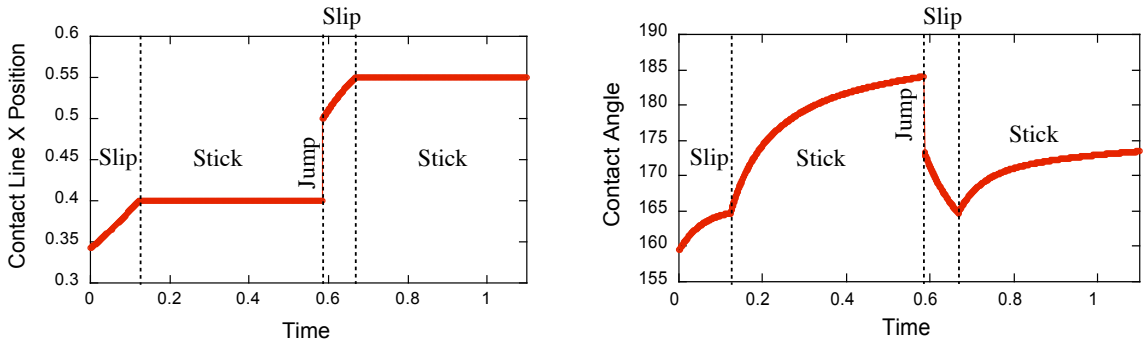

(b) Left hand side plot shows slip-stick-jump motion of the contact line, contact line slips on the horizontal surface, sticks after reaching the corner point and jumps from one pillar to the next. Corresponding dynamic contact angles are plotted on the right.

Figure 4.15: Droplet spreading dynamics over a topography composed of solid width = 0.05 and gap = 0.1 for advancing contact angle of 90°. Liquid starts its downward motion on the first corner point before the interface touches the adjacent pillar.

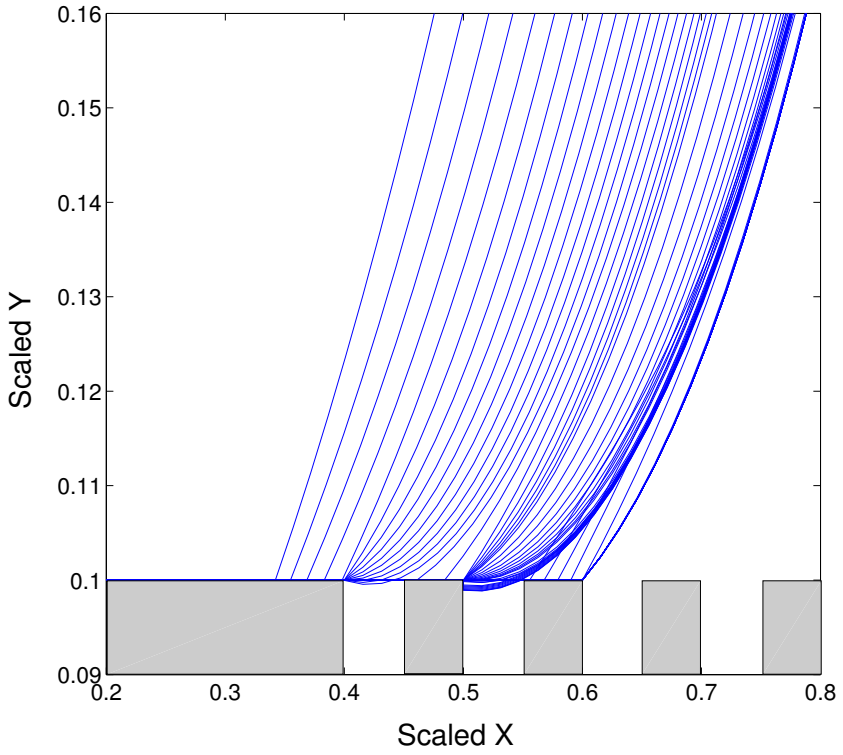

(a) Time evolution of the droplet shape near the contact line region. Droplet achieves a final equilibrium shape at the pinning point located at $X = 0.6$.

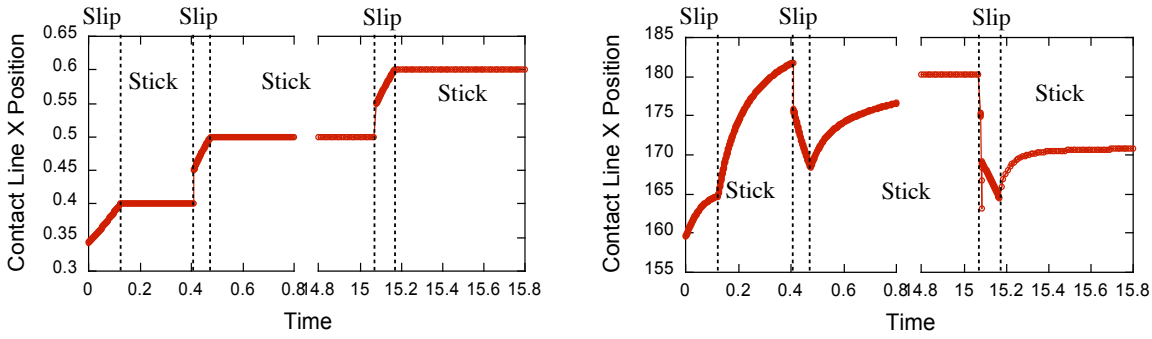

(b) Left hand side plot shows slip-stick-jump motion of the contact line, contact line slips on the horizontal surface, sticks after reaching the corner point and jumps from one pillar to the next. Corresponding dynamic contact angles are plotted on the right.

Figure 4.16: Droplet spreading dynamics over a topography composed of solid width = 0.05 and gap = 0.05 for advancing contact angle of 90°. Downward motion of the interface on the second pillar is more clearly seen before the interface touches the adjacent pillar.

and relative motion of the depositing needle with the surface) the droplet initially starts spreading with a larger base radius, then as it spreads it will come across the pinning points that are ahead of the initial base radius. In that case, droplet will be pinned at a farther distance from the symmetry axis and for a given volume, it will achieve lower equilibrium contact angle corresponding to the location of the corner point. Thus apparent equilibrium contact angle achieved is dependent on location of pinning points, volume of the droplet, and history of the droplet spreading.

Appendix A: Curvature Calculation

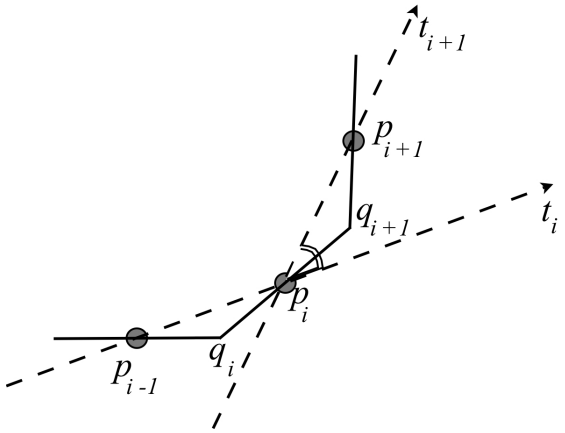

Figure A.1: Geometry for curvature calculation.

Fig. (A.1) shows a geometry for curvature calculation, where t_i and t_{i+1} are tangents at q_i and q_{i+1} respectively obtained by joining the p's. Then curvature (κ) at point p_i is defined as $\frac{d\Theta_i}{ds}$; where $d\Theta_i$ is change in the angle between the tangents and ds is the arc-length over which change has taken place (here, $ds = |q_{i+1} - q_i|$).

$$\kappa = \frac{d\Theta_i}{|q_{i+1} - q_i|} \tag{A-1}$$

Appendix B: Central Difference Scheme

Referring to the Fig. A.1 arc-length is defined as,

$$s_i = |q_i - p_{i-1}| + |p_i - q_i| \tag{B-1}$$

Expanding Ψ_{i-1} and Ψ_{i+1} around Ψ_i,

$$\Psi_{i-1} = \Psi_i - s_i \frac{\partial \Psi_i}{\partial s} + \frac{s_i^2}{2} \frac{\partial^2 \Psi_i}{\partial s^2} + O(s_i^3) \tag{B-2}$$

$$\Psi_{i+1} = \Psi_i + s_{i+1} \frac{\partial \Psi_i}{\partial s} + \frac{s_{i+1}^2}{2} \frac{\partial^2 \Psi_i}{\partial s^2} + O(s_{i+1}^3) \tag{B-3}$$

Eliminating second derivative from above 2 equations, we get a central difference scheme for first derivative,

$$\frac{\partial \Psi_i}{\partial s} = \frac{s_i^2 \Psi_{i+1} + (s_{i+1}^2 - s_i^2)\Psi_i - s_{i+1}^2 \Psi_{i-1}}{s_{i+1}^2 s_i + s_i^2 s_{i+1}} \tag{B-4}$$

Similarly, eliminating first derivative from the two equations we get central difference scheme for second derivative,

$$\frac{\partial^2 \Psi_i}{\partial s^2} = \frac{s_i \Psi_{i+1} - (s_i + s_{i+1})\Psi_i - s_{i+1} \Psi_{i-1}}{\frac{1}{2}(s_{i+1}^2 s_i + s_i^2 s_{i+1})} \tag{B-5}$$

One sided difference is also used in our code for the corner points, derivation of which is similar to shown above. For example, ψ_{i+1} and ψ_{i+2} are expanded around ψ_i and similar elimination procedure is applied.

Appendix C: Integration of Young-Laplace equation

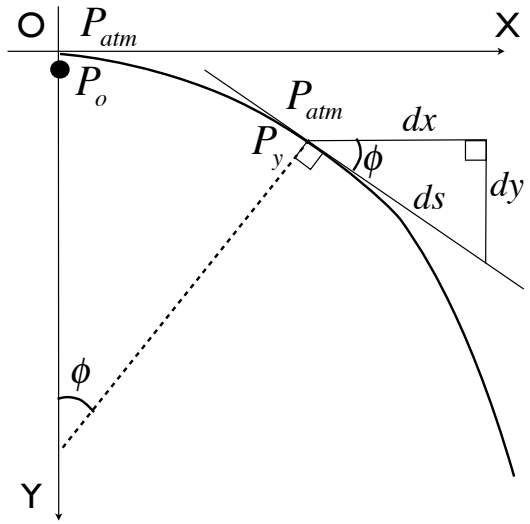

Figure C.1: Arc angle formulation for integrating the Young-Laplace equation.

Interfacial shape of a sessile (or pendant) drop (or bubble) is governed by classical Young-Laplace equation,

$$\Delta P = \gamma\kappa = \frac{\gamma}{R} \tag{C-1}$$

where ΔP is Laplace pressure difference across the interface, which is balanced by surface tension γ times curvature κ of the interface, R is radius of curvature. Equilibrium shape of any interface can be obtained by integration of above equation.

Consider a droplet interface as shown in Fig. C.1 with its apex at origin, "O", and is symmetrical about Y axis. Air around the droplet is at constant atmospheric pressure, P_{atm}. Angle measured from the symmetry axis to any point on the interface is ϕ, where arc length is ds. Then at any point,

$$\frac{dx}{ds} = \cos\phi \tag{C-2}$$

$$\frac{dy}{ds} = \sin\phi \tag{C-3}$$

P_o is the pressure at the origin just beneath the interface and R_o is the radius of curvature at the origin. Applying Eq. C-1 at the origin, $P_o - P_{atm} = \gamma/R_o$. At any point is Young-Laplace equation becomes,

$$P_y - P_{atm} = \gamma\kappa = \gamma\frac{d\phi}{ds}$$

where P_y is pressure at any point in liquid, $P_y = P_o + \rho g y$. Therefore,

$$\begin{aligned} P_o - P_{atm} + \rho g y &= \gamma\tfrac{d\phi}{ds} \\ \tfrac{\gamma}{R_o} + \rho g y &= \gamma\tfrac{d\phi}{ds} \\ 1 + \tfrac{\rho g R_o^2}{\gamma} y' &= \tfrac{d\phi}{ds'} \end{aligned}$$

where y' and s' are nondimensionalized y and s by radius of curvature at the origin,R_o. Thus we get,

$$1 + Bo.y' = \frac{d\phi}{ds'} \tag{C-4}$$

where Bo is the dimensionless number called as Bond number, which is a ratio of body forces to the surface tension forces. Hence in order to obtain equilibrium shape of a droplet we need to solve equations C-2, C-3 and C-4. And Bond number is the only dimensionless parameter in the equations which governs the shape of the droplet.

Algorithm for obtaining equilibrium shape of a droplet is as follows. Initially guess a value for R_o, evaluate Bond number. Solve equations C-2, C-3 and C-4 with initial conditions as $x(0) = 0, y(0) = 0$ and $\phi(0) = 0$. Compute volume at each incremental Δs and when desired volume is reached integration is stopped. At this volume check the final contact angle, if not correct change value of R_o and iterate till the right contact angle is obtained at correct volume of the droplet.

As we can see from this procedure that the interfacial shape is solely governed by Bond number and solid surface topography does not play any role in these equations.

Appendix D: Liquid Meniscus Shape over the Trapped Air

When droplet is riding over a composite surface of solid and air, in Cassie-Baxter regime, air-liquid interface from this composite surface is considered to be flat in numerical simulations presented in Section 4.4. We have also examined dynamic droplet shapes with considering curvatures of the liquid menisci in between the two pillars. Fig. D.1 shows two different simulations over a topography composed of pillar width = 0.04 and gap = 0.04, while pillar are located at different locations. We see that the free interface in between the pillars have certain curvature and it relaxes as a function of time to reach an equilibrium curvature value. Curvatures of these menisci are of the order 1 and the scale of the microstructures is of the order 0.01. Thus, the final curvature obtained is very small as compared to the gap between the pillars, it appears in the figures because the scale of the Y axis is much expanded as compared to X axis scale. Moreover, the final equilibrium contact line position and apparent contact angle, obtained with curvature consideration, falls exactly on the on the extent of spreading curve for volume V1 in Fig. 4.7, which is obtained for a flat surface. Therefore we can conclude that the droplet dynamics and final equilibrium shape obtained is only controlled by contact line motion and free interfacial shape above the solid. And it is a valid assumption that the interface can be considered to be flat as in the simulations presented in Section 4.4.

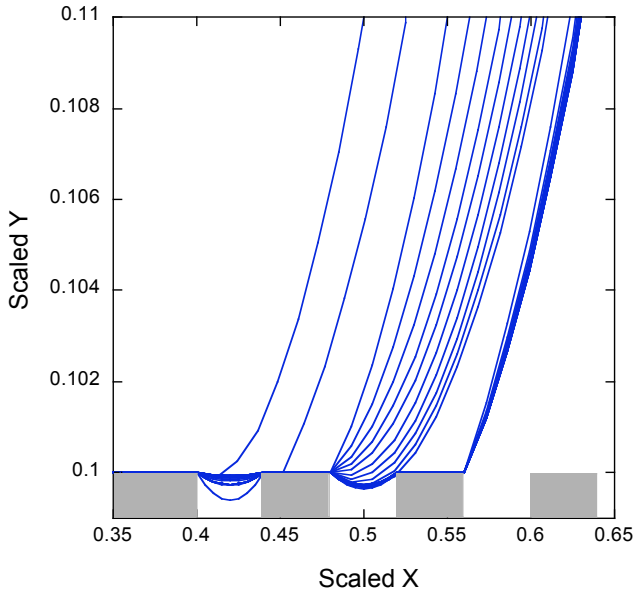

(a) Final pinning location $X = 0.52$, $\theta^*_{eq} = 178.7$

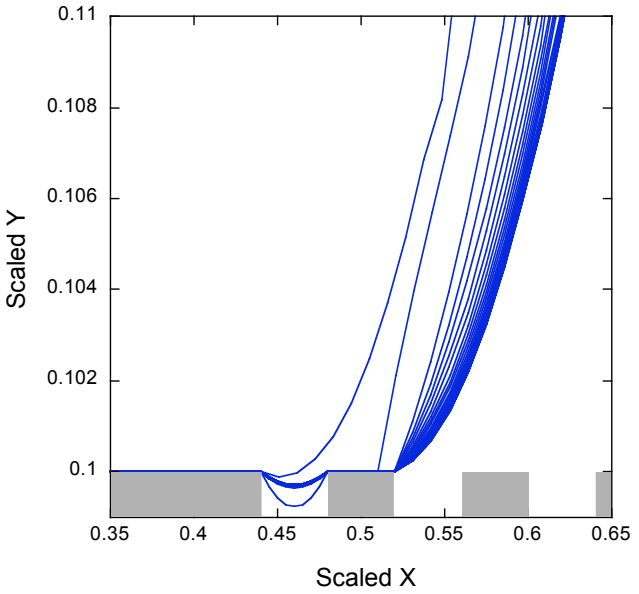

(b) Final pinning location $X = 0.56$, $\theta^*_{eq} = 174.8$

Figure D.1: Droplet spreading over a topography with tangential and normal stress balances are solved on the menisci in between the two pillars. Droplet initially spreads on a flat surface and then encounters a topography of pillar width = 0.04 and gap = 0.04.

Chapter 5

Experimental Studies

This chapter presents experimental investigations of the hydrodynamic movement of droplets over regularly arrayed microtextured superhydrophobic surfaces which we fabricate using soft lithography. In order to be able to compare these experiments to the theoretical results described in the previous chapter on the two dimensional movement of droplets over pillars, the microtextured surface we construct consists of parallel grooves. A fluid droplet placed on this geometry, as it moves perpendicular to the grooves, forms a blunt edge parallel to the grooves which simulates the two dimensional motion modeled in the previous chapter. In section 5.1 we review the soft lithography methods used for fabricating regular/periodic micron scale patterns on a surface. To demonstrate in general how surfaces with regularly arrayed features can be superhydrophobic, in the following section 5.2 we fabricate surfaces with two dimensional arrays of pillars and holes, and measure the equilibrium contact angles of aqueous droplets placed on the surface by imaging the droplets on the surfaces. This imaging also reveals the Cassie-Baxter wetting conditions on the surface. The measured contact angles are then compared with the Cassie-Baxter equation. In the next section 5.3, the experiments on the grooved surfaces are described, and compared to the results of the two dimensional simulations of the previous section.

Experimentally droplet dynamics is studied by two procedures: firstly under gravity driven spreading and secondly with controlled spreading, i.e. by increasing the volume of the droplet gradually with time.

5.1 Soft Lithography Fabrication of Microtextured Surfaces

The fabrication of microtextured surfaces which can trap air as a liquid moves over the surface, and can therefore allow aqueous droplets to subtend large equilibrium contact angles (superhydrophobicity), were first made using chemical deposition methods forming irregular surface topographies. Researchers at Kao Corporation [84] were the first to make such a superhydrophobic surface in 1996. They prepared a surface with a fractal topography from an alkylketene dimer (AKD – a kind of wax), and obtained a water contact angle of 174°. After this successful demonstration of superhydrophobicity, a number of different ways to produce superhydrophobic rough surfaces have emerged in the last decade. For details of the experimental work in this field one can refer to reviews published by Zhang et al[22] and Ma et al[17]. Soft-lithographic techniques have been used for fabricating superhydrophobic surfaces in which the microtextures are formed in a regular pattern [85, 86, 87]. These surfaces are made from PDMS, poly (dimethylsiloxane). Fig. (5.1) illustrates the major fabrication steps. The microstructures are molded onto the surface of a PDMS monolith by casting the uncured liquid PDMS over a master relief of the negative of the microstructures. The master is formed by photolithography on the surface of a photoresist which is spin coated on the surface of a silicon wafer. For preparation of this master on the silicon wafer, we first clean the wafer with the standard technique of a series of chemical washes with acetone, iso-propyl alcohol and de-ionized water and then blow dried with nitrogen gas. We spin-coated a thin layer of negative-toned photoresist (SU-8

2050, MicroChem Corporation, Newton, MA) onto the cleaned silicon wafer. The desired film thickness is achieved by tuning the spinning conditions such as rpm, acceleration and spinning time. The silicon wafer along with the SU-8 layer is then baked (pre-exposure bake) over a hot plate before exposing to UV light (at 365 nm) through a transparency mask. High resolution transparency masks were printed from Pageworks, Cambridge, MA, which consist of the negatives of required designs to be patterned on the PDMS surface. Exposing the SU-8 layer, on the silicon wafer substrate, to UV light at the prescribed exposure energy causes the photoinduced cross-linking reaction and as a result only part of the SU-8 which is exposed through the transparency gets cross-linked. After UV exposure, the photoresist layer is baked again on a hot plate (post-exposure bake). Patterns were developed on the master by

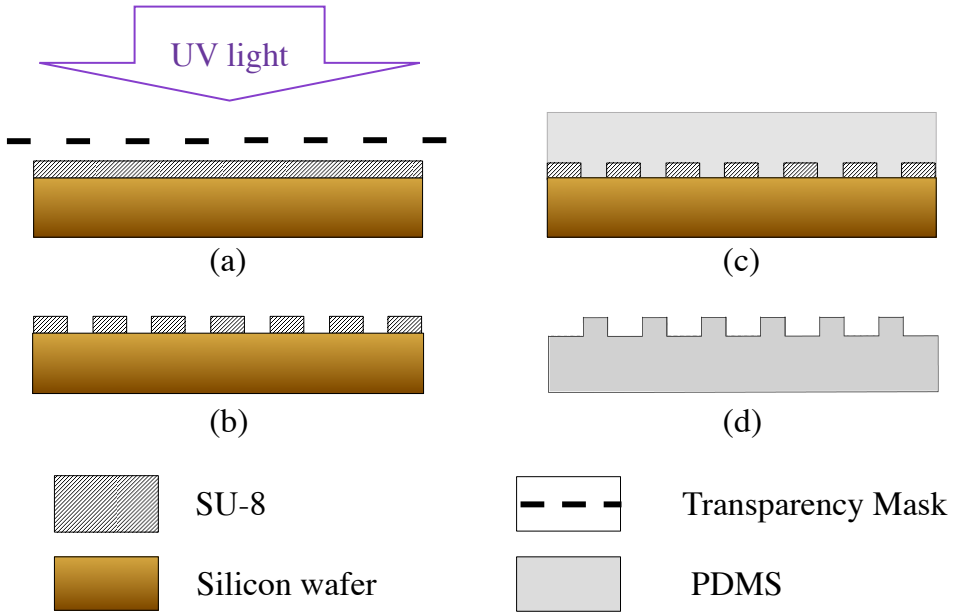

Figure 5.1: Fabrication of patterned PDMS surface: (a) UV-exposure of SU-8 resist through transparency mask, (b) Master prepared after washing off unpolymerized SU-8, (c) PDMS-prepolymer mixture poured over the master and cured in oven, (d) PDMS surface with micro-patterns is obtained after peeling-off from the master.

immersing the wafer in the developing solution (SU-8 developer, MicroChem Corporation, Newton, MA), to remove uncross-linked SU-8 from the wafer. Optimum pa-

rameters for the SU-8 fabrication process (including spin-coating rpm, baking times, UV light exposure energy) are obtained from the datasheet provided by MicroChem corporation [88]. To make the PDMS peel-off easy, the exposed silicon wafer on the master was made hydrophobic by reacting it with perfluorosilane. The surface modification reaction was carried out by dissolving 10μl of (Heptadecafluoro-1,1,2,2-tetrahydrodecyl)trichlorosilane (Gelest Inc, Morrisville, PA)) into 25ml of chloroform and then the master was immersed into the solution. After 2 hours, the master was removed, blow dried with N_2 and heat treated for 20 min at 115°C.

For the the fabrication of the PDMS surface, the PDMS prepolymer mixture is prepared by mixing the prepolymer with a curing agent (Sylgard 184 Silicone Elastomer Kit, Dow Corning, Midland, MI) in a 10:1 weight ratio. The prepolymer mixture was then thoroughly mixed and defoamed in a centrifugal Thinky Mixer (AR-100, Thinky Corporation, Tokyo, Japan). The PDMS prepolymer mixture was then poured onto the master and trapped air in the patterns was removed by applying vacuum for 30 min. The PDMS mixture was then cured in an oven at 65°C for 2 hours. The PDMS replica was then gently peeled off from the master.

Different structured patterns of PDMS surfaces were prepared like a regular array of square pillars, square holes, and circular pillars. SEM images of the patterned PDMS surfaces were taken (Fig. 5.2) with a Zeiss Evo 40 operated at 10kV. Images were recorded under variable pressure (VP) mode at 40 Pa. Samples were also characterized under an optical microscope to get quantitative data about the structures.

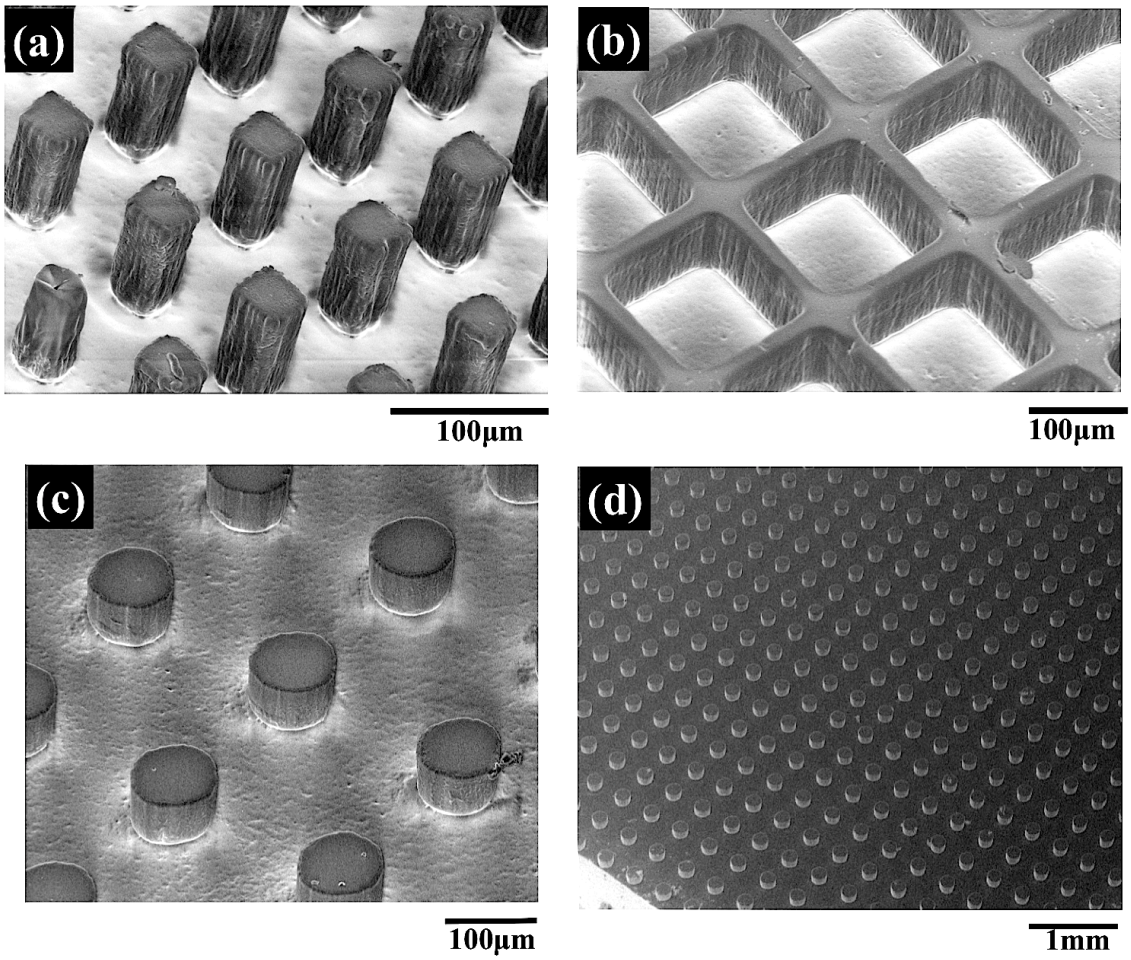

Figure 5.2: Scanning Electron Microscopy images of the fabricated PDMS surfaces: (a) Square pillars (SP), (b) Square wells (SW), (c) and (d) Circular pillars (CP). Scale bar is shown at the bottom-right corner of each image.

5.2 Contact Angle Measurements of Water Droplets on Microtextured Surfaces of Arrayed Pillars and Wells

As a measure of the hydrophobicity, water contact angle measurements were performed on different PDMS surfaces. Measurements were performed with deionized water and surfaces were cleaned to remove dust particles simply by blowing nitrogen

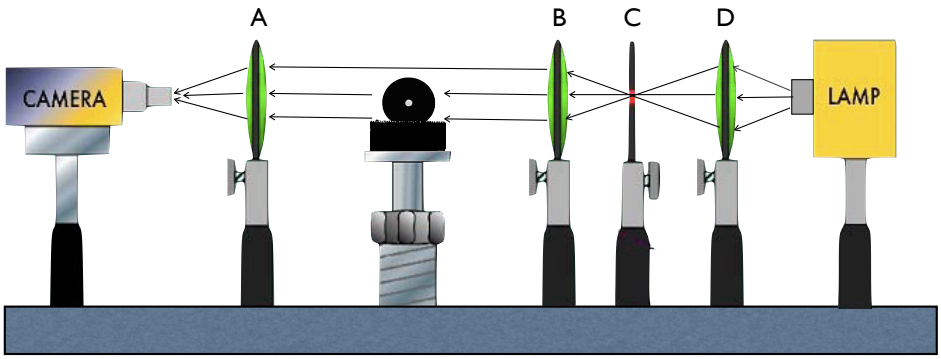

Figure 5.3: Schematics of Video Microscopy apparatus used for imaging the droplets: A, Objective lens; B, collimating lens; C, pinhole; D, focussing lens

gas over it. A pendant bubble/sessile drop video microscopy setup was used to image the droplet, from which the contact angle was then obtained. Fig.(5.3) shows the video microscopy setup, in which light is collimated by using a series of optics, and then imaged by a CCD camera which is connected to a computer. Images recorded are shown in the Fig.(5.4) with respective contact angles for a constant droplet volume of $6\mu l$. Light coming from beneath the drop is an indication of the Cassie-Baxter kind of wetting and the droplet resting on a composite surface of solid and air. Approximately a 40° jump in the water contact angle was observed between the flat and the roughened surfaces. Table 5.1 compares the experimentally observed water contact angles (θ_{exp}) with the predicted values from Wenzel's approach (θ_w) and the Cassie-Baxter's approach (θ_c). We can see that the experimental values are closer to that predicted by the Cassie-Baxter's relation. This also conforms that the droplet is riding on a composite surface rather than having a fully wetted contact with the solid.

A necessary condition for the Cassie-Baxter contact angle equation to be valid is that the droplet edge has to move across several features before achieving equilibrium. In this way, the variation in the free energy for an area change δA can be represented in terms of the solid area fraction as given by 4.6. In these experiments, the droplet was

placed on the surfaces with a hand-held syringe. Attendant to this way of placing the droplet on the surface are oscillations due to inertial effects which force the droplet to jump/explore the neighboring pillars. In the case of water, these oscillations are not damped by the liquid viscosity. These oscillations allow the droplet edge to overshoot local surface energy minima and arrive at the global minimum represented by the Cassie-Baxter equation. In this way the droplets are not trapped in local minima with larger contact angles. Literature values for the contact angles of aqueous drops on microtextured surfaces such as the ones fabricated in this study show this general agreement with the Cassie-Baxter equation ([85, 86, 87]). As we will show in the next section, in the case in which the droplet is placed more carefully on the surface and a more high viscosity liquid is used to damp the oscillations, droplets can get trapped in local minima in accordance with the simulations of the previous chapter.

Table 5.1: Comparing experimentally observed contact angle with that predicted from Wenzel and Cassie-Baxter theory; where a is side of a square, d is diameter of a circle, p is square pitch, and height $h = 100\mu m$.

No.	Surface Topology (in μm)	r	ϕ_s (in%)	θ_c	θ_w	θ_{exp}
1	Flat	1	100	-	-	105
2	SP, $a = 40, p = 100$	2.6	16	151.8	132.3	144
3	SW, $a = 170, p = 200$	2.85	27.75	142.6	137.5	145
4	CP, $d = 110, p = 250$	1.55	15	152.7	113.6	141
5	CP, $d = 130, p = 250$	1.65	21	147.6	115.3	128.4

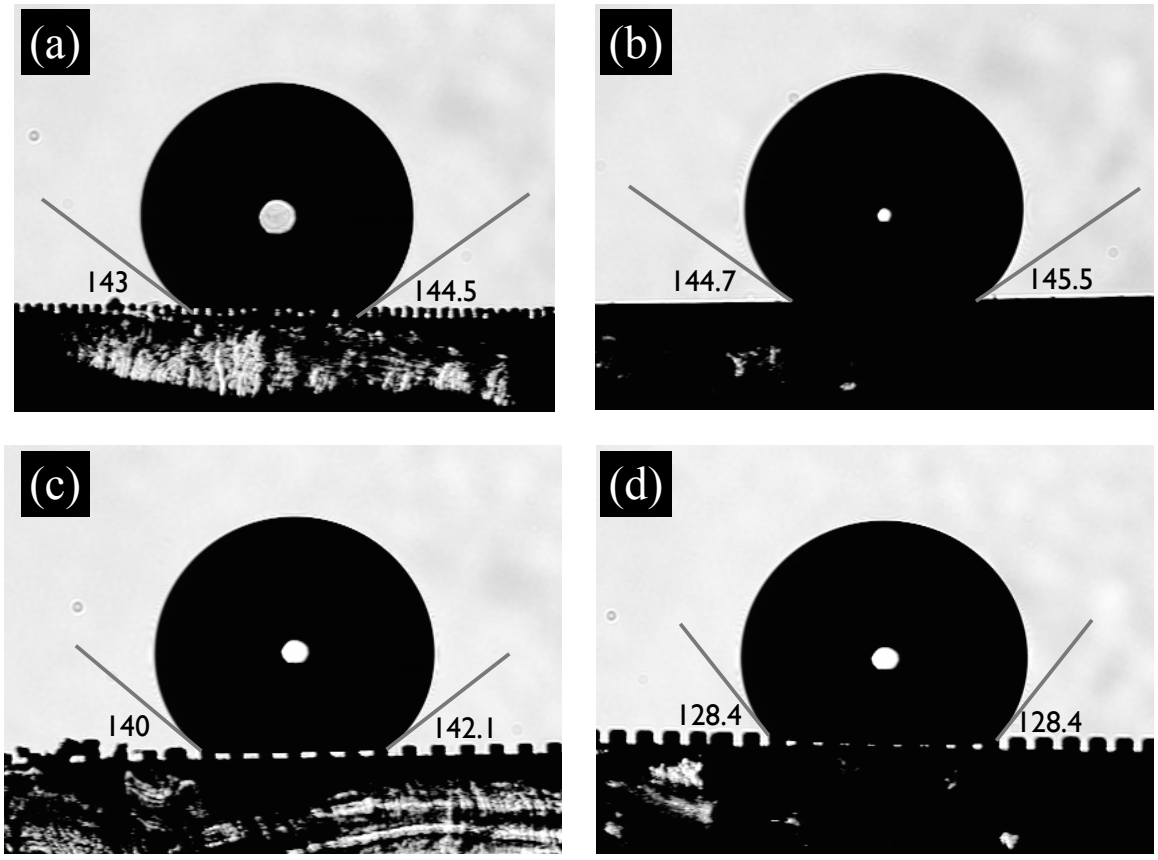

Figure 5.4: Contact angles as measured from the images obtained from video microscopy on (a) Square pillars (SP); (b) Square wells (SW); (c) and (d) Circular pillars (CP).

5.3 Dynamics of a Droplet Spreading over a Superhydrophobic Surface

5.3.1 Gravity driven spreading of a droplet

To study the gravity driven spreading dynamics of a droplet and to have somewhat similar conditions like our simulations, we fabricate surfaces that have microstructures in the form of long parallel grooves as opposed to pillars. SEM images of such fabricated anisotropic surfaces are shown in Fig. 5.5. When aqueous droplets are used, because of the low viscosity of water, the spreading dynamics is very fast. If

we compute a characteristic velocity, $V' = \rho g a^2/\mu$, for water, $V' \sim O(10)$ m/s and the corresponding Reynolds number, $Re = aV'\rho/\mu \sim O(10^4)$. Thus, the Stokes flow assumption of the two dimensional theory is definitely not valid. Therefore, we use glycerol instead of water because glycerol exhibits very similar contact angles on the flat PDMS surface as that of water ($\theta_{gly} = 100^\circ$ and $\theta_{wat} = 103^\circ$). The advantage of using glycerol over water is that its viscosity is 1.2 Pa.s (1200 times viscosity of the water). Hence, the characteristic velocity for glycerol, $V' \sim O(0.01)$ and the corresponding Reynolds number is $Re \sim O(0.01)$.

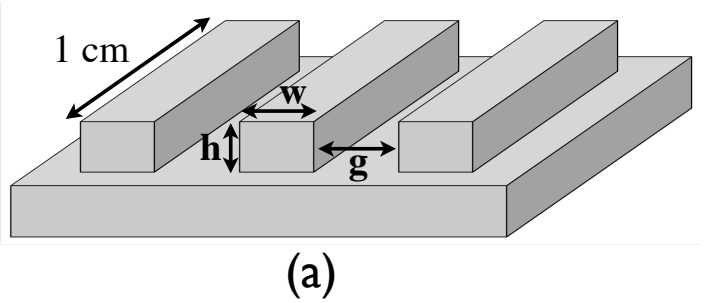

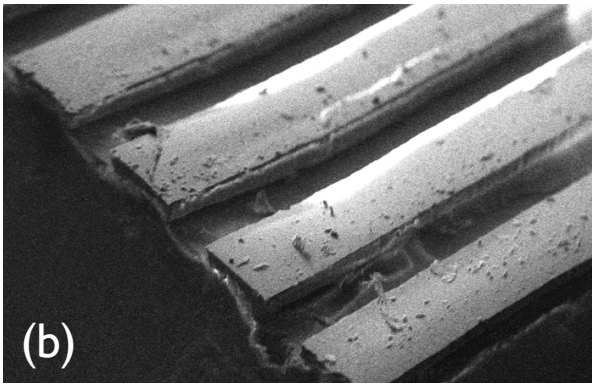

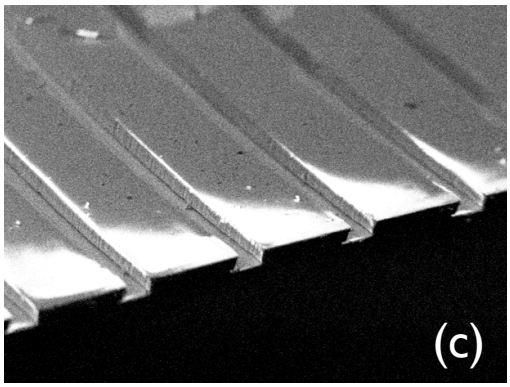

Figure 5.5: 2-D anisotropic parallel grooved/striped surfaces. (a) Schematic of striped surface with width w, height h and gap between the two stripes g. Length of these stripes is 1 cm, much longer as compared to w, g and h. (b) and (c) Scanning Electron Microscopy images with width w of 175 μm and 375 μm respectively. $g = 125\mu$m and $h = 100\mu$m in both cases.

To capture the dynamics of the droplet, glycerol drop was gently touched the solid surface while still attached to the needle and needle was gently pulled up, while clamped to a micro-positioner, so that the drop snaps off from the needle and spreads

under gravity over the parallel grooved surface. Its dynamics is visualized along the transverse direction (perpendicular to the grooves) with a fast video camera capable of capturing few thousand frames per second. Fig. 5.6 shows an experiment of gravity driven dynamics of glycerol droplet over a grooved surface of solid width 175μm and gap between the two pillars 125μm. Images were captured by the fast video camera at 2000 frames/second. Initially at time t=0 s droplet is attached to the needle and touching the top of three solid surfaces and contact line is pinned at the two corners (one on the either sides). During the snap-off process, as the needle was pulled up, interface bends over while still remaining pinned at the same corner points and while doing so interface just touches the neighboring pillar (on the left) at time t=0.0175 s. This initial contact point then becomes the new contact line position and new contact line slips over the top surface of the pillar from time t=0.0175 s to t=0.0265 s, at which time reaches the next pinning point located at the corner of the pillar. After time t=0.0265s contact line remains pinned (stuck) to the corner point and the contact angle increases till the droplet finally achieves an equilibrium at the new pinning position. During this process neck connecting the droplet with the needle thins and finally breaks. Equilibrium contact angle measured at the end of this process is 168.3°. The light coming from underneath the droplet again indicates the Cassie-Baxter kind of wetting where droplet rests on a composite surface of air and solid. For this surface if we calculate the average solid area fraction in the composite surface, we get $\phi_s = 0.5833$. By using Cassie-Baxter relation Eq.4.6, predicted equilibrium contact angle for this ϕ_s is $\theta^* = 121.19°$. This clearly indicates that Cassie-Baxter's relation fails to explain such a large equilibrium contact angle. Because droplet while spreading does not see an average solid area fraction of the composite surface but local surface properties. On the other hand, in our simulations we have observed multiple equilibrium contact angles depending upon the initial base radius and for smaller initial base radius we have observed contact angles of $\sim 170°$.

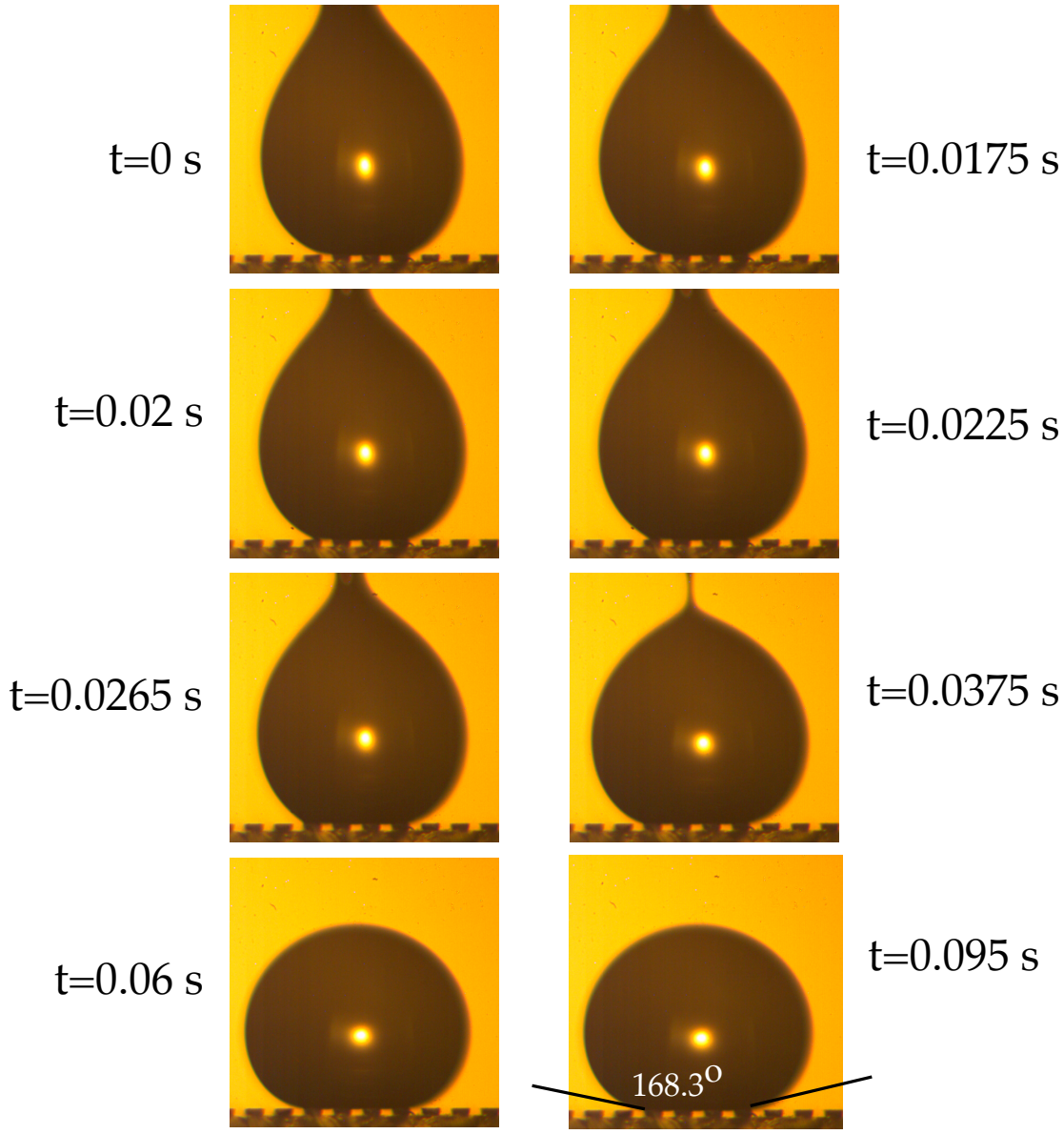

Figure 5.6: Gravity driven spreading motion of a glycerol droplet over a striped surface of solid width 175μm and gap 125μm. Images were recorded by a fast video camera at 2000 frames/sec. Droplet contact line shows distinct slip-stick motion after jumping to the adjacent pillar. Droplet interface touches the pillar on the left and slips over the surface till it sticks to the corner point.

Similar experiment of gravity driven spreading is shown in Fig. 5.7 on a grooved surface of solid width 375μm and gap 125μm. This experiment more clearly shows contact line's slip-stick motion after contact line jumps from its initial pinning point to neighboring pillar on the left at time t = 0.0417 s. Images were recorded at 6000

frames/sec. After going through similar steps droplet again comes to equilibrium at the corner point with final contact angle of $163 \pm 2°$. Average solid area fraction of the composite surface is $\phi_s = 0.75$ and Cassie-Baxter relation predicts $\theta^* = 113.14°$.

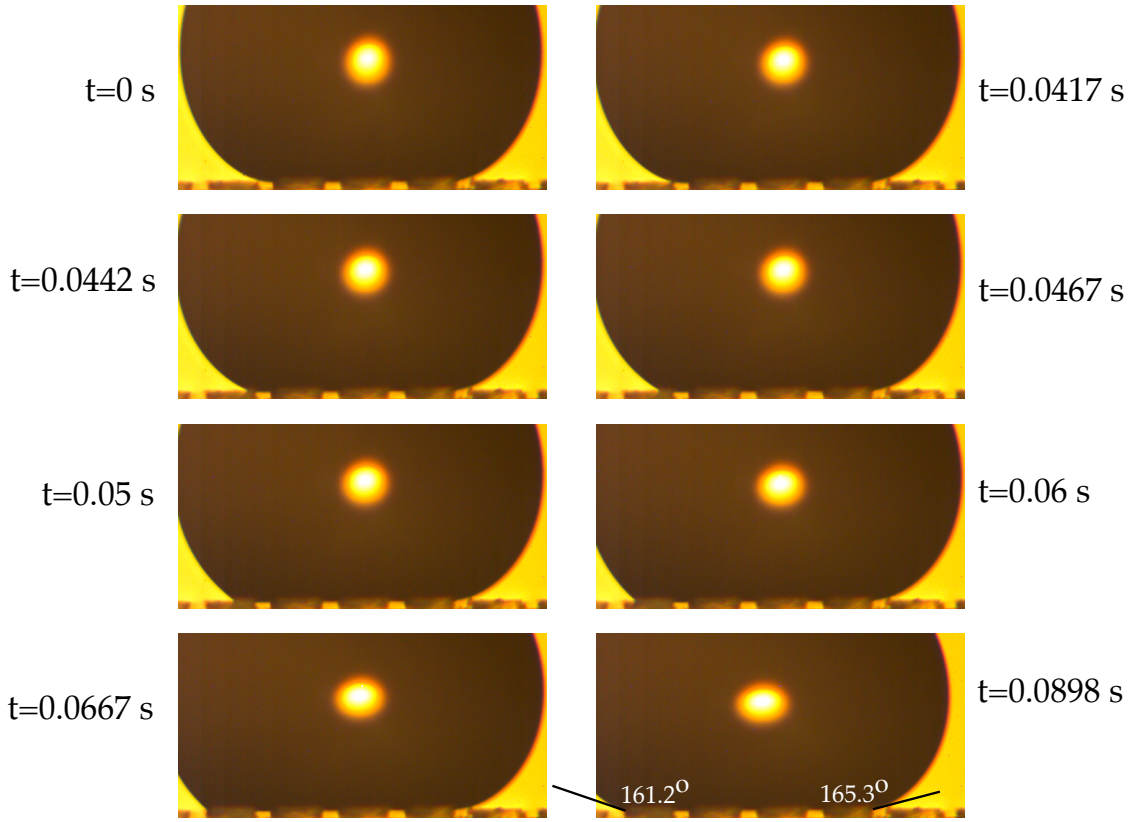

Figure 5.7: Gravity driven spreading motion of a glycerol droplet over a striped surface of solid width 375μm and gap 125μm. Images were recorded by a fast video camera at 6000 frames/sec. Droplet contact line shows distinct slip-stick motion after jumping to the adjacent pillar. Droplet interface touches the pillar on the left and slips over the surface till it sticks to the corner point.

5.3.2 Controlled spreading of a droplet

Slip-stick motion of the contact line is demonstrated in section 5.3.1 where dynamics was too fast and it is captured with a fast video camera. In order to have a closer look at the contact line pinning and available multiple contact angles as well as to minimize the effect of the second curvature in 3-D droplet a controlled spreading experiments were performed. In these experiments droplet contact line does not advance by gravity driven spreading motion but due to increase in volume of the droplet. Experimental arrangement is as follows. Microtextured surface used is again 1-D array of parallel grooved surface. Water is used as a liquid in these experiments as by controlling the rate of increase in the volume of the droplet we can still have stokes flow conditions. Volume of a droplet is increased with the help of a syringe pump which pumps the water at a very small rate through a needle which is attached at its end to a rectangular slit arranged above the surface with slit length aligned along the grooves. Water coming out of this slit forms a cylindrical droplet with axis of cylinder parallel to the grooves. This cylindrical shape of the droplet minimized effect of 3-D curvature and resembles more closely with the simulation conditions. Schematic of this experimental arrangement is shown in Fig. 5.8.

Fig. 5.9 shows one such typical experiment where volume of the droplet is increased gradually as the cylindrical drop forms over a surface consisting of stripes of 275 μm solid width and 125 μm gap. Flow rate to the droplet was maintained at 15 μl/min and droplet spreading is observed in a transverse direction through a CCD camera. Camera is focused in the middle of the cylindrical droplet in order to avoid any end effects and as a result the surface topography appears blurred or washed out. (When camera is focused on the front end of the surface topography looks very sharp, as in the previous results of gravity driven spreading.) Images were captured at the rate of 1 frame/sec. Figure shows time dependent droplet shape in the vicinity of the contact line, which is initially pinned at a corner point. When the flow into the

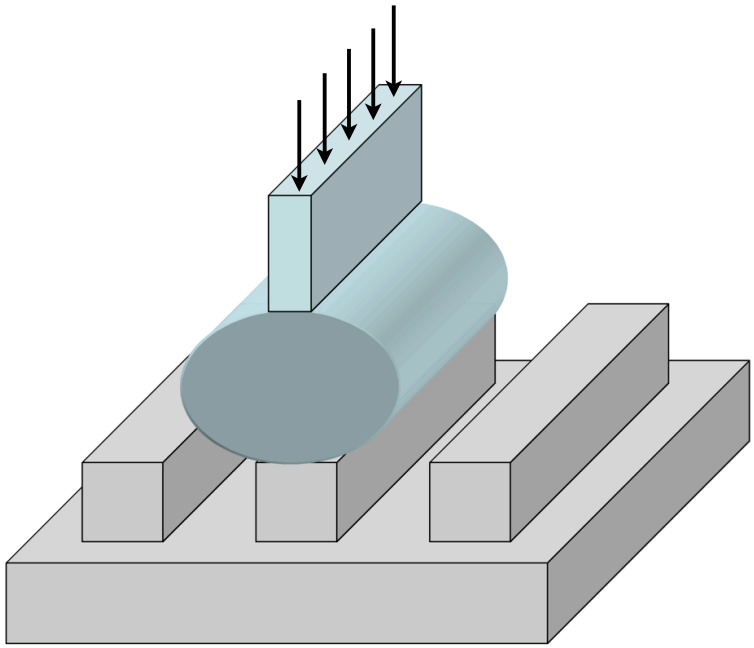

Figure 5.8: Schematic of the experimental arrangement for the controlled spreading of a cylindrical droplet over a parallel grooved surface. Droplet volume in increased by flow coming in through the slit.

droplet is started contact line remains pinned at the same location, however rest of the droplet is free to move and as a function of time droplet goes through multiple contact angles from 157° till very close to 180° after 47 sec where the free interface just touches the next pillar. As soon as the interface touches the neighboring pillar on the left, contact line quickly slips and sticks to the downstream end of the corner point within a second where contact angle is again about 157° and the process continues. Fig. 5.10 shows a very similar experiment on a surface with topography of solid stripes width 175 μm and gap between the stripes 125 μm. In this experiment flow rate through the slit was maintained at 10μl/min and images were captured at 1 frame/sec. These two experiments clearly confirms the presence of sharp pinning points and droplet can achieve any contact angle from the range permissible.

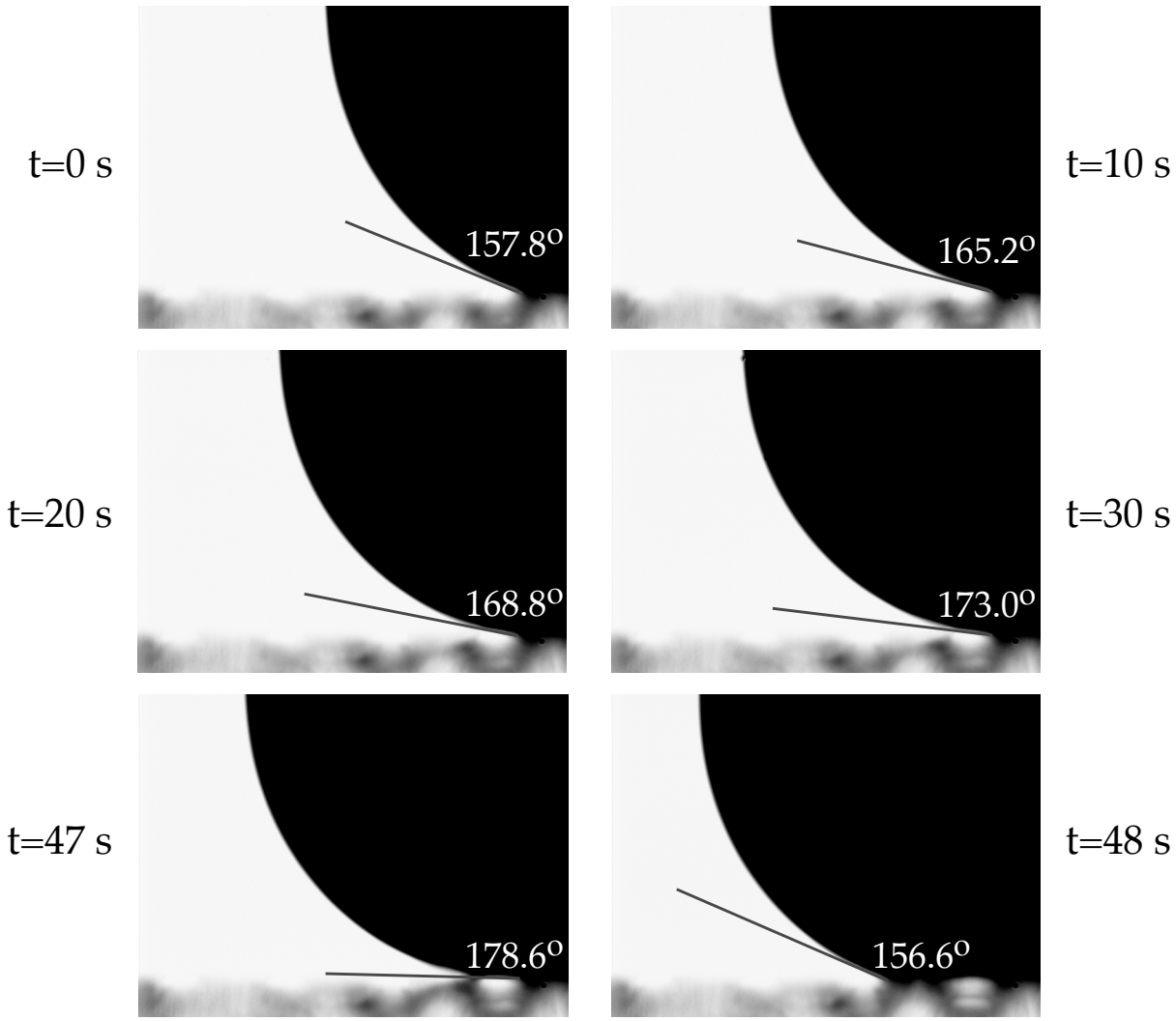

Figure 5.9: Controlled spreading of a 2-D droplet over a striped surface with $w = 275\mu$m, $g = 125\mu$m and $h = 100\mu$m. Flow rate through the slit = 15 μl/min, frame capture rate = 1 frame/sec. Droplet shows pinning at the corner point while its contact angle increases till time t=47 sec at which time the contact line jumps to the next pillar.

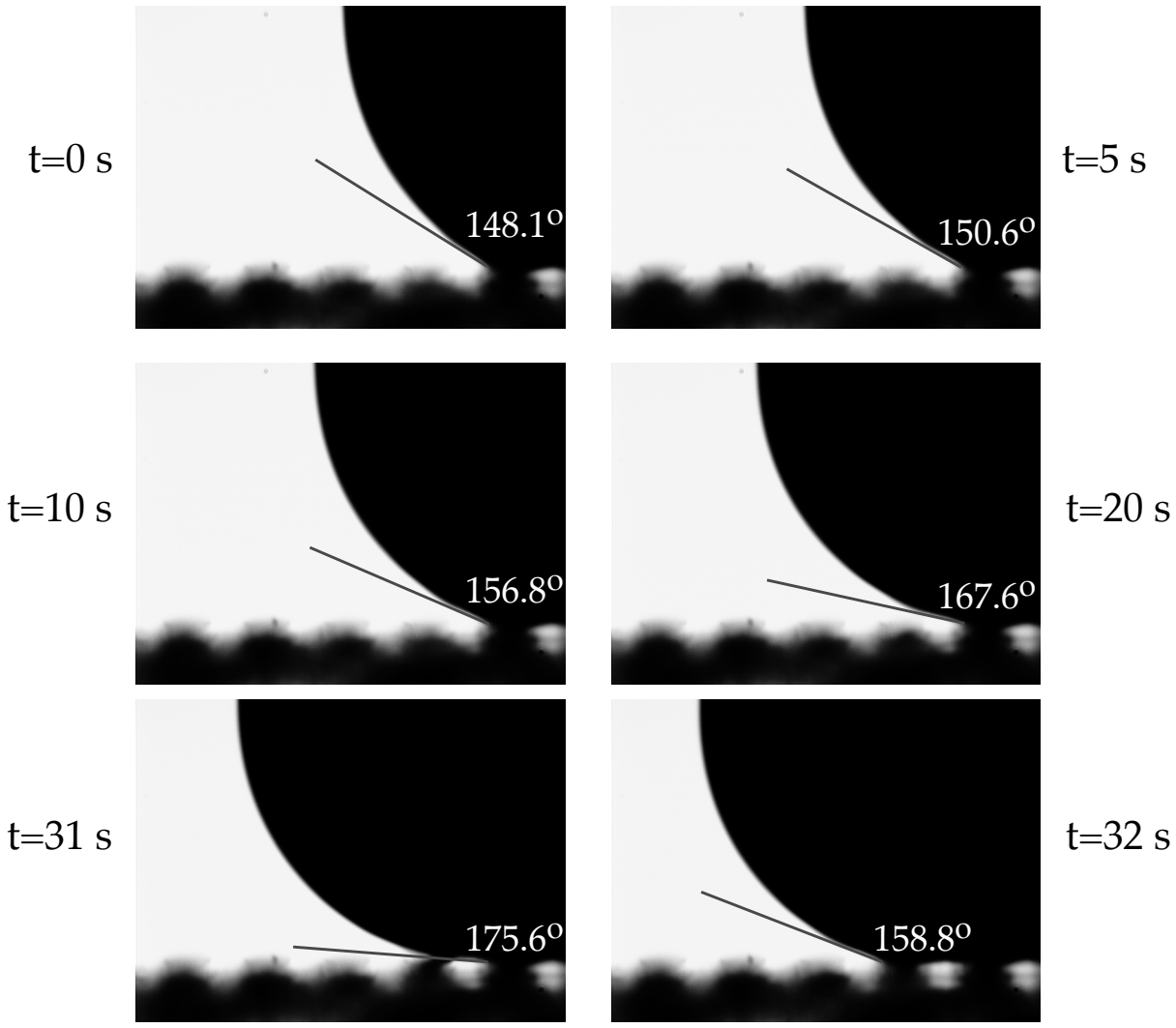

Figure 5.10: Controlled spreading of a 2-D droplet over a striped surface with $w = 175\mu$m, $g = 125\mu$m and $h = 100\mu$m. Flow rate through the slit = 10 μl/min, frame capture rate = 1 frame/sec. Droplet shows pinning at the corner point while its contact angle increases till time t=31 sec at which time the contact line jumps to the next pillar.

5.4 Conclusion

Superhydrophobic surfaces, of PDMS material, consisting of regular array of pillars are fabricated using soft-lithography technique. On 2-D array of posts and pores, water droplet placed clearly shows Cassie-Baxter kind of wetting and measured water contact angle value also fairly matches with the predictions from the Cassie-Baxter relation. Water droplet placed on these surfaces, from a hand-held syringe, were associated with large oscillations due to inherent inertia of the depositing and droplet snap-off process. This oscillations causes the droplet to overshoot local minima and arrive at an equilibrium which is closer to the global minimum, i.e. near Cassie-baxter equilibrium. However, when droplet is more carefully placed and is of higher viscosity, inertial effects are quickly damped and droplet motion is arrested at the first local minimum available. Dynamics of this viscous droplets studied with fast video camera reveal the same slip-stick motion (as simulations in Chapter 4) of the contact line and droplet achieves equilibrium while remaining pinned at a downstream end of the post of 1-D parallel grooved surface. Observed apparent equilibrium contact angle is much larger than the Cassie-Baxter prediction as the droplet remains pinned in the local minimum. Similarly, controlled spreading experiment reveals multiple contact angles provided by the corner point before the contact line jumps to the next available pillar. And the droplet interface indeed makes a contact angle near 180° before it advances to the next pillar. These observations are consistent with our numerical simulations presented earlier in Chapter 4 and reiterate the fact that wetting is a dynamic phenomena and equilibrium droplet contact angle on a textured surface is dependent upon the history of the droplet as well as available local minima in the form of pinning points.

Bibliography

[1] D Quéré, "Wetting and roughness", *Annu. Rev. Mater. Res.* **38**, pp. 16.1–16.29 (2008).

[2] J. Genzer and K. Efimenko, "Recent developments in superhydrophobic surfaces and their relevance to marine fouling: a review", *Biofouling* **22**(5), pp. 339–360 (2006).

[3] J. C. Berg, *Wettability*, Marcel Dekker (1993).

[4] R. G. Laughlin, *The Aqueous Phase Behavior of Surfactants*, Academic Press Inc. (1994).

[5] M. Rosen, *Surfactants and Interfacial Phenomena*, Wiley Interscience third edition (2004).

[6] R. Zana, editor, *Dynamics of Surfactant Self-Assemblies*, CRC Press Boca Raton (2005).

[7] R. Nagarajan and E. Ruckenstein, "Theory of surfactant self assembly: A predictive molecular thermodynamic approach", *Langmuir* **7**, pp. 2934–2968 (1991).

[8] J. Van Hunsel, G. Bleys, and P. Joos, "Adsorption kinetics at the oil/water interface", *Journal of Colloid and Interface Science* **114**(2), pp. 432–441 (1986).

[9] M. Ferrari, L. Liggieri, F. Ravera, C. Amodio, and R. Miller, "Adsorption kinetics of alkylphosphine oxides at water/hexane interface 1. pendant drop experiments", *Journal of Colloid and Intrface Science* **186**, pp. 40–45 (1997).

[10] L. Liggieri, F. Ravera, M. Ferrari, A. Passerone, and R. Miller, "Adsorption kinetics of phosphine oxides at water/hexane interface", *Journal of Colloid and Interface Science* **186**, pp. 46–52 (1997).

[11] D. Colegate and C. Bain, "Adsorption kinetics of micellar solutions of nonionic surfactants", *Physical Review Letters* **95**, pp. 198302 (2005).

[12] Q. Song, A. Couzis, P. Somasundaran, and C. Maldarelli, "A transport model for the adsorption of surfactant from micelle solutions onto a clean air/water interface in the limit of rapid aggregate disassembly relative to diffusion and supporting dynamic tension experiments", *Colloids and Surfaces A: Physicochemical Engineering Aspects* **282-283**, pp. 162–182 (2006).

[13] G.M. Whitesides and Laibnis P.E., "Wet chemical approaches to the characterization of wet chemical approaches to the characterization of organic surfaces: Self- assembled monolayers, wetting, and the physical-organic chemistry of the solid-liquid interface", *Langmuir* **6**(87-96) (1990).

[14] A. Ulman, "Formation and structure of self-assembled monolayers", *Chem. Rev.* **96**(1533-1554) (1996).

[15] T. Nishino, M. Meguro, K. Nakamae, M. Matsushita, and Y. Ueda, "The Lowest Surface Free Energy Based on -CF3 Alignment", *Langmuir* **15**, pp. 4321–4323 (1999).

[16] W. Barthlott and C. Neinhuis, "Purity of sacred lotus, or escape from contamination in biological surfaces", *Planta* **202**(1), pp. 1–8 (1997).

[17] M. Ma and R. M. Hill, "Superhydrophobic surfaces", *Current Opinion in Colloid & Interface Science* **11**(4), pp. 193–202 (2006).

[18] C.-H Choi and C.-J. Kim, "Large Slip of Aqueous Liquid Flow over a Nano-engineered Superhydrophobic Surface", *Physical Review Letters* **96**(6), pp. 1–4 (2006).

[19] J. P. Rothstein, "Slip on Superhydrophobic Surfaces", *Annual Review of Fluid Mechanics* **42**(1), pp. 89–109 (2010).

[20] R. Truesdell, A. Mammoli, P. Vorobieff, F. Swol, and C. Brinker, "Drag Reduction on a Patterned Superhydrophobic Surface", *Physical Review Letters* **97**(4), pp. 1–4 (2006).

[21] F. Shi, J. Niu, J. Liu, F. Liu, Z. Wang, X. Feng, and X. Zhang, "Towards understanding why a superhydrophobic coating is needed by water striders", *Adv. Mater.* **19**, pp. 2257–2261 (2007).

[22] X. Zhang, F. Shi, J. Niu, Y. Jiang, and Z. Wang, "Superhydrophobic surfaces: from structural control to functional application", *J. Mater. Chem.* **18**, pp. 621–633 (2008).

[23] S. Puvvada and D. Blankschtein, "Molecular-thermodynamic approach to predict micellization, phase behavior and phase separation of micellar solutions. 1. application to nonionic surfactants", *Journal of Chemical Physics* **92**, pp. 3710–3724 (1990).

[24] R. Nagarajan and E. Ruckenstein, "Self assembled systems", In J. Sengers, R. Kayser, C. Peters, and H. White, editors, *Equations of State for Fluids and Mixtures* chapter 15. IUPAC Elsevier (2000).

[25] B.A. Noskov, "Kinetics of adsorption from micellar solutions", *Advances in Colloid and Interface Science* **95**, pp. 237–293 (2002).

[26] M. Kahlweit and M. Teubner, "On the kinetics of micellization in aqueous solution", *Advances in Colloid and Interface Science* **13**, pp. 1–64 (1980).

[27] E.A.G. Aniansson and S.N. Wall, "On the kinetics of step-wise micelle association", *The Journal of Physical Chemistry* **78**(10), pp. 1024–1030 (1974).

[28] E.A.G. Aniansson and S.N. Wall, "A correction and improvement of "on the kinetics of step-wise micelle association"", *The Journal of Physical Chemistry* **79**(8), pp. 857 (1975).

[29] E.A.G. Aniansson, S.N.Wall Wall, M. Almgren, H. Hoffmann, I. Kielmann, W. UIbricht, R. Zana, J. Lang, and C. Tondre, "Theory of the kinetics of micellar equilibrium and quantitative interpretation of chemical relaxation studies of micellar solutions of ionic surfactants", *The Journal of Physical Chemistry* **80**(9), pp. 905–922 (1976).

[30] S. N. Wall and E.A.G. Aniansson, "Numerical calculations on the kinetics of stepwise micelle association", *The Journal of Physical Chemistry* **84**, pp. 727–736 (1980).

[31] Suwimon Ariyaprakai and Stephanie R. Dungan, "Contribution of molecular pathways in the micellar solubilization of monodisperse emulsion droplets", *Langmuir* **24**(7), pp. 3061–3069 (2008).

[32] Chien-Hsiang Chang and E Franses, "Adsorption dynamics of surfactants at the air/water interface: A critical review of mathematical models, data and mechanisms", *Colloids and Surfaces A: Physicochemical and Engineering Aspects* **100**, pp. 1–45 (1995).

[33] A. Prosser and E. Franses, "Adsorption and surface tension of ionic surfactants at the air-water interface: review and evaluation of equilibrium models", *Colloids and Surfaces A: Physicochemical and Engineering Aspects* **178**, pp. 1–40 (2001).

[34] M. Schonhoff and O. Soderman, "Pfg-nmr diffusion as a method to investigate the equilibrium adsorption dynamics of surfactants at the solid/liquid interface", *The Journal of Physical Chemistry B* **101**, pp. 8237–8242 (1997).

[35] N. Kamenka, M. Puyal, B. Brun, G. Haouche, and B. Lindman, In K.L. Mittal and B. Lindman, editors, *Surfactants in Solution* volume 1 , p. 359. Plenum New York (1984).

[36] J. Brinck, B. Jonsson, and F. Tiberg, "Kinetics of nonionic surfactant adsorption and desorption at the silica-water interface: One component", *Langmuir* **14**, pp. 1058–1071 (1998).

[37] Fredrik Tiberg, Bengt Joensson, Ji-an Tang, and Bjoern Lindman, "Ellipsometry studies of the self-assembly of nonionic surfactants at the silica-water interface: Equilibrium aspects", *Langmuir* **10**(7), pp. 2294–2300 (1994).

[38] W. Brown, R. Stilbs, and B. Lindman, "Size and shape of nonionic (c12e6) micelles in dilute aqueous solutions as derived from quasielastic light scattering, sedimentation and pulsed field gradient nuclear magnetic resonance self diffusion data", *Journal of Chemical Physics* **87**, pp. 4548–4553 (1983).

[39] Wyn Brown and Roger Rymden, "Static and dynamic properties of a nonionic surfactant (c12e6) in aqueous solution", *Journal of Physical Chemistry* **91**, pp. 3565–3571 (1987).

[40] Wyn Brown, Zhou Pu, and Roger Rymden, "Size and shape of nonionic micelles: Nmr self-diffusion and static and quasi-elastic light scattering measurements on

c12e5, c12e7 and c12e8 in aquoeus solution", *Journal of Physical CHemistry* **92**, pp. 6086–6094 (1988).

[41] W. Richtering, W. Burchard, E. Jahns, and H. Finkelmann, "Light scattering from aqueous solutions of a nonionic surfactant (c14e8) in a wide concentration range", *Journal of Physical Chemistry* **92**, pp. 6032–6040 (1988).

[42] D. Wakefield and K. Marsh, "Viscosities of nonelectrolyte liquid mixtures. i. n-hexadecane and n-octane", *International Journal of Thermophysics* **8**(6), pp. 649–662 (1987).

[43] S. Yoshimura, S. Shirai, and Y. Einaga, "Light-scattering characterization of the wormlike micelles of hexaoxyethylene dodecyl $c_{12}e_6$ and hexaoxyethylene tetradecyl $c_{14}e_6$ ethers in dilute aqueous solution", *J. Phys. Chem. B* **108**(40), pp. 15477–15487 (2004).

[44] N. Hamada and Y. Einaga, "Effects of hydrophobic chain length on the characteristics of the micelles of octaoxyethylene tetradecyl c14e8, hexadecyl c16e8 and octadecyl c18e8 ethers", *J. Phys. Chem. B* **109**, pp. 6990–6998 (2005).

[45] Tadashi Kato, Toshiaki Terao, and Tsutomu Seimiya, "Intermicellar migration of surfactant molecules in entangled micellar solutions", *Langmuir* **10**, pp. 4468–4474 (1994).

[46] Tadashi Kato and Daisuke Nozu, "Structure and dynamics of concentrated micellar phase in nonionic surfactant-water systems", *Journal of Molecular Liquids* **90**, pp. 167–174 (2001).

[47] Julian Eastoe, James Dalton, Philippe Rogueda, Esther Crooks, Alan Pitt, and Elizabeth Simister, "Dynamic surface tensions of nonionic surfactant solutions", *Journal of Colloid and Interface Science* **188**, pp. 423–430 (1997).

[48] A. Patist, S.G. Oh, R. Leung, and D.O. Shah, "Kinetics of micellization: Its significance to technological processes", *Colloids and Surfaces A: Physicochemical and Engineering Aspects* **176**, pp. 3–16 (2001).

[49] E. Freer, K. Yim, G. Fuller, and C. Radke, "Interfacial rheology of globular and flexible proteins at the hexadecane/water interface: Comparison of shear and dilatation deformation", *Journal of Physical Chemistry B* **108**, pp. 3835–3844 (2004).

[50] M. Hollamby, R. Tabor, K. Mutch, K. Trickett, J. Eastoe, R. Heenan, and I. Grillo, "Effect of solvent quality on aggregate structures of common surfactants", *Langmuir* **24**, pp. 12235–12240 (2008).

[51] K. Shinoda and B. Lindman, "Organized surfactant systems: Microemulsions", *Langmuir* **3**, pp. 135–149 (1987).

[52] Guillermo R. Castro, Bridget K. Larson, Bruce Panilaitis, and David L. Kaplan, "Emulsan quantitation by nile red quenching fluorescence assay", *Applied Microbiology and Biotechnology* **67**(6), pp. 767–770 (2005).

[53] M.C.A. Stuart, J.C. van de pas, and J.B.F.N. Engberts, "The use of nile red to monitor the aggregation behavior the use of nile red to monitor the aggregation behavior in ternary surfactant–water–organic solvent systems", *Journal of Physical Organic Chemistry* **18**, pp. 929–934 (2005).

[54] P Greenspan and SD Fowler, "Spectrofluorometric studies of the lipid probe, nile red", *Journal of Lipid Research* **26**(7), pp. 781–789 (1985).

[55] R. N. Wenzel, "Resistance of solid surfaces to wetting by water", *Ind. Eng. Chem.* **28**(8), pp. 988–994 (1936).

[56] A. B. D. Cassie and S. Baxter, "Wettability of porous surfaces", *Trans. Faraday Soc.* **40**, pp. 546–551 (1944).

[57] B. Cortese, S. D'Amone, M. Manca, I. Viola, R. Cingolani, and G. Gigli, "Superhydrophobicity due to the hierarchical scale roughness of pdms surfaces", *Langmuir* **24**, pp. 2712–2718 (2008).

[58] L. Gao and T. J. McCarthy, "How Wenzel and cassie were wrong.", *Langmuir* **23**(7), pp. 3762–5 (2007).

[59] M.V. Panchagnula and S. Vedantam, "Comment on how Wenzel and Cassie were wrong by Gao and McCarthy", *Langmuir* **23**(26), pp. 13242 (2007).

[60] L. Gao and T. J. McCarthy, "Reply to"Comment on How Wenzel and Cassie Were Wrong by Gao and McCarthy", *Langmuir* **23**(26), pp. 13243 (2007).

[61] A. Marmur, "Wetting on hydrophobic rough surfaces: to be heterogeneous or not to be?", *Langmuir* **19**(20), pp. 8343–8348 (2003).

[62] G. Fang, W. Li, X. Wang, and G. Qiao, "Droplet motion on designed microtextured superhydrophobic surfaces with tunable wettability.", *Langmuir* **24**(20), pp. 11651–60 (2008).

[63] W. Li and A. Amirfazli, "Microtextured superhydrophobic surfaces: a thermodynamic analysis.", *Advances in colloid and interface science* **132**(2), pp. 51–68 (2007).

[64] N. A. Patankar, "On the modeling of hydrophobic contact angles on rough surfaces", *Langmuir* **19**(4), pp. 1249–1253 (2003).

[65] N. A. Patankar, "Transition between superhydrophobic states on rough surfaces.", *Langmuir* **20**(17), pp. 7097–102 (2004).

[66] M. Nosonovsky and B. Bhushan, "Patterned nonadhesive surfaces: superhydrophobicity and wetting regime transitions.", *Langmuir* **24**(4), pp. 1525–33 (2008).

[67] C. Ishino, K. Okumura, and D. Quéré, "Wetting transitions on rough surfaces", *Europhysics Letters* **68**(3), pp. 419–425 (2004).

[68] A. Dupuis and J. M. Yeomans, "Modeling droplets on superhydrophobic surfaces: Equilibrium states and transitions", *Langmuir* **21**(2624-2629) (2005).

[69] H. Kusumaatmaja and J. M. Yeomans, "Modeling contact angle hysteresis on chemically patterned and superhydrophobic surfaces", *Langmuir* **23**, pp. 6019–6032 (2007).

[70] N. Moradi, F. Varnik, and I. Steinbach, "Roughness-gradient–induced spontaneous motion of droplets on hydrophobic surfaces: A lattice Boltzmann study", *Europhysics Letters* **89**(2), pp. 26006 (2010).

[71] J. Zhang and D. Y. Kwok, "Contact line and contact angle dynamics in superhydrophobic channels.", *Langmuir* **22**(11), pp. 4998–5004 (2006).

[72] C. Huh and L. E. Scriven, "Hydrodynamic model of steady movement of a solid/liquid/fluid contact line", *J. Colloid Interface Sci.* **35**(1), pp. 85–101 (1971).

[73] M. H. Eres, L. W. Schwartz, and R. V. Roy, "Fingering phenomena for driven coating films", *Physics of Fluids* **12**(6), pp. 1278 (2000).

[74] M. A. Spaid and G. M. Homsy, "Stability of Newtonian and viscoelastic dynamic contact lines", *Physics of Fluids* **8**(2), pp. 460 (1996).

[75] X. Wang, *On the Rolling Motion of Viscous Fluid on a Rigid Surface*, PhD thesis New Jersey Institute of Technology (2008).

[76] H. P. Greenspan, "On the motion of a small viscous droplet that wets a surface", *Journal of Fluid Mechanics* **84**(01), pp. 125–143 (1978).

[77] A. Mazouchi, C. M. Gramlich, and G. M. Homsy, "Time-dependent free surface stokes flow with a moving contact line. i. flow over plane surfaces", *Phys. Fluids* **16**(5), pp. 1647–1659 (2004).

[78] T.-S. Jiang, S.-G. Oh, and J.C. Slattery, "Correlation for dynamic contact angle", *Journal of Colloid and Interface Science* **69**, pp. 74 (1979).

[79] A. A. Becker, *The Boundary Element Method in Engineering: a complete course*, McGraw-Hill (1992).

[80] C. Pozrikidis, *Boundary integral and singularity methods for linearized viscous flow*, Cambridge University Press (1992).

[81] M. A. Kelmanson, "An integral equation method for the solution of singular slow flow problems", *J. Comput. Phys.* **51**, pp. 139–158 (1983).

[82] H. K. Moffatt, "Viscous and resistive eddies near a sharp corner", *J. Fluid Mech.* **18**, pp. 1–18 (1964).

[83] S. Betelu, J. Diez, L. Thomas, R. Gratton, and B. Marino, "A boundary element method for viscous gravity currents", *Int. J. Numer. Meth. Fluids* **25**, pp. 1–19 (1997).

[84] T. Onda, S. Shibuichi, N. Satoh, and K. Tsujii, "Super-water-repellent fractal surfaces", *Langmuir* **12**(9), pp. 2125–2127 (1996).

[85] J. Jopp, H. Grüll, and R. Yerushalmi-Rozen, "Wetting behavior of water droplets on hydrophobic microtextures of comparable size", *Langmuir* **20**, pp. 10015–10019 (2004).

[86] B He, J Lee, and N Patankar, "Contact angle hysteresis on rough hydrophobic surfaces", *Colloids and Surfaces A: Physicochemical and Engineering Aspects* **248**(1-3), pp. 101–104 (2004).

[87] Bo He, Neelesh A. Patankar, and Junghoon Lee, "Multiple Equilibrium Droplet Shapes and Design Criterion for Rough Hydrophobic Surfaces", *Langmuir* **19**(12), pp. 4999–5003 (2003).

[88] "http://www.microchem.com/products/pdf/su-82000datasheet2025thru2075ver4.pdf".